6-28-2016

Tunable Nano-Delivery System for Cancer Treatment: A New Approach for Targeted Localized Drug Delivery

Rana Falahat
University of South Florida, rfalahat@mail.usf.edu

Tunable Nano-Delivery System for Cancer Treatment:

A New Approach for Targeted Localized Drug Delivery

by

Rana Falahat

A dissertation submitted in partial fulfillment
of the requirements for the degree of
Doctor of Philosophy
Department of Chemical and Biomedical Engineering
College of Engineering
University of South Florida

Major Professor: Norma Alcantar, Ph.D.
Nathan Gallant, Ph.D.
Mark Jaroszeski, Ph.D.
Ryan Toomey, Ph.D.
Marzenna Wiranowska, Ph.D.

Date of Approval:
June 22, 2016

Keywords: Chlorotoxin, Chitosan Hydrogel, Niosome,
ATR-FTIR, Glioma

DEDICATION

I would like to dedicate this dissertation to:

My parents *Amineh Moloudi* and *Hedayat Falahat*,

My sister *Ayda Falahat*,

My brother *Ata Falahat,*

And my husband *Dr. Ahmadreza Sedaghat.*

ACKNOWLEDGMENTS

I would like to express my deepest appreciation to my advisor, *Dr. Norma Alcantar*, thank you for your endless encouragement, guidance and support. Thank you for giving me the incredible opportunity of working on this project and allowing me to grow as a research scientist. I am forever indebted to you for shaping my research life.

I would also like to extend my gratitude to *Dr. Marzenna Wiranowska*. I am deeply grateful to you for introducing me to cancer research and training me in cell culture experiments. Thank you for your constant support and advice.

Dr. Ryan Toomey, thank you for designing and pioneering this project. Your lessons in scientific and engineering problem solving skills have been incredibly helpful in shaping my research career.

Dr. Nathan Gallant, thank you for your guidance, support and insightful comments at different stages of my research. Your help has been invaluable particularly through the Cell ELISA studies.

Dr. Mark Jaroszeski, I am grateful to you for your valuable insights in nanoparticle preparation and characterization which helped me to improve my knowledge in this area. I would also like to thank you for letting me use your lab when I needed it.

A special thanks to *Robert Hill* at the Cell Biology, Microbiology and Molecular Biology (CMMB) Core Facility for his great assistance and valuable discussion regarding flow cytometry and Western blotting studies.

I would like to thank *Edward Haller* at the Integrative Biology Microscopy Core Laboratory for providing extensive training for transmission electron microscopy (TEM) studies.

I would like to acknowledge *Dr. Vinay Gupta* and *Dr. Patricia Kruk* for the instrumental support.

I would also like to express my gratitude to the USF-Byrd Alzheimer's Institute for the financial support.

I would like to thank all my lab members for their support: *Dr. Daniela Stebbins, Zeinab Veisi*, *Wen Zhao*, *Fei Guo*, *Tunan Peng* and *Molly Skinner*.

My deepest gratitude to my parents *Amineh Moloudi* and *Hedayat Falahat*, my sister *Ayda Falahat*, and my brother *Ata Falahat* for their endless love, understanding, patience and support throughout my entire life. I am forever indebted to my husband, *Dr. Ahmadreza Sedaghat*, whose unconditional love and constant encouragement have helped me in accomplishing this journey.

TABLE OF CONTENTS

LIST OF TABLES

LIST OF FIGURES

ABSTRACT

Localized drug delivery systems have been widely studied as potential replacements for conventional chemotherapy with the capability of providing sustained and controlled drug release in specific targeted sites. They offer numerous benefits over conventional chemotherapy such as enhancing the stability of embedded drugs and preserving their anticancer activity, providing sustained and controlled drug release in the tumor site, reducing toxicity and diminishing subsequent side effects, minimizing the drug loss, averting the need for frequent administrations, and minimizing the cost of therapy.

The aim of this study is to develop a localized drug delivery system with niosomes embedded in a chitosan hydrogel with targeting capabilities. The incorporation of niosomes into a chitosan hydrogel has several advantages over each individually being used. First, embedding niosomes in a chitosan hydrogel can yield control over drug release especially for small molecule drugs. Second, chitosan hydrogel may improve the release time and dosage of drugs from niosomes by protecting them with an extra barrier, resulting in tunable release rates. Third, as a localized delivery system, chitosan hydrogels can prevent the migration of niosomes away from the targeted tumor sites. Finally, chitosan has mucoadhesive property which can be used in the targeting of the tumor cells with the mucin over expression.

To enhance the specific targeting, the capacity of chitosan to target MUC1 overexpression in cancer cells will be analyzed. Similarly, the incorporation of chlorotoxin in this system will be achieved and evaluated. Chlorotoxin, a 36-amino acid peptide, is purified

from *Leiurus quinquestriatus* scorpion venom with a distinct characteristic of binding preferentially to neuroectoderma tumors such as glioma, but not to normal tissue.

The overexpression of MUC1, a mucin antigen, in certain cancer cells has been used as an attractive therapeutic target in the design of a drug delivery system consisting of chitosan with a distinct mucoadhesive property. To determine the level of MUC1expression in different cell lines, Cell based Enzyme Linked Immunosorbent Assay (Cell ELISA) was developed for the first time.

Attenuated Total Reflectance- Fourier Transform Infra-Red (ATR-FTIR) Spectroscopy is used to investigate the possible molecular interaction between chlorotoxin and glioma cells. This study presents a new approach in monitoring the biochemical and biophysical changes in glioma cells after being exposed to CTX. In addition to characterizing the signature spectra of CTX and glioma cells, we evaluated the differences in biochemical compositions of the spectra of the glioma cells treated with and without CTX over different incubation time periods.

The results indicate that the proposed localized drug delivery system with the distinct tumor targeting features and extended release profiles would tune and control the specific delivery of chemotherapeutics in tumor sites.

CHAPTER 1: INTRODUCTION

According to American Cancer Society's 2015 Cancer Statistics report, the lifetime probability of being diagnosed with an invasive cancer is slightly less than 1 in 2 for men and a little more than 1 in 3 for women, which leads to estimated 1,658,370 new cancer cases and 589,430 cancer deaths in the United States in 2015 [1].

Depending on the cancer type, diagnostic stage, and patient's tolerance to different therapies, the treatment is then designed. Principal cancer treatment modalities include surgery, radiotherapy, and chemotherapy. Surgery is the first step in the treatment of solid tumors at early or intermediate stage in an accessible and localized region of the body [2]. Following tumor excision, conventional chemotherapy is applied to eradicate any remaining cancerous cells and to prevent tumor recurrence [2]. Despite of being the most common approach for cancer treatment, the efficacy of conventional chemotherapy is limited [2-4]. First, it distributes anticancer drugs to the whole body and does not differentiate between normal and cancer cells [3, 4]. In fact, only a small percentage of the administered drugs can reach the tumor areas leading to insufficient bioavailability of therapeutics in the sites needed treatment [3, 4].

Second, most of drug release occurs shortly after its administration causing the drug levels in the body to abruptly increase, peak and then decrease within a short period of time. This non-sustained drug release in conventional chemotherapy leads to undesirable side effects due to toxicities at the elevated drug levels and insufficient therapy afterwards [3-6].

Third, multiple injections are required to increase the bioavailability of drugs in the tumor sites. These repeated administrations can exacerbate the existing side effects such as kidney or nerve damage [2, 3, 5].

Finally, the need of using high amount of anticancer drugs in conventional chemotherapy, the need to treat inherent secondary effect and also the need for multiple cycles of chemo increase the cost of cancer treatment (Figure 1.1) [3, 5].

To overcome these problems, localized drug delivery systems have been widely studied as potential replacement for conventional chemotherapy with the capability of providing sustained and controlled drug release in specific targeted sites [3, 5, 6]. Localized drug delivery systems which are designed to enhance the efficacy of cancer treatments offer numerous benefits over conventional chemotherapy, and can be summarized as follows:

1- Enhance the stability of embedded drugs and preserving their anticancer activity.
2- Provide sustained and controlled drug release in the tumor site to ensure the adequate drug uptake into cancer cells.
3- Reduce toxicity to the whole body and diminish of subsequent side effects by minimizing systemic distribution.
4- Effective application of required therapeutics, and therefore, drug loss is minimal.
5- Avert the need for frequent administrations.
6- Minimize the cost of therapy as a result of requiring only one single administration.
7- Tune the dosage and release of drugs

Depending on the modality of administration and release mechanism, current local drug delivery systems can be categorized into two groups [3].

The first group consists of nanoparticles which are administered systematically with specific targeting property toward the tumor site [3-6]. Polymeric nanoparticles, polymeric micelles, dendrimers, liposomes, and niosomes are examples of these local drug delivery systems [3-7].

Also new therapeutic schemes based on the administration of living cells have been developed where the surface of therapeutic cells can be modified with artificial receptors, and multifunctional nanomaterials for enhanced cell therapies [8].

They can reach to the target sites by passive or active targeting. In passive targeting nanoparticles can diffuse through the leaky and dilated walls of tumor vasculature which results in their accumulation in the tumor site, while active targeting occurs due to interactions of ligands on nanoparticles with an over-expressed tumor cell marker (Figure 1.2) [9]. Despite the promising ability in targeting tumor sites, the localization of these nanoparticles is highly challenging as they are removed by the mononuclear phagocyte system (MPS) cells upon their intravenous administration (Figure 1.3) [10]. Blood monocytes, dendritic cells, and tissue-resident macrophages are examples of the MPS cells which are responsible for detecting, clearing, and degrading foreign materials from circulation [10, 11]. In addition to reducing the bioavailability of drugs in the tumor sites, the MPS uptake of nanomaterials can cause other problems such as inflammation, toxicities due to the toxic byproducts, and distribution and accumulation of nanomaterials in sensitive body areas [10]. The uncontrolled and unpredicted localization of nanomaterials as well as the possibility of toxicity have hindered their translation into clinical applications [10, 12].

The second group consists of polymer based drug delivery systems with intratumoral or peritumoral injection, or implantation into tumor resection cavities. They have been designed in

various forms including gels, films, wafers, and rods, featuring controlled and sustained drug release kinetics. Implants require a surgical procedure at the tumor site, which leads to additional costs and complications.

Thermoresponsive *in-situ* hydrogel systems have gained special attention in drug delivery [13]. Their initial liquid formulation can be applied at minimally invasive manner by a simple injection to fill the shape of any targeted area [14-16]. Upon their injection, they transform into a soft gel at body temperature (Figure 1.4). As mentioned above, synthetic polymers can be tailored and modified to provide excellent mechanical and chemical properties, but because of their synthetic origin, its application can lead to acute or chronic inflammations, retarded removal rates, and localized pH decrease as a result of the acidity of the accumulated degradation products [13].

Natural polymers such as polysaccharides and proteins are obtained from abundantly available natural resources with great biocompatibility and biodegradability properties. Unlike synthetic polymers, natural polymers can degrade into components which are non-inflammatory or cytotoxic [4].

Among them, polysaccharides have the advantage of interacting with living cells with excellent hemocompatibility. On the other hand, protein-originated polymers have the risk of immunegenecity and transmission of pathogens from animal donors [17].

Chitosan is a polysaccharide obtained by alkaline deacetylation of chitin [18]. It has been widely used in various biomedical applications, owing to its superior biocompatibility, enzymatic degradability and low toxicity [19, 20]. It also benefits from antimicrobial, antifungal actions and anticoagulant properties [4, 21].

Thermoresponsive chitosan hydrogel systems have been prepared with different chemical or physical crosslinking methods such as grafting polymerization of a polymer (e.g. poly(N-isopropylacrylamide), poly(ethylene glycol) and Pluronic) onto chitosanor neutralization with polyol salts such as glycerol phosphate disodium salt [5, 17, 22-24].

Despite all the remarkable properties these hydrogels systems have some limitations [25]. Due to the high amount of water in the hydrogel network, the encapsulation of hydrophobic drugs is often challenging [25]. Also, large pores in their structure can lead to relatively fast release rates particularly for small molecule drugs [26].

To overcome these problems, incorporation of a secondary drug carrier such as liposomes, micelles, and other particle based vehicles into the hydrogel network has been considered recently [25-28].

Non-ionic surfactant vesicles or niosomes have been used as drug delivery vehicles [29-33]. Similar to liposomes, niosomes have an enclosed spherical bilayer structure with hydrophilic core and hydrophobic shell allowing them to be used for encapsulating both hydrophilic and hydrophobic drugs [29]. Also, a mixture of hydrophobic and hydrophilic drugs can be encapsulated in the same vesicle [34]. As another advantage, niosomes do not interact with any of the charge groups of a drug molecule [29]. As compared to liposomes, niosomes provide better stability while having lower cost and being more convenient to store [29, 30].

In this study, niosomes with chemotherapeutic drugs are embedded in a thermoresponsive hydrogel network. Such configuration has allowed us to finely tune drug release time, concentration and dosage [35, 36].

The incorporation of niosomes into a chitosan hydrogel has several advantages over each individually being used. First, niosomes can encapsulate hydrophobic drugs which is challenging

in the case of embedding them in a pure hydrogel. Second, embedding niosomes in a chitosan hydrogel can yield slower drug release especially for small molecule drugs. Third, chitosan hydrogel may improve the release kinetics of drugs from niosomes by protecting them with an extra barrier and by preventing or decreasing the burst release, which is typical in spherical vesicles, resulting in extended release rates. Fourth, as a localized delivery system, chitosan hydrogels can prevent the migration of niosomes away from the targeted tumor sites. Finally, chitosan has mucoadhesive property which can be used in the targeting of the tumor cells with the mucin over expression.

Therefore, developing a localized drug delivery system with niosomes embedded in chitosan hydrogel with enhanced targeting characteristics is the focus of this study.

In targeted drug delivery a therapeutic agent is delivered specifically to a particular tumor cell [37]. Targeted drug delivery is highly beneficial in cancer therapy where anticancer drugs affect both tumor cells and normal cells resulting in toxicities and subsequent side effects [37].

Tumor-specific targeting therapy uses an approach where a tumor-specific molecule helps the drug to reach to the tumor cells [38]. This specific targeting is based on the interactions involved between the targeting molecules and the receptors present on the surface of tumor cells and not on the surface of normal cells [37].

Chlorotoxin (CTX) is a 36-amino acid peptide derived from the venom of the scorpion *Leirius quinquestriatus* that preferentially binds to tumor cells of neuroectodermal origin, such as glioma, but not to normal non-transformed cells [39-41]. Several studies have demonstrated its use as an imaging and targeting agent for drug and radioisotope delivery.

Tumor paint BLZ-100, a bioconjugat of CTX and Cy5.5 (a near-infrared fluorescent molecule) has been recently approved to be tested in human clinical trials [42]. This bioconjugat

targets tumors with the fluorescent dye enabling surgeons to distinguish normal tissue from malignancies such as glioma, prostate cancer, intestinal cancer and sarcoma [42, 43]. CTX has been also investigated as a targeting agent in many drug delivery systems including CTX-conjugated iron oxide nanoparticles and CTX-modified doxorubicine-loaded liposomes [44, 45].

To take advantage of this unique targeting feature, we have incorporated CTX along with niosomes in the chitosan hydrogel as the second targeting strategy to further improve the specific delivery of drugs to tumor cells such as glioma.

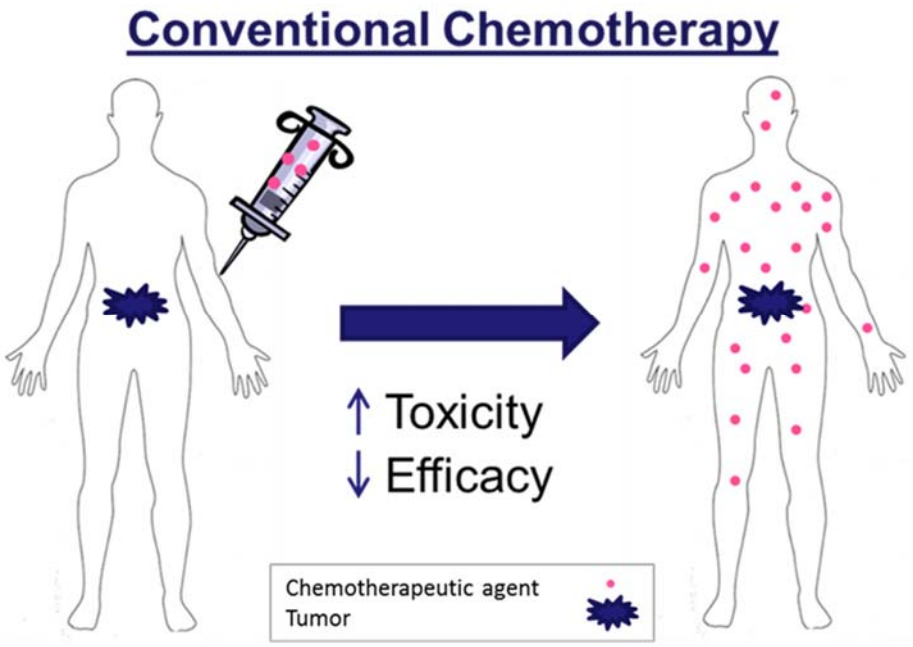

Figure 1.1 Major drawbacks associated with the conventional chemotherapy in the treatment of the solid tumors

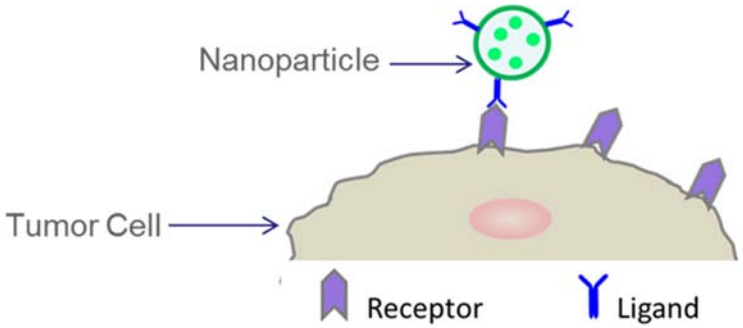

Figure 1.2 Schematic representation of an active targeting strategy to target tumor cells through the interactions of ligands on nanoparticles with an over-expressed tumor cell marker

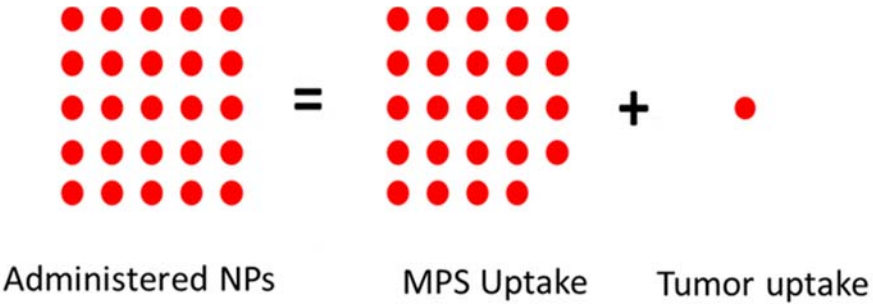

Figure 1.3 Schematic representation of systematically administered Nanoparticles (NPs), showing their considerably higher uptake by the mononuclear phagocyte system (MPS) as compared to the tumor site

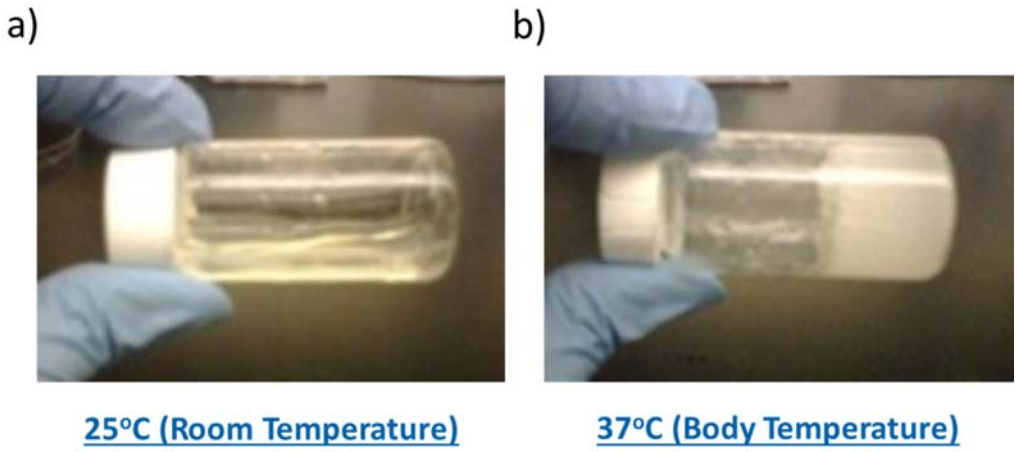

Figure 1.4 Chitosan/β-glycerophosphate in liquid form at room temperature (25°C) (a) and as a soft gel at body temperature (37°C) (b).

1.1. References

1. Siegel, R.L., K.D. Miller, and A. Jemal, *Cancer statistics, 2015.* CA: a cancer journal for clinicians, 2015. **65**(1): p. 5-29.
2. DeSantis, C.E., et al., *Cancer treatment and survivorship statistics, 2014.* CA: a cancer journal for clinicians, 2014. **64**(4): p. 252-271.
3. Wolinsky, J.B., Y.L. Colson, and M.W. Grinstaff, *Local drug delivery strategies for* cancer *treatment: gels, nanoparticles, polymeric films, rods, and wafers.* Journal of controlled release, 2012. **159**(1): p. 14-26.
4. De Souza, R., et al., *Polymeric drug delivery systems for localized cancer chemotherapy.* Drug delivery, 2010. **17**(6): p. 365-375.
5. Ta, H.T., C.R. Dass, and D.E. Dunstan, *Injectable chitosan hydrogels for localised cancer therapy.* Journal of Controlled Release, 2008. **126**(3): p. 205-216.
6. Cho, K., et al., *Therapeutic nanoparticles for drug delivery in cancer.* Clinical cancer research, 2008. **14**(5): p. 1310-1316.
7. Timko, B.P. and D.S. Kohane, *Drug-Delivery Systems for Tunable and Localized Drug Release.* Israel Journal of Chemistry, 2013. **53**(9-10): p. 728-736.
8. Stephan, M.T. and D.J. Irvine, *Enhancing cell therapies from the outside in: cell surface engineering using synthetic nanomaterials.* Nano today, 2011. **6**(3): p. 309-325.
9. Thassu, D., M. Deleers, and Y.V. Pathak, *Nanoparticulate drug delivery systems*. Vol. 166. 2007: CRC Press.
10. Walkey, C.D., et al., *Nanoparticle size and surface chemistry determine serum protein adsorption and macrophage uptake.* Journal of the American Chemical Society, 2012. **134**(4): p. 2139-2147.
11. Moghimi, S.M., A.C. Hunter, and J.C. Murray, *Long-circulating and target-specific nanoparticles: theory to practice.* Pharmacological reviews, 2001. **53**(2): p. 283-318.
12. Davis, M.E. and D.M. Shin, *Nanoparticle therapeutics: an emerging treatment* modality *for cancer.* Nature reviews Drug discovery, 2008. **7**(9): p. 771-782.
13. Yu, L. and J. Ding, *Injectable hydrogels as unique biomedical materials.* Chemical Society Reviews, 2008. **37**(8): p. 1473-1481.
14. Kim, S., et al., *A chitosan/β-glycerophosphate thermo-sensitive gel for the delivery of ellagic acid for the treatment of brain cancer.* Biomaterials, 2010. **31**(14): p. 4157-4166.
15. Obara, K., *et* al., *Photocrosslinkable chitosan hydrogel containing fibroblast growth factor-2 stimulates wound healing in healing-impaired db/db mice.* Biomaterials, 2003. **24**(20): p. 3437-3444.
16. Ruel-Gariépy, E., et al., *A thermosensitive chitosan-based hydrogel for the local delivery of paclitaxel.* European Journal of Pharmaceutics and Biopharmaceutics, 2004. **57**(1): p. 53-63.

17. Bhattarai, N., J. Gunn, and M. Zhang, *Chitosan-based hydrogels for controlled, localized drug delivery.* Advanced drug delivery reviews, 2010. **62**(1): p. 83-99.

18. Kumar, M.N.R., *A review of chitin and chitosan applications.* Reactive and functional polymers, 2000. **46**(1): p. 1-27.

19. Chandy, T. and C.P. Sharma, *Chitosan-as a biomaterial.* Biomaterials, artificial cells and artificial organs, 1990. **18**(1): p. 1-24.

20. Kean, T. and M. Thanou, *Biodegradation, biodistribution and toxicity of chitosan.* Advanced drug delivery reviews, 2010. **62**(1): p. 3-11.

21. Ganji, F., M. Abdekhodaie, and A.R. SA, *Gelation time and degradation rate of chitosan-based injectable hydrogel.* Journal of sol-gel science and technology, 2007. **42**(1): p. 47-53.

22. Park, K.M., et al., *Thermosensitive chitosan–Pluronic hydrogel as an injectable cell delivery carrier for cartilage regeneration.* Acta biomaterialia, 2009. **5**(6): p. 1956-1965.

23. Chenite, A., et al., *Rheological characterisation of thermogelling chitosan/glycerol-phosphate solutions.* Carbohydrate Polymers, 2001. **46**(1): p. 39-47.

24. Ruel-Gariepy, E., et al., *Thermosensitive chitosan-based hydrogel containing liposomes for the delivery of hydrophilic molecules.* Journal of Controlled Release, 2002. **82**(2): p. 373-383.

25. Hoare, T.R. and D.S. Kohane, *Hydrogels in drug delivery: progress and challenges.* Polymer, 2008. **49**(8): p. 1993-2007.

26. Pan, W. and Z. Yang, *Thermoreversible Pluronic® F127-based hydrogel containing liposomes for the controlled delivery of paclitaxel: in vitro drug release, cell cytotoxicity, and uptake studies.* International journal of nanomedicine, 2011. **6**: p. 151-166.

27. Wang, C., N.T. Flynn, and R. Langer, *Controlled structure and properties of thermoresponsive nanoparticle–hydrogel composites.* Advanced Materials, 2004. **16**(13): p. 1074-1079.

28. Segovia, N., et al., *Hydrogel doped with nanoparticles for local sustained release of siRNA in breast cancer.* Advanced healthcare materials, 2015. **4**(2): p. 271-280.

29. Uchegbu, I.F. and S.P. Vyas, *Non-ionic surfactant based vesicles (niosomes) in drug delivery.* International Journal of pharmaceutics, 1998. **172**(1): p. 33-70.

30. Manosroi, A., et al., *Characterization of vesicles prepared with various non-ionic surfactants mixed with cholesterol.* Colloids and Surfaces B: Biointerfaces, 2003. **30**(1): p. 129-138.

31. Pardakhty, A., J. Varshosaz, and A. Rouholamini, *In vitro study of polyoxyethylene alkyl ether niosomes for delivery of insulin.* International journal of pharmaceutics, 2007. **328**(2): p. 130-141.

32. Bayindir, Z.S. and N. Yuksel, *Characterization of niosomes prepared with various nonionic surfactants for paclitaxel oral delivery.* Journal of pharmaceutical sciences, 2010. **99**(4): p. 2049-2060.

33. Pham, T.T., et al., *Liposome and niosome preparation using a membrane contactor for scale-up.* Colloids and Surfaces B: Biointerfaces, 2012. **94**: p. 15-21.

34. Williams, E.C., *Smart Packaging: A Novel Technique For Localized Drug Delivery For Ovarian Cancer.* 2012.

35. Williams, E.C., R. Toomey, and N. Alcantar, *Controlled release niosome embedded chitosan system: Effect of crosslink mesh dimensions on drug release.* Journal of Biomedical Materials Research Part A, 2012. **100**(12): p. 3296-3303.

36. Falahat, R., et al., *Targeted delivery to tumor cells by using tunable nano-delivery system with chlorotoxin.* Cancer Research, 2013. **73**(8 Supplement): p. 4523-4523.

37. Brannon-Peppas, L. and J.O. Blanchette, *Nanoparticle and targeted systems for cancer therapy.* Advanced drug delivery reviews, 2004. **56**(11): p. 1649-1659.

38. Park, J.H., et al., *Targeted delivery of low molecular drugs using chitosan and its derivatives.* Advanced drug delivery reviews, 2010. **62**(1): p. 28-41.

39. Debin, J.A., J.E. Maggio, and G.R. Strichartz, *Purification and characterization of chlorotoxin, a chloride channel ligand from the venom of the scorpion.* American Journal of Physiology-Cell Physiology, 1993. **264**(2): p. C361-C369.

40. Lyons, S.A., J. O'Neal, and H. Sontheimer, *Chlorotoxin, a scorpion-derived peptide, specifically binds to gliomas and tumors of neuroectodermal origin.* Glia, 2002. **39**(2): p. 162-173.

41. Wiranowska, M., L.O. Colina, and J.O. Johnson, *Clathrin-mediated entry and cellular localization of chlorotoxin in human glioma.* Cancer Cell Int, 2011. **11**: p. 27.

42. Butte, P.V., et al., *Near-infrared imaging of brain tumors using the Tumor Paint BLZ-100 to achieve near-complete resection of brain tumors.* Neurosurgical focus, 2014. **36**(2): p. E1.

43. Veiseh, M., et al., *Tumor paint: a chlorotoxin: Cy5. 5 bioconjugate for intraoperative visualization of cancer foci.* Cancer research, 2007. **67**(14): p. 6882-6888.

44. Sun, C., et al., *Tumor-targeted drug delivery and MRI contrast enhancement by chlorotoxin-conjugated iron oxide nanoparticles.* 2008.

45. Xiang, Y., et al., *Chloride channel-mediated brain glioma targeting of chlorotoxin-modified doxorubicine-loaded liposomes.* Journal of controlled release, 2011. **152**(3): p. 402-410.

CHAPTER 2: CHLOROTOXIN-MODIFIED NIOSOME-CHITOSAN HYDROGEL COMPLEXES FOR SUSTAINED, CONTROLLED AND TARGETED DRUG DELIVERY

2.1. Abstract

This study reports a development and characterization of a localized drug delivery system with enhanced targeting ability consisting of non-ionic surfactant vesicles (niosomes) with chlorotoxin (CTX) embedded in a chitosan hydrogel. With the controlled, sustained and targeted delivery features, this system represents a novel approach in cancer therapy.

Release profiles of 5,6-carboxyfluorescein from niosomes alone, niosomes in chitosan hydrogel, and CTX-niosomes in chitosan hydrogel were studied in a release medium with low ionic strength and pH 6.0 (similar to tumor extracellular pH). Morphological assessments of niosomes alone and niosomes with CTX were performed using Transmission electron microscopy (TEM). Attenuated Total Reflectance-Fourier Transform Infra-Red (ATR-FTIR) spectroscopy was also employed to study the possible interactions between niosomes and CTX.

Release rate studies indicated that embedding niosomes in chitosan hydrogel significantly extends the release rates after 24 h. Embedding CTX along with niosomes in chitosan hydrogel resulted in slightly more extended release rates as compared to the release rates from niosomes alone in chitosan hydrogel. Attachment of CTX to the surface of niosomes shown by TEM imaging improved the stability of niosomes resulting in extended release rates. ATR-FTIR studies also confirmed the interaction of CTX with niosomes.

2.2. Introduction

Non-ionic surfactant vesicles (niosomes) are among the common vesicular systems widely studied as drug delivery vehicles [1-5]. Similar to liposomes, niosomes have an enclosed spherical bilayer structure with hydrophilic core and hydrophobic shell allowing them to be used for the delivery of both hydrophilic and hydrophobic drugs [6, 7]. Also, a mixture of hydrophobic and hydrophilic drugs can be encapsulated in the same vesicle [8]. Niosomes have been reported to provide better stability while having lower cost and being more convenient to store as compared to liposomes [1, 2]. Having these benefits, niosomes have received a great attention as potential delivery systems for various drugs and therapeutic agents such as anticancer drugs (doxorubicin, paclitaxel and carboplatin) [8-10], insulin [3, 11], vasoactive intestinal peptide (VIP) [12], and many others.

Despite all the promising features, the localization of niosomes in tumor sites is highly challenging due to their removal by the mononuclear phagocyte system (MPS) cells upon the systemic administration [13]. Also, as being osmotically active they may have an undesired burst release which is typical in spherical vesicles.

To overcome these problems, in this study niosomes were embedded in a thermosensitive chitosan hydrogel network. The initial liquid formulation of chitosan hydrogel at room temperature allows it to be injected into the cavities after tumor resection and to fill the shape of the targeted areas [14-16]. Upon the injection, it transforms into a soft gel at body temperature [14-16]. By protecting niosomes with an extra barrier and by preventing or decreasing the burst release, chitosan hydrogel can improve the release kinetics of drugs from niosomes and result in extended release rates. Also, as a localized delivery system, chitosan hydrogel can prevent the migration of niosomes away from the targeted tumor sites. Finally, chitosan has a mucoadhesive

property which can be used in the targeting of the tumor cells with the mucin over expression such as ovarian carcinoma and other adenocarcinomas [17, 18].

To further improve the specific delivery of drugs to tumor cells we have incorporated Chlorotoxin (CTX). CTX is a 36-amino acid peptide derived from the venom of the scorpion *Leirius quinquestriatus* with known specificity toward tumor cells of neuroectodermal origin, such as glioma, but not to normal non-transformed cells.[19-21] Many studies have shown its application as an imaging and targeting agent for drug and radioisotope delivery.[22-25] A bioconjugat of CTX and Cy5.5 (a near-infrared fluorescent molecule) recently has been entered clinical trials.[26] By specific targeting of tumor cells with a fluorescent dye, this bioconjugat allows surgeons to distinguish normal tissue from malignancies such as glioma, prostate cancer, intestinal cancer, and sarcoma.[22, 26] As a targeting agent, CTX has been investigated in many drug delivery systems including CTX-conjugated iron oxide nanoparticles, CTX-modified doxorubicine-loaded liposomes, and CTX-assisted nanoparticle-chitosan hydrogel complexes.[27-29]

In this study, we performed the release rate studies on niosomes and niosomes embedded in chitosan hydrogel with and without CTX to examine the effect of chitosan and CTX on the release rates. We used Transmission Electron Microscopy (TEM) for morphologic assessments, and Attenuated Total Reflectance-Fourier Transform Infra-Red (ATR-FTIR) spectroscopy to study the possible interactions between CTX and niosomes.

2.3. Materials and Methods

2.3.1. Materials

Chlorotoxin was purchased from Iris Biotech GmbH (Marktredwitz, Germany). Span 60, cholesterol, dicetyl phosphate (DCP), medium molecular weight chitosan and 5(6)-

Carboxyfluorescein dye were obtained from Sigma-Aldrich (St. Louis, MO). β-glycerophosphate disodium salt (β-GP) was purchased from Calbiochem EMD Biosciences (La Jolla, CA) and used as the crosslinking agent. All the other reagents were purchased from Fisher Scientific (Fair Lawn, NJ).

2.3.2. Preparation of Niosomes

Dye-loaded niosomes were prepared by the thin film hydration method [4]. Briefly, span 60, cholesterol and DCP (1:1:0.1 molar ratio) were dissolved in chloroform and transferred to a 50 mL round bottom flask. To make a thin film, chloroform was removed by rotating the flask using a Buchi rotary evaporator (Flawil, Switzerland) in a water bath at 60ºC. The thin film was left in the fume hood overnight to remove any remaining traces of the chloroform. The dried thin film was hydrated with dye solution with concentration of 5 mM in phosphate buffer saline (PBS) in the rotary evaporator for 1 h at 60ºC. Size reduction process was performed using an Avanti Polar Lipids Mini-Extruder (Alabaster, AL) by passing the niosome suspension through 800, 400 or 80 nm polycarbonate membrane filters (Nuclepore Corp., Pleasanton, CA) at 60ºC. The un-trapped dye was separated from niosome suspension using a Beckman XL-100 ultracentrifuge (Fullerton, CA) operating at 60,000 rpm for 1 h. Dye-loaded niosomes in the precipitate were resuspended in 0.01 M PBS and kept at 4ºC for the future experiments.

2.3.3. Preparation of Chitosan Hydrogel

A 2.8% (w/v) chitosan solution was prepared by dissolving chitosan powder in 1.5 ml of 0.1 M hydrochloric acid at room temperature. A β-GP solution at a concentrations of 65% (w/v) was prepared in 0.5 ml of deionized water and kept at 4ºC for 1 h prior to crosslinking along with the chitosan solution. While stirring continuously, the cold β-GP solution was added drop wise to the cold chitosan solution. After adding the last drop, the final solution was stirred for 10 min.

0.7 ml of niosome suspension was added into the chitosan and β-GP mixture followed by 5 min stirring. The prepared mixture was transferred into a 5 ml beaker and placed in a water bath at 37 ^{o}C and allowed to gel (Figure 2.1).

2.3.4. Release Studies - Niosomes

The release rate of the entrapped dye from niosomes was studied at specified time intervals using the Dialysis method. Briefly, 100 µl of niosome solutions were pipetted into Slide-A-Lyzer mini-dialysis units with a 10,000-molecular-weight-cutoff (MWCO) membrane (Pierce Biotechnology) floating in a mini-dialysis flotation device (Pierce Biotechnology). They were dialyzed against 100 ml of 0.01M PBS (pH 7.4) or salt-free water (pH 6.0) at 37^{o}C. While stirring the release medium using the magnetic stirrer at 200 rpm, 500 µl aliquots of the release medium were taken at specified time intervals and refilled with the same amount of the fresh medium. The cumulative amount of the released dye in collected samples was quantified in triplicates using a Fluorescence Plate Reader (Biotek, Flx800) at an excitation wavelength of 485 nm and emission wavelength of 528 nm.

2.3.5. Release Studies - Chitosan Hydrogels Containing Niosomes

The prepared chitosan hydrogels containing niosomes with and without CTX were placed into 100 ml of deionized water (pH 6.8) at 37^{o}C while stirred at 200 rpm. At specified time points 500 µl aliquots of the release medium were collected and stored at 4^{o}C for further analysis. After taking each sample, the same amount of the release medium was added into the container.

2.3.6. Transmission Electron Microscopy

Transmission electron microscopy (TEM) was used to assess the morphology of niosomes alone and niosomes with CTX. The TEM samples were prepared by placing a droplet

of the suspension (after appropriate dilution) on a 150-mesh carbon coated formvar copper grid (Electron Microscopy Sciences, Hatfield, PA) and allowed to adhere for 1 min. Following the removal of the excess solution using a filter paper, the samples were placed in a vacuum chamber for 10 min at 40ºC. The samples were then viewed under an electron microscope (FEI Morgagni TEM) with an operating voltage of 80 kV.

2.3.7. ATR-FTIR Spectroscopy

A 100 µl niosome suspension with and without CTX was introduced onto a 45º ZnSe flat crystal (Thermo Scientific, WI) and allowed to air dry for 1 hr. To remove any excess water, the formed films were exposed to an ultrapure nitrogen flux before collecting the spectra. The ATR-FTIR spectra were obtained using a Nicolet 6700 spectrometer (Thermo Scientific, WI). The spectra in the 4000-400 cm^{-1} region were collected using 300 scans at a spectral resolution of 4 cm^{-1}. The data analysis was performed using OMNIC software (Thermo Scientific, WI). To ensure appropriate comparison between different samples, all the spectra were baseline corrected.

2.4. Results and Discussion

2.4.1. Release Studies - Niosomes

The *in-vitro* release rate studies for niosomes were performed in PBS (pH 7.4) representing physiological condition and salt-free water (pH 6.0) representing tumor pH conditions. The release profiles of 5,6-carboxyfluorescein from niosomes are shown in Figure 2.2. The fast release rates in both conditions within the first 24 hours may be a result of dye desorption from the surface of niosomes. The slow release rates after 24 h for niosomes exposed to PBS can be related to diffusion of dye from the bilayer of niosomes. Unlike niosomes in PBS,

the continuous fast release profiles from niosomes exposed to salt-free water were observed even after 24 h.

As niosomes are considered to be osmotically active, exposing them to salt-free water increases their osmotic pressure and results in their swelling [1]. This increases the permeability of dye from the bilayer leading to faster and less sustained release rates in salt-free water as compared to their release rates in PBS.

2.4.2. Release Studies - Chitosan Hydrogels Containing Niosomes

To provide niosomes with more stability and to decrease the osmotic pressure effect on the release rates, niosomes were embedded in a chitosan hydrogel. The release profiles of niosomes embedded with and without CTX in chitosan hydrogel along with the bare niosomes exposed to salt-free water are presented in Figure 2.3. It can be clearly seen that the incorporation of niosomes in chitosan hydrogel extended the release rates particularly after 24 h. The fast release rates within the first 24 h are mostly associated with niosomes placed on the surface of hydrogel, while the slower release rates after 24 h are related to niosomes embedded after the edge of chitosan network which provides them with more stability. In fact, only 61% cumulative release occurred for niosomes embedded in chitosan hydrogel after 21 days of the exposure to salt-free water. To investigate the effect of CTX on the release profiles, the same release rate studies were performed for CTX and niosomes embedded in chitosan hydrogel. The release profiles of 5,6-carboxyfluorescein from this system is also presented in Figure 2.3. It is clear that having CTX along with niosomes in chitosan hydrogel slightly extends the release rates when compared to the release rates from niosomes alone in chitosan hydrogel. The slower release rates are possibly due to the extra protection that CTX provides for niosomes and enhances their stability.

2.4.3. Transmission Electron Microscopy

To understand the possible interactions between niosome and CTX, TEM imaging was performed for samples of niosomes alone (Figure 2.4a) and niosomes in the presence of CTX (Figure 2.4b). As can be seen in Figure 2.4b, CTX forms micelles and binds to the surface of niosomes. The attachment of CTX to niosomes may be the reason for the extended release rates observed from CTX and niosomes in chitosan hydrogel, as CTX protects niosomes with extra layer and increases their stability.

2.4.4. ATR-FTIR Spectroscopy

Comparative spectra of Niosome, CTX, and CTX+Niosome in the frequency region of 1800-1200 cm^{-1} are shown in Figure 2.5. The most notable peaks in the Niosome spectrum were observed at 1736 cm^{-1} and 1466 cm^{-1} assigned to $\nu(C=O)$ and $\delta(CH_2)$, respectively. Other peaks in the spectrum of Niosome include 1376, 1355, and 1300 cm^{-1} all assigned to CH_2 and CH bending vibrations. A peak at 1246 cm^{-1} in the spectrum of Niosome indicates the $\nu(PO_4^{-3})$ of dicetyl phosphate.

Two prominent bands in the CTX spectrum were observed at 1645 cm^{-1} and 1545 cm^{-1} correspond to amide I (C=O stretch) and amide II (NH bending and CN stretch) α-helical structures, respectively. The band at 1516 cm^{-1} was assigned to $\nu(C-C)$ and $\delta(C-H)$ of Tyrosine ring. Similarly, the 1446 cm^{-1} peak was associated with $\delta(CH_2)$ of Tyrosine and Phenylalanine amino acid side chains present in CTX. The peaks at 1408 cm^{-1} and 1388 cm^{-1} correspond to $\nu(C-N)$ of Glutamine and Methionine and $\delta_w(CH_2)$ of Tyrosine, respectively.

Two significant spectral shifts were observed in the CTX+Niosome spectrum.: 1) the characteristic amide II peak at 1538 cm^{-1} in CTX shifts to 1549 cm^{-1} in CTX+Niosome, 2) the amide I peak at 1648 cm^{-1} in CTX shifts to 1657 cm^{-1} in CTX+Niosome.

It is known that the frequency changes in amide bands correlate with the strength alterations of the hydrogen bonds.[30-32] While an upshift represents weakening of hydrogen bonds in stretching vibrations, it indicates stronger hydrogen bonds for bending vibrations.[31] It has been shown that the shifts of amide II band induced by hydrogen bonding derive predominantly from N-H bending.[33] Therefore, the observed upshift of amide II band in the spectra of CTX+Niosome compared to CTX indicates an increase in N-H hydrogen bonding. This implies that a hydrogen bonding between N-H groups of CTX and C=O and O-H groups of Niosomes may be responsible for the observed binding of CTX to the surface of niosomes shown by TEM imaging. The upshift of amide I (C=O stretch) indicates a decrease in C=O associated intramolecular C=O…N-H hydrogen bonding within CTX. This may be due to the formation of intermolecular hydrogen bonds between N-H groups of CTX and O-H and C=O groups of Niosomes.

2.5. Conclusions

Embedding niosomes in chitosan hydrogel resulted in significant prolonged release profiles specifically after 24 h. Release rate studies also indicated that embedding CTX along with niosomes in chitosan hydrogel results in slightly more extended release rates as compared to the release rates from niosomes alone in chitosan hydrogel. As clearly shown by the TEM images, the attachment of CTX to the surface of niosomes may play a critical role in improving the stability of niosomes and the extended release rates. The interaction of CTX with niosomes was also confirmed by ATR-FTIR studies. These findings suggest that the developed drug delivery system with extended release profiles and distinct tumor targeting features would improve the specific delivery of anticancer drugs to tumor cells.

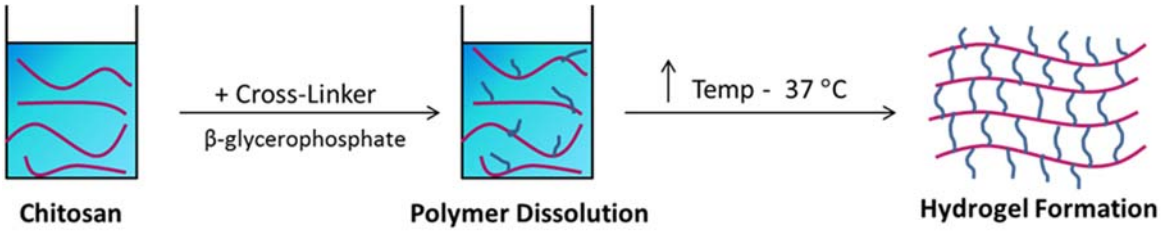

Figure 2.1 Schematic representation of the thermosensitive chitosan hydrogel preparation

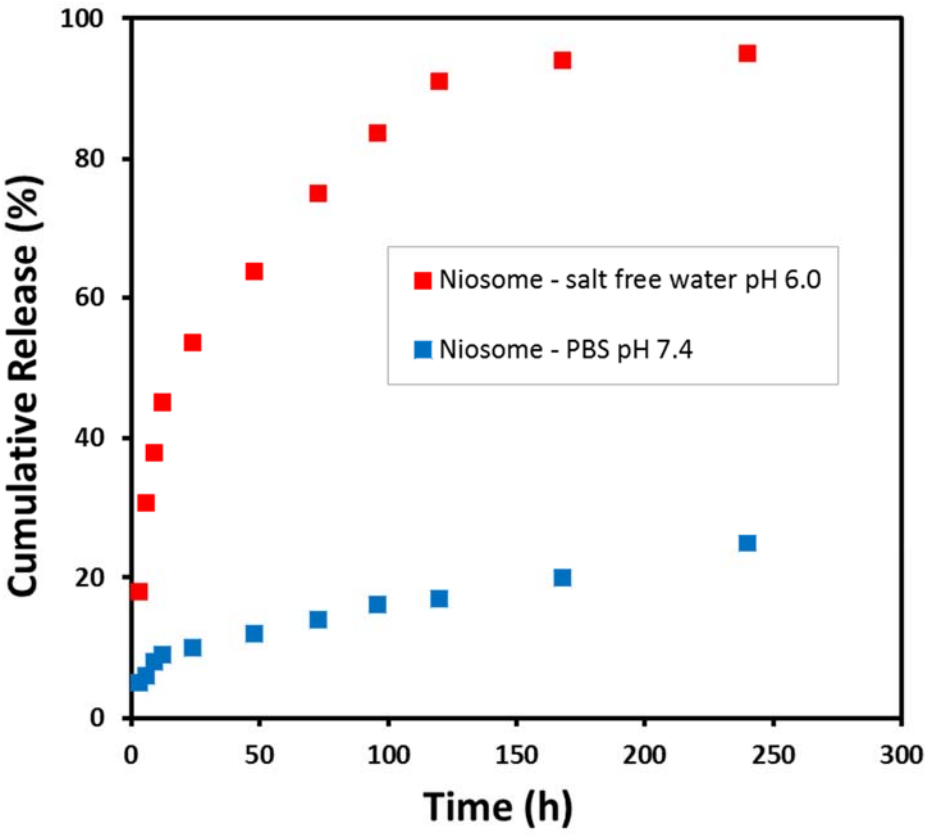

Figure 2.2 Cumulative release profiles of 5,6-carboxyfluorescein from niosomes in salt-free water (pH 6.0) and PBS (pH 7.4)

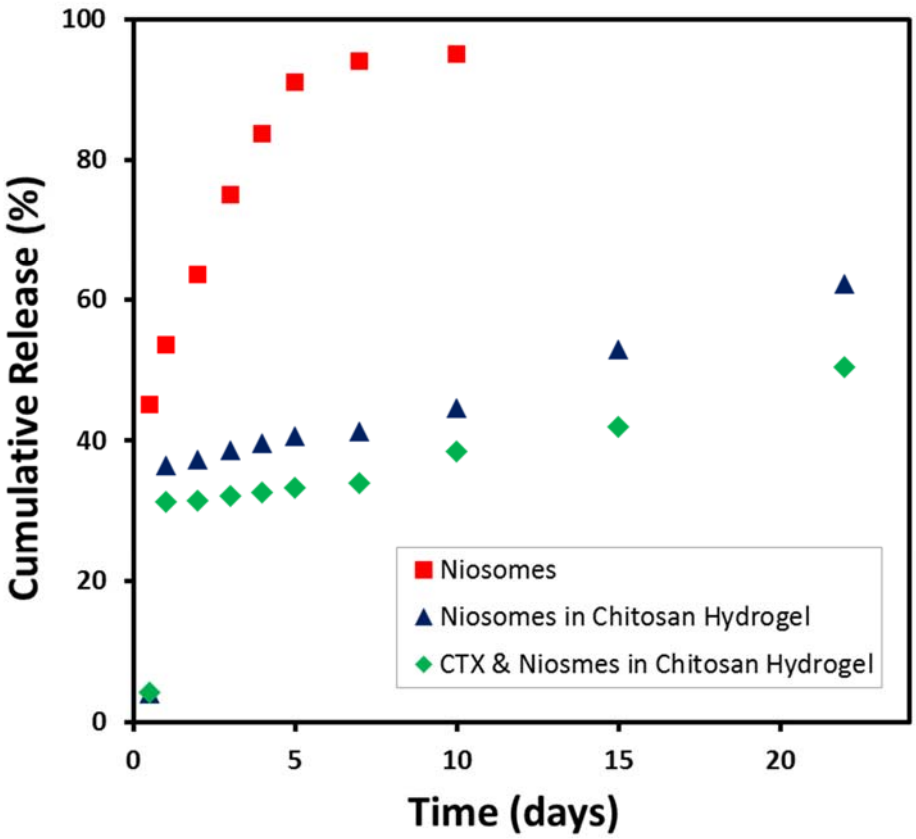

Figure 2.3 Cumulative release profiles of 5,6-carboxyfluorescein from niosomes, niosomes embedded in chitosan hydrogel, and CTX-niosomes embedded in chitosan hydrogel in salt-free water (pH 6.0)

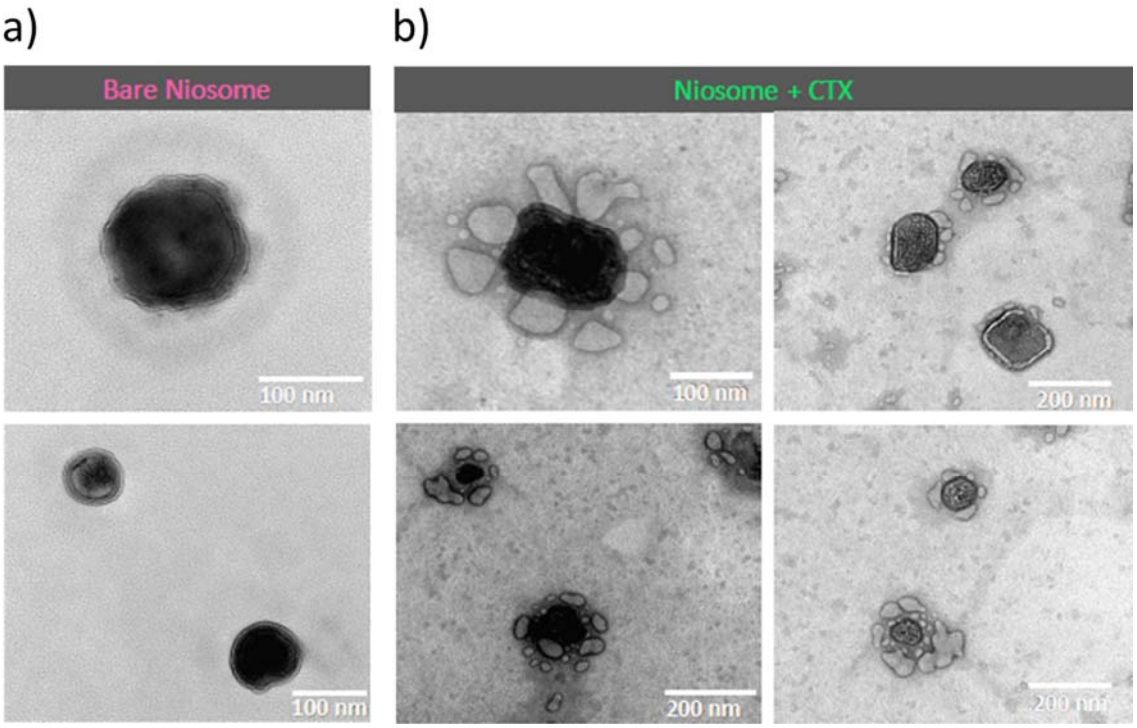

Figure 2.4 TEM images of bare niosomes (a) and niosomes with CTX (b)

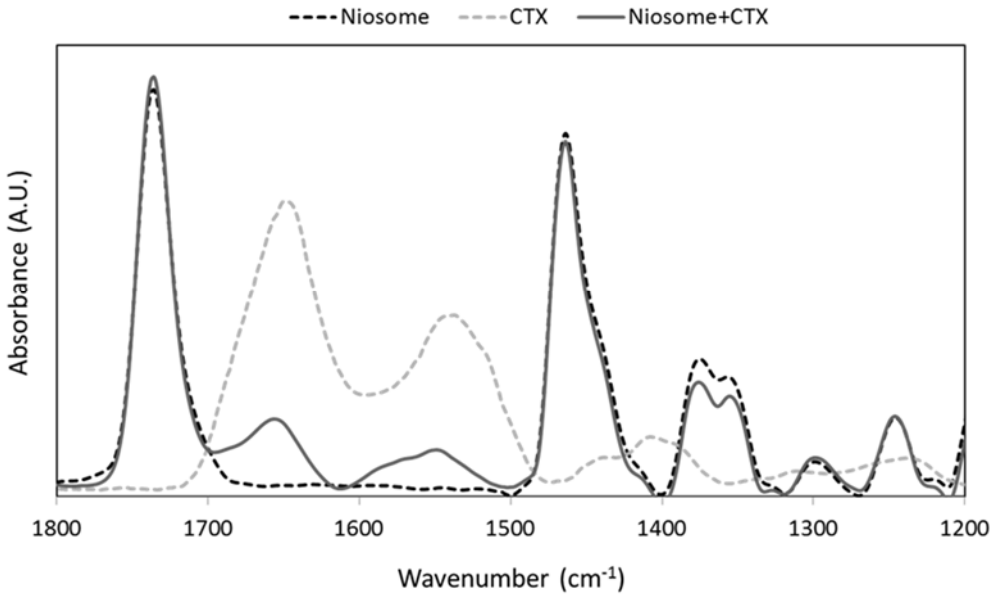

Figure 2.5 ATR-FTIR absorption spectra of niosomes (dashed black), CTX (dashed gray), and niosomes with CTX (solid gray) in frequency region of 1800 cm $^{-1}$–1200 cm $^{-1}$

2.6. References

1. Uchegbu, I.F. and S.P. Vyas, *Non-ionic surfactant based vesicles (niosomes) in drug delivery.* International Journal of pharmaceutics, 1998. **172**(1): p. 33-70.
2. Manosroi, A., et al., *Characterization of vesicles prepared with various non-ionic surfactants mixed with cholesterol.* Colloids and Surfaces B: Biointerfaces, 2003. **30**(1): p. 129-138.
3. Pardakhty, A., J. Varshosaz, and A. Rouholamini, *In vitro study of polyoxyethylene alkyl ether niosomes for delivery of insulin.* International journal of pharmaceutics, 2007. **328**(2): p. 130-141.
4. Bayindir, Z.S. and N. Yuksel, *Characterization of niosomes prepared with various nonionic surfactants for paclitaxel oral delivery.* Journal of pharmaceutical sciences, 2010. **99**(4): p. 2049-2060.
5. Pham, T.T., et al., *Liposome and niosome preparation using a membrane contactor for scale-up.* Colloids and Surfaces B: Biointerfaces, 2012. **94**: p. 15-21.
6. Alsarra, I.A., et al., *Proniosomes as a drug carrier for transdermal delivery of ketorolac.* European journal of pharmaceutics and biopharmaceutics, 2005. **59**(3): p. 485-490.
7. Soussan, E., et al., *Drug delivery by soft matter: matrix and vesicular carriers.* Angewandte Chemie International Edition, 2009. **48**(2): p. 274-288.
8. Williams, E.C., *Smart Packaging: A Novel Technique For Localized Drug Delivery For Ovarian* Cancer. 2012.
9. Rogerson, A., et al., *The distribution of doxorubicin in mice following administration in niosomes.* Journal of pharmacy and pharmacology, 1988. **40**(5): p. 337-342.
10. Sezgin-Bayindir, Z. and N. Yuksel, *Investigation of formulation variables and excipient interaction on the production of niosomes.* AAPS PharmSciTech, 2012. **13**(3): p. 826-835.
11. Varshosaz, J., et al., *Development and physical characterization of sorbitan monoester niosomes for insulin oral delivery.* Drug delivery, 2003. **10**(4): p. 251-262.
12. Dufes, C., et al., *Glucose-targeted niosomes deliver vasoactive intestinal peptide (VIP) to the brain.* International journal of pharmaceutics, 2004. **285**(1): p. 77-85.
13. Walkey, C.D., et al., *Nanoparticle size and surface chemistry determine serum protein adsorption and macrophage uptake.* Journal of the American Chemical Society, 2012. **134**(4): p. 2139-2147.
14. Bhattarai, N., J. Gunn, and M. Zhang, *Chitosan-based hydrogels for controlled, localized drug delivery. Advanced* drug delivery reviews, 2010. **62**(1): p. 83-99.
15. Ganji, F., M. Abdekhodaie, and A.R. SA, *Gelation time and degradation rate of chitosan-based injectable hydrogel.* Journal of sol-gel science and technology, 2007. **42**(1): p. 47-53.
16. Ta, H.T., C.R. Dass, and D.E. Dunstan, *Injectable chitosan hydrogels for localised cancer therapy.* Journal of Controlled Release, 2008. **126**(3): p. 205-216.

17. Falahat, R., et al., *A Cell ELISA for the quantification of MUC1 mucin (CD227) expressed by cancer cells of epithelial and neuroectodermal origin.* Cellular immunology, 2015. **298**(1): p. 96-103.

18. He, P., S.S. Davis, and L. Illum, *In vitro evaluation of the mucoadhesive properties of chitosan microspheres.* International Journal of Pharmaceutics, 1998. **166**(1): p. 75-88.

19. Debin, J.A., J.E. Maggio, and G.R. Strichartz, *Purification and characterization of chlorotoxin, a chloride channel ligand from the venom of the scorpion.* American Journal of Physiology-Cell Physiology, 1993. **264**(2): p. C361-C369.

20. Lyons, S.A., J. O'Neal, and H. Sontheimer, *Chlorotoxin, a scorpion-derived peptide,* specifically *binds to gliomas and tumors of neuroectodermal origin.* Glia, 2002. **39**(2): p. 162-173.

21. Wiranowska, M., L.O. Colina, and J.O. Johnson, *Clathrin-mediated entry and cellular localization of chlorotoxin in human glioma.* Cancer Cell Int, 2011. **11**: p. 27.

22. Veiseh, M., et al., *Tumor paint: a chlorotoxin: Cy5. 5 bioconjugate for* intraoperative *visualization of cancer foci.* Cancer research, 2007. **67**(14): p. 6882-6888.

23. Akcan, M., et al., *Chemical re-engineering of chlorotoxin improves bioconjugation properties for* tumor *imaging and targeted therapy.* Journal of medicinal chemistry, 2011. **54**(3): p. 782-787.

24. Falahat, R., et al., *Enhanced targeted delivery of paclitaxel to tumor cells of epithelial and neuroectodermal origin using chlorotoxin-chitosan nanodelivery system.* Cancer Research, 2015. **75**(15 Supplement): p. 3677-3677.

25. Dardevet, L., et al., *Chlorotoxin: A Helpful Natural Scorpion Peptide to Diagnose Glioma* and *Fight Tumor Invasion.* Toxins, 2015. **7**(4): p. 1079-1101.

26. Butte, P.V., et al., *Near-infrared imaging of brain tumors using the Tumor Paint BLZ-100 to achieve near-complete resection of brain tumors.* Neurosurgical focus, 2014. **36**(2): p. E1.

27. Sun, C., et al., *Tumor-targeted drug delivery and MRI contrast enhancement by chlorotoxin-conjugated iron oxide nanoparticles.* Nanomedicine, 2008. **3**(4): p. 495-505.

28. Xiang, Y., et al., *Chloride channel-mediated brain glioma targeting of chlorotoxin-modified doxorubicine-loaded liposomes.* Journal of controlled release, 2011. **152**(3): p. 402-410.

29. Falahat, R., et al., *Targeted delivery to tumor cells by using tunable nano-delivery system with chlorotoxin.* Cancer Research, 2013. **73**(8 Supplement): p. 4523-4523.

30. Tamm, L.K. and S.A. Tatulian, *Infrared spectroscopy of proteins and peptides in lipid bilayers.* Quarterly reviews of biophysics, 1997. **30**(04): p. 365-429.

31. Barth, A., *Infrared spectroscopy of proteins.* Biochimica et Biophysica Acta (BBA)-Bioenergetics, 2007. **1767**(9): p. 1073-1101.

32. Takekiyo, T., et al., *Pressure stability of the α-helix structure in a de novo designed protein (α-l-α) 2 studied by FTIR spectroscopy.* Biopolymers, 2007. **85**(2): p. 185-188.

33. Myshakina, N.S., Z. Ahmed, and S.A. Asher, *Dependence of amide vibrations on hydrogen bonding.* The Journal of Physical Chemistry B, 2008. **112**(38): p. 11873-11877.

CHAPTER 3: CHARACTERIZATION OF PACLITAXEL-LOADED NIOSOMES EMBEDDED IN CHITOSAN HYDROGELS: THE INFLUENCE OF CROSSLINKER CONTENT AND PH

3.1. Abstract

We report the development and characterization of a localized drug delivery system consisting of paclitaxel-loaded non-ionic surfactant vesicles (PTX-loaded niosomes) embedded in a thermosensitive chitosan hydrogel. This system represents a new approach in cancer therapy through a sustained and controlled delivery of PTX to tumor sites.

The characterization of prepared PTX-loaded niosomes was performed in terms of morphological assessments and encapsulation efficiency measurements. Chitosan hydrogels (L-Ch, M-Ch, and H-Ch) were prepared with various crosslinker contents in their formulations. The PTX release from chitosan hydrogels containing PTX-loaded niosomes was evaluated in a release medium at 37 ^{o}C with pH 7.4 or 6.3 representing the extracellular pH of a normal tissue or tumor environment. The release studies showed a prolonged release of PTX form chitosan hydrogels containing PTX-loaded niosomes with similar release profiles for L-Ch and M-Ch hydrogels.

The mathematical modeling of the PTX release data was performed using the Peppas-Korsmeyer model to understand the mechanisms of PTX release from chitosan hydrogels containing PTX-loaded niosomes. A combination of diffusion-controlled and swelling-controlled

release also known as the anomalous transport was identified as the dominant release mechanism only for L-Ch hydrogels at pH 6.3.

Swelling studies of the chitosan hydrogels were also performed in the same conditions used for the drug release studies. Swelling of chitosan hydrogels was observed for the formulations with low and medium crosslinker contents (L-Ch and M-Ch) when incubated at pH 6.3. No significant difference in the swelling ratio of chitosan hydrogels with a high crosslinker content (H-Ch) was found at pH 6.3 or 7.4.

Together the results suggest that the chitosan hydrogels containing PTX niosomes could improve the chemotherapeutic benefits of PTX by providing a localized, controlled, and prolonged delivery in solid tumors.

3.2. Introduction

Paclitaxel (PTX) is one of the most effective chemotherapeutic agents in the treatment of many cancers including breast, ovarian, colon, and non-small-cell lung cancers [1-4]. Due to the hydrophobicity of PTX, several organic formulations such as polyethoxylated castor oil (Cremophor® EL) have been employed to improve the solubility of PTX [5]. However, many undesired side effects of Cremophor EL have been reported in patients undertaking this treatment [6-8].

Among different strategies, encapsulation of PTX in submicronic colloidal systems such as liposomes, microspheres, micelles, and polymeric nanoparticles has been widely studied to address this problem [9-11]. Despite having many promising features, poor stability and low bioavailability of the nanoparticles in tumor sites have hindered their effectiveness when administered systemically [12-14].

An alternative approach is the use of localized drug delivery systems in which chemotherapeutic agents are encapsulated in a matrix designed in various forms including hydrogels, films, wafers, and rods [15]. Among different *in situ* drug delivery systems, thermoresponsive chitosan hydrogels in particular have gained special attention [16-18]. Their initial liquid state at room temperature allows them to be applied through a simple injection into the specific body sites. After injection, they transform into a soft gel at body temperature which provides a localized drug release within the tumor sites [19]. In addition, they are known to exhibit antibacterial, biocompatible, biodegradable, and mucoadhesive properties [20-22]. Thermoresponsive chitosan hydrogel systems have been prepared with different chemical or physical crosslinking methods [16, 23].

Despite all the outstanding properties, some limitations are associated with their use [24] First, due to the presence of high amount of water in the hydrogel network, the encapsulation of hydrophobic drugs such as PTX is often difficult [24]. Second, the large pores in their network structure can cause relatively fast release rates particularly for small molecule drugs [25]. To address these challenges, an incorporation of a secondary drug carrier such as liposomes, micelles, and other particle based vehicles into the hydrogel network has been considered [26-28].

In this study, we present the development of a localized drug delivery system consisting of PTX-loaded non-ionic surfactant vesicles (niosomes) embedded in a thermoresponsive chitosan hydrogel network. Similar to liposomes, niosomes have a spherical bilayer structure with hydrophilic core and hydrophobic shell allowing them to be used for encapsulating both hydrophilic and hydrophobic drugs [29-31].

The PTX-loaded niosomes were prepared using the thin film hydration method and characterized by performing morphological assessments and encapsulation efficiency measurements. Chitosan hydrogels containing PTX-loaded niosomes with various crosslinker contents were prepared. The PTX release studies were performed in a release medium with pH 7.4 or 6.3. The PTX release kinetics were evaluated by fitting the release data into the Peppas-Korsmeyer model. Swelling and biodegradability are among the important characteristics of chitosan hydrogels [21, 38]. Therefore, swelling behavior and degradation rates of chitosan hydrogels were also studied.

3.3. Materials and Methods

3.3.1. Materials

Span 60, cholesterol, dicetyl phosphate (DCP), and medium molecular weight chitosan were purchased from Sigma-Aldrich (St. Louis, MO). The crosslinking agent, β-glycerophosphate disodium salt (β-GP) was purchased from Calbiochem EMD Biosciences (La Jolla, CA). Paclitaxel (PTX) was obtained from LC laboratories (Woburn, MA) and used as a chemotherapeutic drug. All the other agents were purchased from Fisher Scientific (Fair Lawn, NJ).

3.3.2. Preparation of PTX-loaded Niosomes

PTX-loaded niosomes were prepared by the thin film hydration method [31]. Briefly, span 60, cholesterol and DCP (1:1:0.1 molar ratio) were dissolved in chloroform and transferred to a 50 mL round bottom flask. PTX at 0.5 to 10 mol% with respect to total niosome content was added to this solution. To make a thin film, chloroform was removed by rotating the flask using a Buchi rotary evaporator (Flawil, Switzerland) in a water bath at 60^{o}C. The thin film was left in the fume hood overnight to remove any remaining traces of the chloroform. The dried thin film

was hydrated with 0.01 M phosphate buffer saline (PBS) containing 0.1% (v/v) Tween 80 in the rotary evaporator for 1 h at 60ºC. Size reduction process was performed using an Avanti Polar Lipids Mini-Extruder (Alabaster, AL) by passing the niosome suspension through 800, 400 or 80 nm polycarbonate membrane filters (Nuclepore Corp., Pleasanton, CA) at 60ºC. The un-trapped drug was separated from niosome suspension using a Beckman XL-100 ultracentrifuge (Fullerton, CA) operating at 60,000 rpm for 1 h. PTX-loaded niosomes in the precipitate were resuspended in 0.01 M PBS and kept at 4ºC for the future experiments.

3.3.3. Characterization of PTX-loaded Niosomes

3.3.3.1. Transmission Electronic Microscopy

The morphology of PTX-loaded niosomes was observed using transmission electron microscopy (TEM). The TEM samples were prepared by placing a droplet of niosome suspension (after appropriate dilution) on a 150-mesh carbon coated formvar copper grid (Electron Microscopy Sciences, Hatfield, PA) and allowed to adhere for 1 min. Following the removal of the excess solution using a filter paper, the samples were placed in a vacuum chamber for 10 min at 40ºC. The samples were then viewed under an electron microscope (FEI Morgagni TEM) with an operating voltage of 80 kV.

3.3.3.2. Encapsulation Efficiency

The encapsulation efficiency of PTX in niosomes was determined using a Shimadzu HPLC system consisting of an automatic sample injector (SIL-10A), system controller (SCL-10A VP), pump (LC-10AT VP), degasser (DGU- 14A), and UV-VIS detector (SPD-10A VP). Chromatographic separation of PTX was achieved using a reverse phase C18 column (ODS-3V, GL Sciences). The mobile phase consisted of acetonitrile and water (60:40 v/v). The flow rate was 1.0 ml/min and the injection volume was 20 µl. The UV detection was performed at a

wavelength of 227 nm. Prior to HPLC analysis, PTX was extracted from the niosomes using dichloromethane (DCM). Briefly, 2 ml of prepared niosome solution was extracted with 3×1 ml of DCM. Following the evaporation of DCM under a stream of nitrogen, the extracted PTX was dissolved in 4 ml of acetonitrile and quantitated using the HPLC system. The extraction efficiency was determined by extracting a known amount of PTX following the same procedure as described above. The encapsulation efficiency was defined as the ratio of PTX encapsulated in niosomes to the initial amount of PTX used in niosomes preparation:

$$\text{Encapsulation Efficiency } (\%) = \frac{\text{Amount of PTX encapsulated in niosomes}}{\text{Initial amount of PTX used in niosome preparation}} \times 100 \quad \ldots\ldots\ldots\ldots\ldots\ldots(1)$$

3.3.4. Preparation of Chitosan Hydrogels

A 2.8% (w/v) chitosan solution was prepared by dissolving chitosan powder in 1.5 ml of 0.1 M hydrochloric acid at room temperature. A β-GP solution at three different concentrations of 55%, 65%, or 83% (w/v) was prepared in 0.5 ml of deionized water and kept at 4^{o}C for 1 h prior to crosslinking along with the chitosan solution. While stirring continuously, the cold β-GP solution was added drop wise to the cold chitosan solution. After adding the last drop, the final solution was stirred for 10 min. 0.7 ml of niosome suspension was added into the chitosan and β-GP mixture followed by 5 min stirring. The prepared mixture was transferred into a 5 ml beaker and placed in a water bath at 37 ^{o}C and allowed to gel. Chitosan hydrogels were named as L-Ch, M-Ch, or H-Ch representing low (0.33 M), medium (0.39 M) or high (0.50 M) concentrations of β-GP in hydrogel formulations.

3.3.5. *In vitro* Release Studies

Prepared samples of chitosan hydrogel containing PTX-loaded niosomes were placed into 30 ml of PBS (pH=7.4 or 6.3) at 37^{o}C. 0.1% (v/v) Tween 80 was also included in the release medium as a sink-inducing agent to facilitate the solubility of PTX [4, 5]. At predetermined time

intervals, the entire release medium was collected and replaced with equal amount of fresh medium at 37ºC. The collected samples were pretreated using the DCM extraction procedure and then introduced to the HPLC system as described in section 3.3.2.

3.3.6. Mathematical Analysis of the Drug Release Kinetics

To determine the release kinetics of PTX from niosome embedded chitosan hydrogel complexes and the related transport mechanisms, the obtained drug release rate data were fitted into the Peppas-Korsmeyer semi-empirical equation also known as power law equation [32]:

$$Q = \left(\frac{M_t}{M}\right) = k \times t^n \quad \text{.....(2)}$$

where Q is the fractional drug release into the medium at time t (h), M_t is the amount of drug released at time t, M is the total amount of drug, k is the kinetic constant incorporating structural and geometric characteristics of the drug delivery system, t is the release time (h) and n is the diffusion exponent characterizing the drug release mechanism.

Based on the diffusion exponent, the drug release mechanisms from a hydrogel system can be classified as [32, 33]:

1- Quasi-Fickian diffusion, $n < 0.5$

2- Fickian diffusion, $n = 0.5$

3- Anomalous transport, $0.5 < n < 1$

4- Case II transport (swelling-controlled drug release), $n = 1$

3.3.7. Swelling Studies

The swelling behavior of chitosan hydrogels was studied as follows.Uniform disk-shaped chitosan hydrogels were immersed into 30 ml PBS with pH = 7.4 or 6.3 at 37ºC. At specific time points the hydrogels were taken out from the swelling medium and blotted using a filter paper to

remove the excess surface water. This was followed by measuring their diameter. The swelling ratio was defined as:

$$\% \text{ Swelling ratio} = \frac{D_S}{D_d} \quad \text{.....(3)}$$

D_s and D_d correspond to the diameter of the hydrogel at the swollen and dried states, respectively.

3.3.8. Enzymatic Degradation

Samples of chitosan hydrogel were prepared using the same method described in the previous section and placed into 30 ml of PBS (pH=7.4) with 0.02 mg/ml lysozyme at 37ºC. At specified time points samples were removed from the medium, rinsed with distilled water, and dried under vacuum. Enzymatic degradation of chitosan hydrogel samples is then quantified using the following equation:

$$\% \, Enzymatic \; Degradation \; (t) = \frac{[W_0 - W_t]}{W_0} \quad \text{.....(4)}$$

W_0 reflects the initial weight of the chitosan hydrogel and W_t is the weight of the dried hydrogel at time t.

3.4. Results and Discussion

3.4.1. Characterization of PTX-loaded Niosomes

The mean diameter and encapsulation efficiency of PTX in PTX-loaded niosomes as a function of the membrane pore size used in the extrusion process are shown in Figure 3.1a. Niosomes with a mean diameter of 85 nm were prepared using a membrane with a pore size of 80 nm. A decrease in encapsulation efficiencies was observed for niosomes when smaller membrane pore sizes used in the extrusion process which correlated well with the decrease of niosome sizes.

TEM image of a PTX-loaded niosome which was extruded through 80 nm membrane with a diameter of less than 100 nm is shown in Figure 3.1b.

3.4.2. *In vitro* Release Studies

The cumulative release profiles of L-Ch, M-Ch and H-Ch hydrogels containing PTX-loaded niosomes in PBS with pH=7.4 and 6.3 are depicted in Figure 3.2a-c. Slow and controlled PTX release profiles were observed for all hydrogels with various cross-linker content in both release media (pH=6.3 and 7.4). All the hydrogels indicated slower release profiles in the release medium with pH=6.3 as compared to the release medium with pH=7.4. The PTX cumulative release profiles from L-Ch and M-Ch hydrogels were very similar particularly in PBS with pH=6.3 for which only 38% and 37% of the cumulative release occurred after 40 days, respectively. Higher amounts of PTX release were observed for L-Ch (44%) and M-Ch (43%) incubated in PBS with pH=7.4 for 40 days as compared to the hydrogels incubated in PBS with pH=6.3.

H-Ch hydrogels indicated significantly slower release profiles of PTX compared to both L-Ch and M-Ch hydrogels. Only 33% and 36% of the PTX release occurred from H-Ch hydrogels after 40 days in the release media with pH=6.3 and 7.4, respectively. As can be seen in Figure 3.2a-c, unlike L-Ch and M-Ch the difference between the release profiles of H-Ch in PBS with pH 6.3 and 7.4 were not as significant as those observed for L-Ch and M-Ch hydrogels.

The PTX release rates for all chitosan formulations were slower in PBS with pH 6.3 than PBS with pH 7.4.This phenomenon can be explained as follows. As niosomes contain dicetyl phosphate, a negative charge inducer, they possess negative zeta potential values [31, 34, 35]. Therefore, they are likely to interact with positively charged NH_2 groups in chitosan hydrogel when incubated in PBS with low pH (6.3). The slower release rates observed for the chitosan

hydrogels containing PTX-niosomes in PBS with pH 6.3 compared to PBS with pH 7.4 might be due to the possible interactions between negatively charged niosomes and NH_3^+ groups of chitosan hydrogels when incubated in PBS with pH 6.3.

3.4.3. Mathematical Analysis of the Drug Release Kinetics

The drug release kinetics of PTX from L-Ch, M-Ch, and H-Ch hydrogels containing PTX-loaded niosomes were further assessed by fitting the PTX release data to the Peppas-Korsmeyer model. The corresponding theoretical curves are presented as dashed lines in Figure 3.2a-c. The model coefficients (k and n) and the squared correlation coefficient (R^2) are listed in Table 3.1. A good correlation with the Peppas-Korsmeyer model ($R^2 > 0.91$) was obtained for all the PTX release data.

Based on the derived release exponent values ($0.5 < n < 1$), the PTX release can be classified as an anomalous transport for L-Ch hydrogels when incubated in PBS with pH 6.3 indicating that the drug release from this system was a combination of diffusion-controlled (n=0.5) and swelling-controlled (n =1) release. The drug release from M-Ch and H-Ch hydrogels containing PTX-loaded niosomes in PBS with pH 6.3 was identified as Fickian diffusion (n=0.5). When incubated in PBS with pH 7.4, n< 0.5 was obtained for all hydrogels (L-Ch, M-Ch, and H-Ch) identifying the PTX release mechanism as quasi-Fickian diffusion.

3.4.4. Swelling Studies

The swelling studies were performed on the L-Ch, M-Ch, and H-Ch hydrogels containing PTX-loaded niosomes which were incubated in PBS with pH=7.4 and 6.3 for specified time points to analyze the effect of crosslinker content on the swelling behavior of chitosan hydrogels at various pH. The swelling ratio was defined as the diameter of the swollen hydrogel to the diameter of the hydrogel at the dried state.

Figure 3.3 shows a comparative representation of L-Ch, M-Ch, and H-Ch hydrogels after 24 h of incubation in PBS with pH=7.4 and 6.3. As can be seen in Figure 3.3, the swelling behavior of chitosan hydrogels varies as a function of the crosslinker content and pH of the release medium.

While L-Ch and M-Ch hydrogels exhibited increased swelling ratios at pH=6.3 when compared to pH=7.4, no significant difference was observed for H-Ch hydrogels at various pH conditions.

Swelling ratios of these hydrogels at pH=7.4 and 6.3 as a function of time are shown in Figure 3.4. The highest swelling ratio was observed for L-Ch hydrogel after 24 h of incubation in PBS with pH=6.3. The swelling ratios decreased after 24 h and all the hydrogels reached equilibrium swelling after 7 days. Similar to the swelling ratios at 24 h, L-Ch hydrogels at pH=6.3 had the highest swelling ratios among other hydrogels for all incubation time periods. These results are in agreement with the previous studies in which the swelling of chitosan hydrogels has been reported to be a function of crosslinker content and the pH of the release medium [37].

At low pH (pH < 6.5), a protonation of amino groups in chitosan hydrogels occur. Therefore, the observed swelling of L-Ch and M-Ch hydrogels at pH 6.3 can be explained as an increase in the protonation and repulsion of chitosan free ammonium groups.

3.4.5. Enzymatic Degradation

Biodegradability is one of the important characteristics of chitosan hydrogels [21, 38]. To determine the degradation rate of chitosan hydrogels, M-Ch hydrogels were incubated in PBS with and without 0.02 mg/ml lysozyme concentration at 37 ^{o}C. As can be seen in Figure 3.5,

around 75% degradation occurred for M-Ch hydrogel after49 days of incubation in PBS with 0.02 mg/ml lysozyme.

Degree of deacetylation (DDA) has been defined an important factor in degradation of chitosan hydrogels [39, 40]. In this study chitosan with DDA of 85% was used. Chitosan with high DDA (71% to 93%) has been shown to experience slow degradation rates.

3.5. Conclusions

We have prepared thermosensitive chitosan hydrogels containing PTX-loaded niosomes with various amount of crosslinker in their formulations. We have shown that the incorporation of PTX-niosomes in chitosan hydrogels resulted in prolonged release profiles which lasted for more than 40 days in a pH-dependent manner. While L-Ch and M-Ch hydrogels indicated similar PTX release profiles, relatively slower release rates (around 10%) were found for H-Ch hydrogels. The release mechanism was identified as anomalous transport (a combination of diffusion-controlled and swelling-controlled release) for L-Ch hydrogels when incubated in PBS with pH 6.3. The significant effect of crosslinker content on physical properties and release profiles of chitosan hydrogels was further confirmed by swelling studies. Major changes in swelling behavior were observed for L-Ch and M-Ch chitosan hydrogels with a small physiologically relevant pH change. Together, the results of this study show promise for the development of a localized drug delivery system which can be used for a sustained and controlled delivery of PTX at the tumor sites.

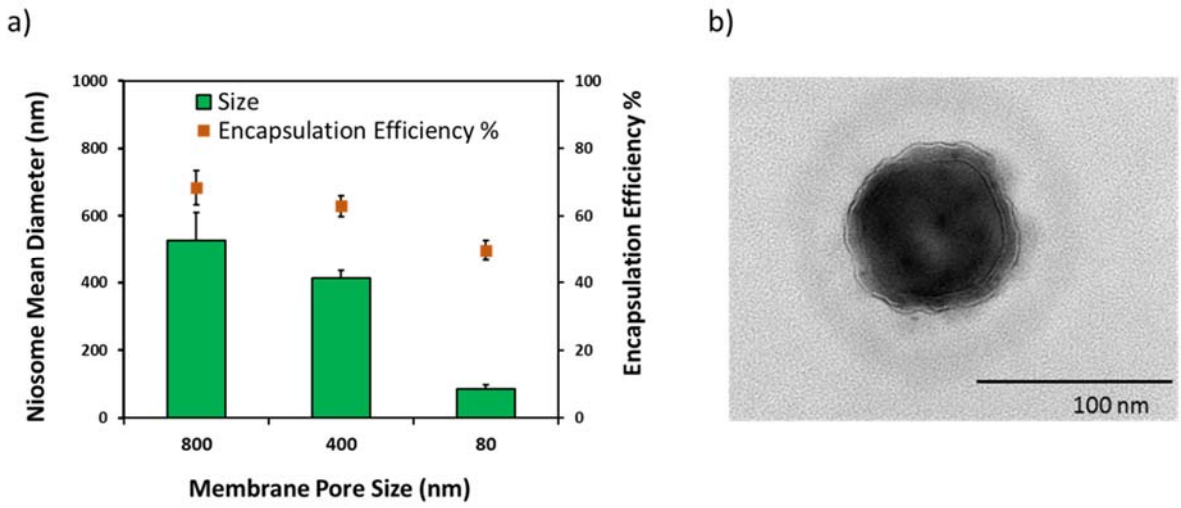

Figure 3.1 Mean diameter and encapsulation efficiency of niosomes as a function of membrane pore size used in the extrusion process (a), TEM image of a PTX-loaded niosome with a diameter of less than 100 nm (b)

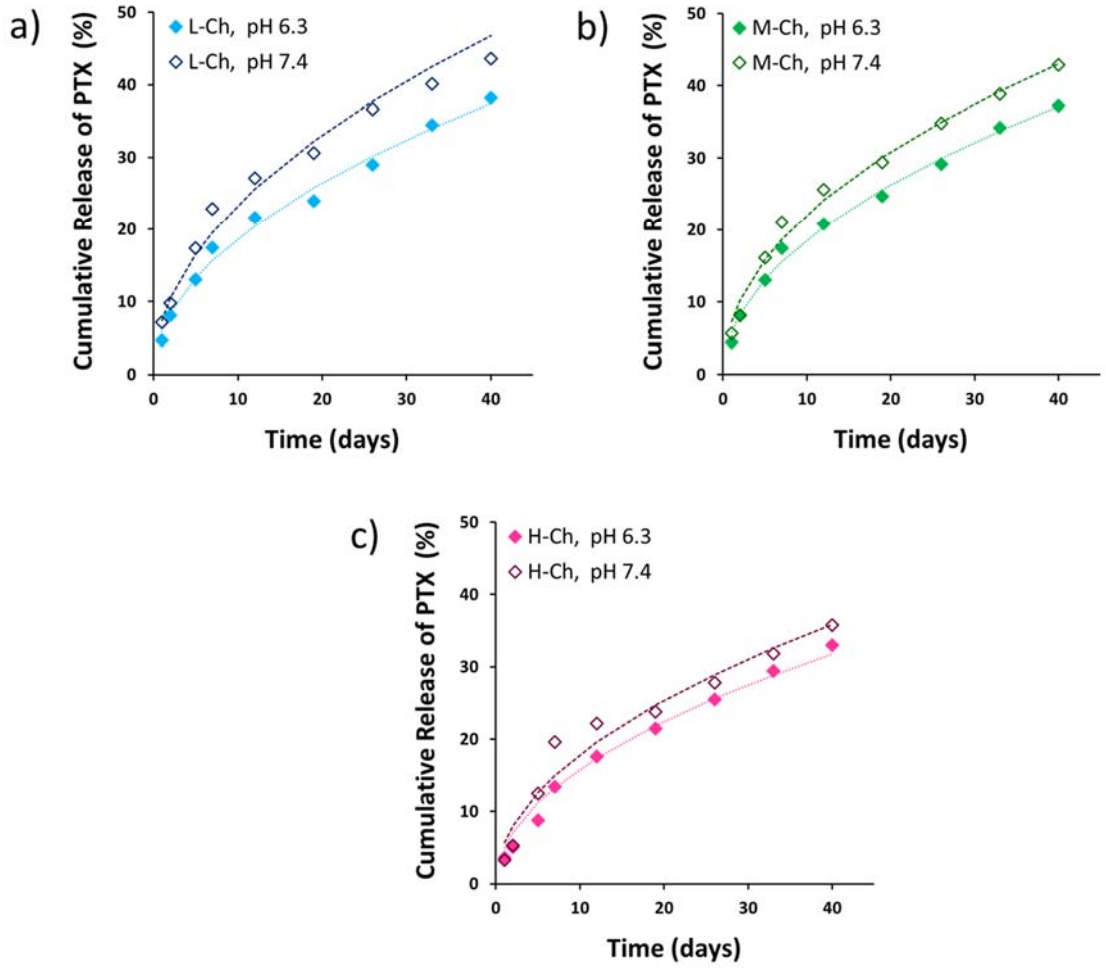

Figure 3.2 Cumulative release profiles of PTX from L-Ch Nio (a), M-Ch Nio (b), and H-Ch Nio (c) in PBS with pH=7.4 or 6.3. The dashed lines represent the corresponding theoretical curves derived from Korsmeyer-Peppas model.

Table 3.1 Kinetic assessment of drug release from chitosan hydrogels containing PTX-loaded niosomes using Korsmeyer-Peppas model

Sample	Korsmeyer-Peppas model			Drug release mechanism
	k	n	R^2	
L-Ch Nio - PBS pH =6.3	1.18	0.57	0.98	Anomalous transport
L-Ch Nio - PBS pH =7.4	1.88	0.46	0.91	Quasi-Fickian diffusion
M-Ch Nio - PBS pH =6.3	1.21	0.50	0.98	Fickian diffusion
M-Ch Nio - PBS pH =7.4	1.59	0.48	0.97	Quasi-Fickian diffusion
H-Ch Nio - PBS pH =6.3	1.01	0.50	0.92	Fickian diffusion
H-Ch Nio - PBS pH =7.4	1.20	0.49	0.92	Quasi-Fickian diffusion

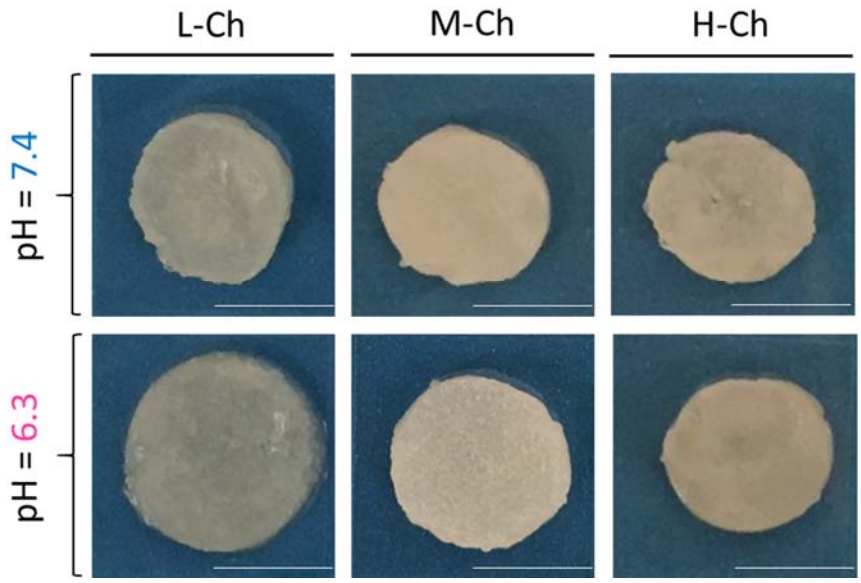

Figure 3.3 Comparative representation of swelling behavior of L-Ch, M-Ch, and H-Ch hydrogels after 24 h of incubation in PBS with pH=7.4 or 6.3. The scale bars correspond to 1 cm.

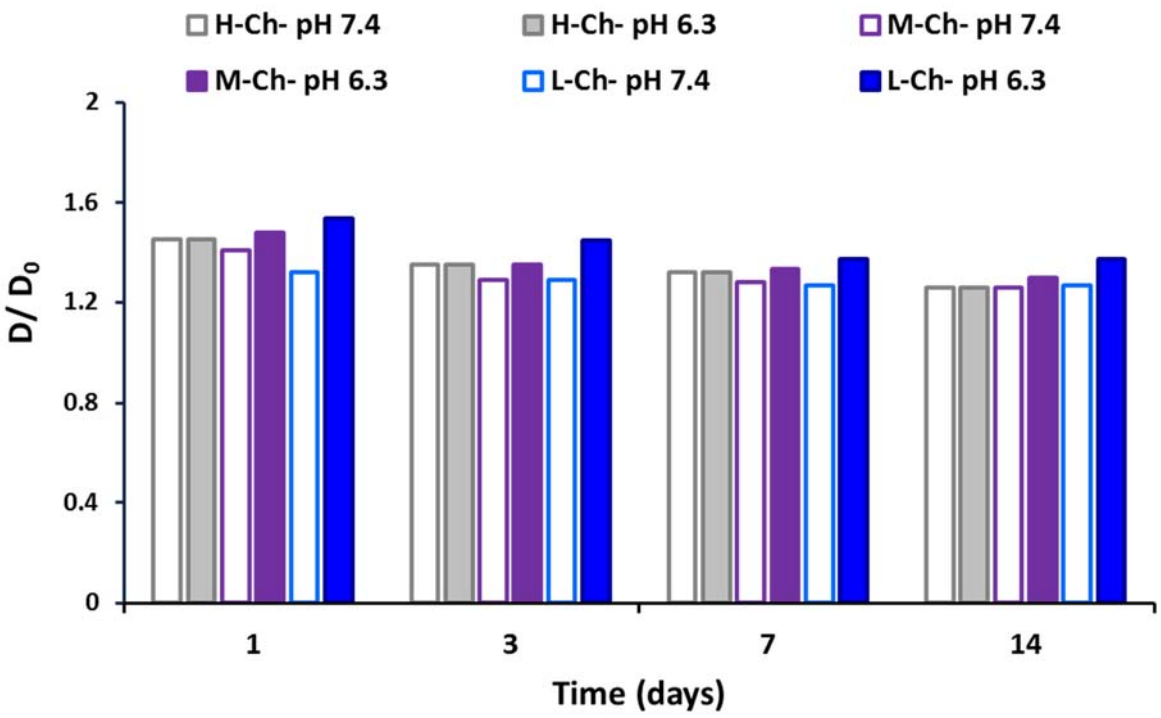

Figure 3.4 Swelling ratios of L-Ch, M-Ch, and H-Ch hydrogels at pH=7.4 and 6.3.

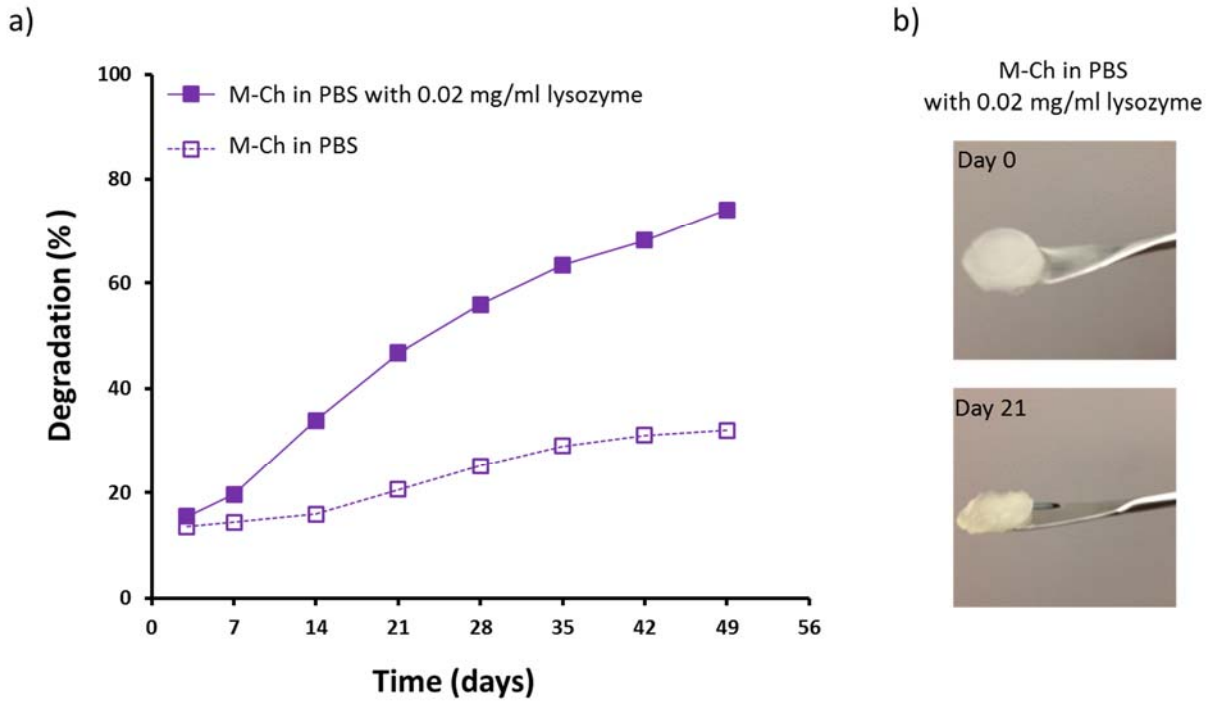

Figure 3.5 Degradation of M-Ch, hydrogels as a function of time incubated in PBS with 0.02 mg/ml lysozyme (filled purple) and PBS (open purple) at pH=7.4 (a) and images of M-Ch hydrogels prior and 21 days after incubation in PBS with 0.02 mg/ml lysozyme (b)

3.6. References

1. Panchagnula, R., *Pharmaceutical* aspects *of paclitaxel.* International Journal of Pharmaceutics, 1998. **172**(1): p. 1-15.
2. Kubota, T., et al., *Antitumor activity of paclitaxel against human breast carcinoma xenografts serially transplanted into nude mice.* Journal of surgical oncology, 1997. **64**(2): p. 115-121.
3. Hu, L., et al., *Inhibition of phosphatidylinositol 3'-kinase increases efficacy of paclitaxel in in vitro* and *in vivo ovarian cancer models.* Cancer research, 2002. **62**(4): p. 1087-1092.
4. Langer, C.J., et al., *Paclitaxel and carboplatin in combination in the treatment of advanced non-small*-cell *lung cancer: a phase II toxicity, response, and survival analysis.* Journal of clinical oncology, 1995. **13**(8): p. 1860-1870.
5. Gelderblom, H., et al., *Cremophor EL: the drawbacks and advantages of vehicle selection for drug* formulation. European Journal of Cancer, 2001. **37**(13): p. 1590-1598.
6. Weiss, R.B., et al., *Hypersensitivity reactions from taxol.* Journal of Clinical Oncology, 1990. **8**(7): p. 1263-1268.
7. Szebeni, J., C.R. Alving, and F.M. Muggia, *Complement activation by Cremophor EL as a possible contributor to hypersensitivity to paclitaxel: an in vitro study.* Journal of the national cancer institute, 1998. **90**(4): p. 300-306.
8. Wang, J., D. Mongayt, and V.P. Torchilin, *Polymeric micelles for delivery of poorly soluble drugs: preparation and anticancer activity in vitro of paclitaxel incorporated into mixed micelles based on poly (ethylene glycol)-lipid conjugate and positively charged lipids.* Journal of drug targeting, 2005. **13**(1): p. 73-80.
9. Yang, T., et al., *Preparation and evaluation of paclitaxel-loaded PEGylated immunoliposome.* Journal of Controlled Release, 2007. **120**(3): p. 169-177.
10. Liggins, R.T. and H.M. Burt, *Paclitaxel-loaded poly (L-lactic acid) microspheres 3: blending low and high molecular weight polymers to control morphology and drug release.* International journal of pharmaceutics, 2004. **282**(1): p. 61-71.
11. Danhier, F., et al., *Paclitaxel-loaded PEGylated PLGA-based nanoparticles: in vitro and in vivo* evaluation. Journal of Controlled Release, 2009. **133**(1): p. 11-17.
12. Walkey, C.D., et al., *Nanoparticle size and surface chemistry determine serum protein adsorption and macrophage uptake.* Journal of the American Chemical Society, 2012. **134**(4): p. 2139-2147.
13. Moghimi, S.M., A.C. Hunter, and J.C. Murray, *Long-circulating and target-specific nanoparticles: theory to practice.* Pharmacological reviews, 2001. **53**(2): p. 283-318.
14. Davis, M.E. and D.M. Shin, *Nanoparticle therapeutics: an emerging treatment modality for cancer.* Nature reviews Drug discovery, 2008. **7**(9): p. 771-782.

15. Wolinsky, J.B., Y.L. Colson, and M.W. Grinstaff, *Local drug delivery strategies for cancer treatment: gels, nanoparticles, polymeric films, rods, and wafers.* Journal of controlled release, 2012. **159**(1): p. 14-26.

16. Ta, H.T., C.R. Dass, and D.E. Dunstan, *Injectable chitosan hydrogels for localised cancer therapy.* Journal of Controlled Release, 2008. **126**(3): p. 205-216.

17. Bhattarai, N., J. Gunn, and M. Zhang, *Chitosan-based hydrogels for controlled, localized drug delivery.* Advanced drug delivery reviews, 2010. **62**(1): p. 83-99.

18. Yu, L. and J. Ding, *Injectable hydrogels as unique biomedical materials.* Chemical Society Reviews, 2008. **37**(8): p. 1473-1481.

19. Ruel-Gariépy, E., et al., *A thermosensitive chitosan-based hydrogel for the local delivery of paclitaxel.* European Journal of Pharmaceutics and Biopharmaceutics, 2004. **57**(1): p. 53-63.

20. Ahmadi, R. and J.D. de Bruijn, *Biocompatibility and gelation of chitosan–glycerol phosphate hydrogels.* Journal of Biomedical Materials Research Part A, 2008. **86**(3): p. 824-832.

21. Jin, R., et al., *Injectable chitosan-based hydrogels for cartilage tissue engineering.* Biomaterials, 2009. **30**(13): p. 2544-51.

22. Jauhari, S. and A.K. Dash, *A mucoadhesive in situ gel delivery system for paclitaxel.* AAPS PharmSciTech, 2006. **7**(2): p. E154-E159.

23. Klouda, L. and A.G. Mikos, *Thermoresponsive hydrogels in biomedical applications.* European Journal of Pharmaceutics and Biopharmaceutics, 2008. **68**(1): p. 34-45.

24. Hoare, T.R. and D.S. Kohane, *Hydrogels in drug delivery: progress and challenges.* Polymer, 2008. **49**(8): p. 1993-2007.

25. Pan, W. and Z. Yang, *Thermoreversible Pluronic® F127-based hydrogel containing liposomes for the controlled delivery of paclitaxel: in vitro drug release, cell cytotoxicity, and uptake studies.* International journal of nanomedicine, 2011. **6**: p. 151-166.

26. Wang, C., N.T. Flynn, and R. Langer, *Controlled structure and properties of thermoresponsive nanoparticle–hydrogel composites.* Advanced Materials, 2004. **16**(13): p. 1074-1079.

27. Ruel-Gariepy, E., et al., *Thermosensitive chitosan-based hydrogel containing liposomes for the delivery of hydrophilic molecules.* Journal of Controlled Release, 2002. **82**(2): p. 373-383.

28. Segovia, N., et al., *Hydrogel doped with nanoparticles for local sustained release of siRNA in breast cancer.* Advanced healthcare materials, 2015. **4**(2): p. 271-280.

29. Uchegbu, I.F. and S.P. Vyas, *Non-ionic surfactant based vesicles (niosomes) in drug delivery.* International Journal of pharmaceutics, 1998. **172**(1): p. 33-70.

30. Yoshioka, T., B. Sternberg, and A.T. Florence, *Preparation and properties of vesicles (niosomes) of sorbitan monoesters (Span 20, 40, 60 and 80) and a sorbitan triester (Span 85).* International journal of pharmaceutics, 1994. **105**(1): p. 1-6.

31. Bayindir, Z.S. and N. Yuksel, *Characterization of niosomes prepared with various nonionic surfactants for paclitaxel oral delivery.* Journal of pharmaceutical sciences, 2010. **99**(4): p. 2049-2060.

32. Serra, L., J. Doménech, and N.A. Peppas, *Drug transport mechanisms and release kinetics from molecularly designed poly (acrylic acid-g-ethylene glycol) hydrogels.* Biomaterials, 2006. **27**(31): p. 5440-5451.

33. Siepmann, J. and N. Peppas, *Modeling of drug release from delivery systems based on hydroxypropyl methylcellulose (HPMC).* Advanced drug delivery reviews, 2012. **64**: p. 163-174.

34. Balakrishnan, P., et al., *Formulation and in vitro assessment of minoxidil niosomes for enhanced skin delivery.* International journal of pharmaceutics, 2009. **377**(1): p. 1-8.

35. Sezgin-Bayindir, Z. and N. Yuksel, *Investigation of formulation variables and excipient* interaction *on the production of niosomes.* AAPS PharmSciTech, 2012. **13**(3): p. 826-835.

36. Park, S.N., et al., Preparation *of quercetin and rutin-loaded ceramide liposomes and drug-releasing effect in liposome-in-hydrogel complex system.* Biochemical and biophysical research communications, 2013. **435**(3): p. 361-366.

37. Berger, J., et al., *Structure and interactions in covalently and ionically crosslinked chitosan hydrogels for biomedical applications.* European Journal of Pharmaceutics and Biopharmaceutics, 2004. **57**(1): p. 19-34.

38. Vårum, K.M., et al., *In vitro degradation rates of partially N-acetylated chitosans in human serum. Carbohydrate* research, 1997. **299**(1): p. 99-101.

39. Ganji, F., M. Abdekhodaie, and A.R. SA, *Gelation time and degradation rate of chitosan-based injectable hydrogel.* Journal of sol-gel science and technology, 2007. **42**(1): p. 47-53.

40. Pangburn, S., P. Trescony, and J. Heller, *Lysozyme degradation of partially deacetylated chitin, its films and hydrogels.* Biomaterials, 1982. **3**(2): p. 105-108.

CHAPTER 4[1]: A CELL ELISA FOR THE QUANTIFICATION OF MUC1 MUCIN EXPRESSED BY CANCER CELLS OF EPITHELIAL AND NEUROECTODERMAL ORIGIN

4.1. Abstract

Quantitative analysis of MUC1, a cell membrane associated mucin, expressed by intact cells of epithelial origin previously has been limited to flow cytometry, which requires using large quantities of cells and antibodies. Here, for the first time, we report the development of a novel Cellular-based Enzyme Linked Immunosorbent Assay (Cell ELISA) to quantify the expression of MUC1 by cell lines of epithelial and neuroectodermal origin using an antibody recognizing a specific tandem repeat found in the extracellular domain of MUC1. In contrast to flow cytometry, this method requires a much lower number of cells. We report here the results obtained from two variants of this Cell ELISA in live and fixed cells. We found that the Cell ELISA in live cells was not sensitive enough to detect a difference in MUC1 levels between the normal cells and tumor cells. However, we found that Cell ELISA in fixed cells followed by whole cell staining was a dependable method of MUC1 level detection in the normal and tumor cells showing significantly higher levels of MUC1 receptor in the tumor cells when compared to the normal controls. Therefore, we conclude that the Cell ELISA in fixed cells is an efficient

[1] Note. "A CELL ELISA FOR THE QUANTIFICATION OF MUC1 MUCIN (CD227) EXPRESSED BY CANCER CELLS OF EPITHELIAL AND NEUROECTODERMAL ORIGIN" Falahat, Rana, et al., 2015, Cellular Immunology, Vol. 298, No. 1, Copyright © 2016 by Elsevier Inc. Permission is included in Appendix A.

method for quantifying the expression of MUC1 by epithelial and neuroectodermal cancer cell lines.

4.2. Introduction

MUC1 mucin (CD227), a large glycoprotein, is expressed on the surface of normal glandular epithelial cells and has been found to be aberrantly overexpressed on most carcinoma cells [1, 2]. In addition to being an important and valuable diagnostic tumor marker, MUC1 has been studied as a potential therapeutic target [3, 4]. Recent advances in MUC1 associated cancer therapies, including immunotherapy [5, 6] and targeted drug delivery [7-9], have created a need for quantitative assessment of MUC1 in various tumor cells. Until now, the expression of MUC1 on the surface of intact cells has been quantified using flow cytometry [10-12], which, despite its sensitivity to detect cell surface antigens, requires a large number of cells [13, 14]. Cell ELISA, as described here, is based on the interaction between antibodies and cell surface antigens assisted by colorimetric (or near infrared) methods of antigen detection. It has been shown to be as sensitive as flow cytometry, and it is a commonly used method for quantification of surface antigens [15-17]. The aim of this study was to develop a Cell ELISA technique to quantify the expression level of MUC1 in various tumor cells and compare it to the normal controls. Our study included the design of two variants of Cell ELISA using live cells and fixed cells. Flow cytometry and Western blot were used to validate the developed Cell ELISA assays.

4.3. Materials and Methods

4.3.1. Cell Lines

The following cell lines were used: human ovarian epithelial origin carcinoma OV2008, SV-40 large T-antigen transfected normal human ovarian surface epithelial cells IMCC3 (both provided by Dr. Patricia Kruk, Department of Pathology and Cell Biology, College of Medicine,

University of South Florida, Tampa, FL), two human glioblastoma astrocytoma cell lines U87 and U373 (both from American Type Culture Collection) and mouse glioma G26 [18, 19]. The ovarian cell lines (OV2008 and IMCC3) were cultured in a 1:1 mixture of MCDB105/M199 medium (Sigma-Aldrich, MO) supplemented with 5% fetal bovine serum (FBS; Hyclone, UT) and 10 μg/ml Gentamicin. The G26, U87, and U373 cell lines were grown in Minimum Essential Medium with Earle's Balanced Salts (MEM/EBSS; Hyclone, UT) supplemented with 10% FBS and 2 mM L-glutamine, penicillin, and streptomycin. All cell lines were grown in 25 cm^2 culture flasks (Corning, NY) and incubated at 37ºC with 5% CO_2.

4.3.2. Antibodies

VU-11D1, a mouse primary (Ab1) monoclonal antibody recognizing TSAPDTR, the 7-mer epitope found in the extracellular domain of MUC1 protein, HRP-conjugated polyclonal goat anti-mouse secondary IgG antibody (Ab2) (both from NOVUS Biologicals, CO), goat anti-mouse IgG-PE (Santa Cruz Biotechnology, CA), and anti-α-Tubulin monoclonal antibody (T6199) (Sigma-Aldrich, MO) were used in this study.

4.3.3. Cell ELISA using Live Cells

The first assay, Cell ELISA using live cells, was performed as follows. After detaching cells from the culture flask and adjusting the cell density to 3×10^5 cells/ml, 100 μl of the cell suspension (3×10^4 cells/well) was added to each well of a flat-bottomed 96-well microtiter plate (Corning, NY). The plate was incubated overnight with an appropriate growth medium at 37ºC in 5% CO_2. The following day, the medium was removed, and the confluent cell monolayers were washed 3 times with 200 μl/well of washing buffer (0.01 M Phosphate Buffered Saline (PBS) containing 0.5% (w/v) Bovine Serum Albumin (BSA) (Sigma-Aldrich, MO)). Nonspecific binding was blocked using 100 μl/well of blocking solution containing 2% (v/v) normal goat

serum (Southern Biotech, AL) and 1% (w/v) BSA in 0.01 M PBS for 1 hour at 4ºC. The cells were treated under one of the following experimental conditions: 1) primary antibody alone (Control Ab1); 2) secondary antibody alone (Control Ab2); 3) primary and secondary antibody together (Ab1 + Ab2); or 4) blocking solution alone (Cell Control). Both primary and secondary antibodies were prepared in the blocking solution. Upon the removal of the blocking solution cells received either 50 µl/well of the primary antibody or 50 µl/well of the blocking solution followed by incubation for at least 1 hour at 4ºC. The plate was washed 5 times with 200 µl/well of the washing buffer and then exposed to 50 µl/well of the secondary antibody or 50 µl/well of the blocking solution and incubated for additional 1 hour at 4 ºC. The plate was washed 5 times with 200 µl/well of the washing buffer. Then, 100 µl of TMB (3,3', 5,5"-tetramethylbenzidine) substrate solution (Cell Signaling Technology, MA) was added to each well, and the reaction was allowed to proceed for 20 minuets at room temperature. The enzyme reaction was stopped by the addition of 25 µl/well of 2 M sulfuric acid. The optical density (OD) at 450 nm was measured using an ELx800 microplate reader (Bio-Tek Instruments, VT).

4.3.4. Cell ELISA using Fixed Cells

In this variant of Cell ELISA, a fixation step was used to prevent loss of cells during the procedure. This assay is analogous to Cell ELISA in live cells and the same experimental treatment groups (Control Ab1, Control Ab2, Ab1+Ab2, and Cell Control) were used as described in section 4.3.3. Briefly, cells were seeded in a flat-bottomed 96-well microtiter plate at 3×10^4 cells/well in the appropriate growth medium. Following the incubation for 24 hours at 37ºC in 5% CO_2, the growth medium was removed and the confluent cell monolayers were washed 3 times with 0.01 M PBS (200 µl/well) and fixed with 4% (v/v) paraformaldehyde (Electron Microscopy Sciences, PA) in 0.01 M PBS (100 µl/well) for 10 minutes at room

temperature. The fixed monolayers were washed 3 times with 0.01 M PBS (200 µl/well) and then permeabilized with 50 µl/well of the blocking solution (0.01 M PBS containing 2% (v/v) normal goat serum, 1% (w/v) BSA, and 0.1% (v/v) Triton X-100) for 1 hour at room temperature. Upon the removal of the blocking solution cells received 50 µl/well of the primary antibody or 50 µl/well of the blocking solution and were incubated for at least 1 hour at room temperature. The plate was washed 3 times with 0.01 M PBS (5 minutes each) and then exposed to 50 µl/well of the secondary antibody or 50 µl/well of the blocking solution and incubated for 1 hour at room temperature. After washing with 0.01 M PBS (3 times, 5 minutes each), the plate was incubated with the TMB substrate solution (100 µl/well) at room temperature. The reaction was allowed to proceed for 20 minuets. The enzyme reaction was stopped by adding 25 µl/well of the stop solution, followed by reading the OD at 450 nm using a microplate reader.

4.3.5. Quantification of the Cell Number in Cell ELISA using Fixed Cells

After removing the plate contents, 50 µL/well of 1X Janus Green stain (Abcam, MA) was added to the plate and incubated for 5 minutes at room temperature. Next, the plate was washed 5 times with 200 µl/well of deionized water followed by the addition of 50 µL/well of 0.5 M HCl. The OD at 595nm was measured using the ELx800 microplate reader. The results were analyzed by normalizing OD values measured at 450 nm to cell number ($[OD_{450}]$ / $[OD_{595}]$) to account for differences in cell numbers in various wells. All washing and incubation steps (except for the overnight incubation) were performed on a plate shaker (Bellco Biotechnology, NJ) with gentle shaking at 300 rpm.

4.3.6. Flow Cytometry

Flow cytometry analysis was performed on OV2008 cells as follows: cells were trypsinized from adherent cultures and resuspended in the blocking solution (0.01 M PBS

containing 2% (v/v) normal goat serum and 1% (w/v) BSA). After adjusting the cell density to 5×10^6 cells/ml, 100 µl of the cell suspension (5×10^5 cells) was added to micro-centrifuge tubes and incubated for 1 hour at 4ºC. The same experimental treatment groups (Control Ab1, Control Ab2, Ab1+Ab2, and Cell Control) were used for flow cytometry as described in section 4.3.3.

Upon the removal of the blocking solution cells received either 100 µl of the primary antibody or 100 µl of the blocking solution followed by incubation for at least 1 hour at 4ºC. The samples were washed 3 times with the washing buffer (0.01 M PBS containing 1% (w/v) BSA) by centrifugation at 400 g for 5 minutes and then exposed to 100 µl of the goat anti-mouse IgG-PE secondary antibody or 100 µl of the blocking solution and incubated for 30 minutes at 4ºC in the dark. After washing (3 times, 5 minutes each), the samples were re-suspended in 0.01 M PBS and stained with 7-Aminoactinomycin D (7-AAD) viability dye (BD Pharmingen, CA) for 15 minutes to distinguish live cells (7-AAD negative) from dead cells (7-AAD positive).

Flow cytometry was performed on aliquots of each sample using an Accuri C6 flow cytometer (BD Biosciences, CA) and obtained data was analyzed using CFlow Plus software (BD Biosciences, CA). A minimum of 50,000 events was collected on each sample. Staining intensity was determined in 2-dimensional histograms of fluorescence intensity versus cell number. After gating the 7-AAD-negative cell population, the percentage of live cells expressing PE was determined.

4.3.7. Western Blot

Cells were grown to 70% confluence and washed with ice-cold 0.01 M PBS and detached using scrapping. Cells were pelleted and suspended in 2× RIPA buffer (50 mM Tris-buffered saline [TBS], pH 8.0, 150 mM NaCl, 1% NP-40, 0.5% sodium deoxycholate, 0.1% sodium dodecyl sulfate [SDS]) supplemented with Halt Protease inhibitors (Thermo Fisher Scientific,

MA). The cell lysate was sonicated for 5 seconds at 30% Amplitude and quantified using a standard Coomassie protein assay (Pierce Biotechnology, IL). The lysate was denatured in 4% SDS sample buffer with 10% (v/v) 2-mercaptoethanol, then incubated for 5 minutes at 95˚C. The amount of 50 µg of the lysate was electrophoresed though a 10% Protean-TGX gel (BioRad, CA) and transferred to nitrocellulose overnight in a buffer containing 0.1% SDS and 10% methanol. The membrane was incubated in blocking buffer (5% (w/v) milk in 50 mM TBS with 0.1% Tween-20 [TBST]), followed by overnight incubation in 1µg/ml Anti-MUC1 (VU-11D1) antibody in TBST with 5% (w/v) BSA. The membrane was washed 3 times for a total of 15 minutes in TBST and then incubated for 1 hour in HRP conjugated secondary antibody. Washes were repeated and the bands visualized by soaking the membrane for 3 minutes in SuperSignal West Femto Luminol substrate (Thermo Fisher Scientific, MA) followed by standard autoradiography. To ensure equal loading, the membrane was stripped by incubating with agitation for 1 hour at 50˚C in stripping buffer containing 2% SDS, 0.1 M Tris HCl (pH 6.8) and 1% (v/v) 2-mercaproethanol. The membrane was washed for 1 hour with continuous fresh deionized water and incubated for 1 hour in the blocking buffer. Anti-α-Tubulin monoclonal antibody (T6199) (Sigma-Aldrich, MO) was diluted 1:1000 in the fresh blocking buffer and incubated for 1 hour. Washings, secondary antibody incubation, and luminol detection were then completed as mentioned above. The total intensity of MUC1 bands was quantified by densitometry using ImageJ software (NIH, MD) and normalized by the intensity of the α-Tubulin band for each cell line.

4.3.8. Statistical Analysis

Statistical analysis was carried out using the Microsoft Excel Analysis Tool Pack (Redmond, WA). Descriptive statistical parameters (mean and SD) were calculated for the

measured OD values. The Student's t-test was used to assess the statistical significance of the difference between the cells with antibody treatments (Ab1+Ab2) and the cells in the presence of the secondary antibody (Control Ab2).

The OD levels of Cell Control and Control Ab1 were at the baseline in all experiments; therefore, they were not further considered. A p-value < 0.05 was considered to be statistically significant. A total of n=12 experiments for Cell ELISA in live cells and n=10 experiments for Cell ELISA in fixed cells were evaluated. All the experiments were done in triplicate. The statistical analysis using the data derived from Cell ELISA with fixed cells followed by whole cell staining was performed using n=4 experiments for OV2008, n=3 experiments for IMCC3, and n= 1 experiment for G26, U87, and U373 cell lines. All the experiments included triplicate measurements.

The results for Cell ELISA in fixed cells were further analyzed to account for differences in cell numbers in various wells in which the OD measured at 450 nm was divided by the OD measured at 595 nm representing cell numbers ($[OD_{450}] / [OD_{595}]$).

4.4. Results

4.4.1. Optimal Experimental Conditions for Cell ELISA Assay

4.4.1.1. Cell Density

The optimal cell seeding density was determined using 0.3×10^4 to 10×10^4 cells/well of OV2008 cells in Cell ELISA assay using fixed cells (Figure 4.1). The OD value obtained for the secondary antibody (Control Ab2) was subtracted from the OD value obtained for Ab1 +Ab2 to account for the nonspecific binding ($[OD_{450}]_{Ab1+Ab2} - [OD_{450}]_{Control\ Ab2}$). A cell density of 3×10^4 cells/well was selected as the optimum cell concentration as the higher cell densities resulted in similar responses.

4.4.1.2. Antibody Concentrations

To determine the binding activity of the primary antibody, various dilutions of VU-11D1 were used to treat OV2008 cells in Cell ELISA assay using live and fixed cells. The assay was performed with 1 μg/ml concentration of the secondary antibody. The OD level of the secondary antibody (Control Ab2) was subtracted from the OD level of Ab1 +Ab2. The dose response curve of the primary antibody (Figure 4.2) indicates concentration-dependent responses in Cell ELISA assay using fixed cells. The optimal concentration of the primary antibody was found to be 1 μg/ml (1:100 dilution).

A similar study using various concentrations (0.005 to 5 μg/ml) of the secondary antibody with1 μg/ml concentration of the primary antibody was performed (data not shown). The concentration of 1 μg/ml (1:500 dilution) for the secondary antibody was selected as the optimum concentration for the next experiments.

4.4.1.3. Temperature

To determine the effect of temperature during cell incubation on the efficiency of antibody binding measured as OD, Cell ELISA assay using live OV2008 cells was performed at 4ºC and 37ºC incubation temperatures. As seen in Figure 4.3, the OD values were not significantly different ($p>0.05$) when evaluating OV2008 cells incubated at 4ºC and 37ºC. In addition to 1-hour incubation, OV2008 cells were incubated for 2 hours at either 4ºC or 37ºC (data not shown). The results obtained for this time point also indicated no difference in antibody binding efficiency for cell incubation at 4ºC and 37ºC.

Also, to investigate the possible effect of temperature on the IMCC3 cell loss in Cell ELISA assay using live cells, a similar study was performed. It was found that the incubation at both 37ºC and 4ºC resulted in the similar loss of IMCC3 cells. This indicates that the IMCC3

cell loss in the Cell ELISA assay using live cells occurred independently from the incubation temperature.

4.4.2. Cell ELISA using Live Cells

Cell ELISA assay using live cells was performed using four cell lines: OV2008, IMCC3, G26, and U87. The cells were seeded at a density of 3×10^4 cells/well. The primary and secondary antibodies were used at the optimal concentrations obtained in section 4.4.1.2.

Figure 4.4 shows the OD values for the tested cell lines in Cell ELISA assay using live cells indicating MUC1 expression. The response in the Control Ab2 relates to the intrinsic enzyme activity or nonspecific binding of HRP conjugated secondary antibody to the cell lines. The OV2008 cells showed 64% more response in Ab1+Ab2 than Control Ab2 $[([OD_{450}]_{Ab1+Ab2} - [OD_{450}]_{Control\ Ab2})/ [OD_{450}]_{Control\ Ab2} \times 100]$ ($p<0.05$). Similarly, the G26 cells had 56% more response in Ab1+ Ab2 as compared to Control Ab2 ($p<0.05$). There was no significant difference between the OD values for Ab1+Ab2 and Control Ab2 ($p>0.05$) when IMCC3 and U87 cells were evaluated. Therefore, we concluded that although MUC1 expression was detected in OV2008 and G26 cell lines using this method, MUC1 expression was not detectable in IMCC3 and U87 cell lines. A relatively high cell loss was observed using a light microscope during the incubation and washing steps for all the cell lines except for OV2008.

4.4.3. Cell ELISA using Fixed Cells

In an attempt to improve the preservation of cells and minimize cell loss during the numerous washing steps, a fixation step with paraformaldehyde was applied in this variant of Cell ELISA. A fixation step is considered to be an effective way to inactivate endogenous peroxidase activity and, subsequently, to minimize the enzyme background problem that is common in eukaryotic cells [14, 20]. Also, to account for the differences in the cell densities and

have comparable results, whole-cell staining with Janus Green was used in this Cell ELISA method, in which the OD values measured at 490 nm were normalized to the Janus Green staining intensity measured at 595 nm ($[OD_{450}]$ / $[OD_{595}]$). In addition to the cell lines used in Cell ELISA assay using live cells, a U373 human glioma cell line was used in this assay.

Figure 4.5 shows the OD (normalized to cell number) for various cell lines in Cell ELISA assay using fixed cells. These data show that fixation with paraformaldehyde did not affect the integrity of MUC1 in this assay. The OD indicating expression of MUC1 by OV2008 was 167% higher in Ab1+Ab2 treated cells than the Control Ab2 ($p<0.05$). This difference was 83% and 101% for IMCC3 and G26 cell lines, respectively. Unlike Cell ELISA assay using live cells, the difference between the OD in Ab1+Ab2 and Control Ab2 for IMCC3 cells in this method was statistically significant ($p<0.05$). The U87 and U373 human glioma cell lines did not show significant difference ($p>0.05$) between the OD measured for Ab1+Ab2 and Control Ab2 indicating that MUC1 expression in these cell lines cannot be evaluated using this technique. Therefore, it was concluded that the MUC1 receptor was detected consistently in the two tumor cells lines OV2008 and G26. In addition, using this method, MUC1 also was detected in normal ovarian epithelial cell control IMCC3. However, two human glioma cell lines U87 and U373 showed no detectable levels of MUC1. When the levels of MUC1 in epithelial ovarian carcinoma OV2008 was compared to the MUC1 levels in the normal ovarian epithelial control IMCC3, a statistically significant difference between these two cell lines was found (Figure 4.6). In addition, Figure 4.6 shows a comparison between these two types of Cell ELISA assays, using live and fixed OV2008 and IMCC3 cells. When the OD value at 450 nm obtained for Control Ab2 was subtracted from the OD value obtained for Ab1 +Ab2 ($[OD_{450}]_{Ab1+Ab2}$ - $[OD_{450}]_{Control\ Ab2}$, the difference in the expression level of MUC1 between OV2008 and IMCC3 cell lines was

found to be statistically significant ($p<0.05$) in Cell ELISA using fixed cells, but not in Cell ELISA using live cells.

4.4.4. Flow Cytometry

To validate the developed Cell ELISA assays, flow cytometry analysis was performed on OV2008 cells. Analysis of the data obtained from flow cytometry using CFlow Plus software showed the expression of MUC1 in OV2008 cells (Figure 4.7). From the representative data, 42.9% of the cells treated with anti-MUC1 primary antibody and PE-conjugated secondary antibody (Ab1+Ab2) and 7.87% of the cells treated with PE-conjugated secondary antibody (Control Ab2 PE) were identified as PE-positive, indicating 35% of the OV2008 cells as MUC1-positive in this experiment and with a similar range of 30% to 45% of MUC1-positive cells in all four experiments.

4.4.5. Western Blot

Western blot analysis was performed to determine the relative amount of MUC1 protein in OV2008 and U87 cell lines and to further validate experiments using Cell ELISA. The Cell ELISA demonstrated an attenuated expression of MUC1 in U87 and an increased level of MUC1 expression in OV2008 cells. Therefore, whole cell lysates were created in an SDS buffer using OV2008 and U87 cell lines to provide positive and negative controls, respectively.

Figure 4.8A shows equal loading of total cell lysate in both gel lanes (OV2008 and U87) as seen by immunoblotting using anti-α-Tubulin antibody. MUC1 staining resulted in multiple bands ranging in size from approximately 30 to 65 kDa. The most prominent band resolved at approximately 55 kDa in OV2008 cells but not U87. An intense band around 60 kDa was observed in both cell lines. Densitometry analysis of Western blot bands revealed more than a

twofold higher expression level of MUC1 (normalized to α-Tubulin) in OV2008 when compared to U87 (Figure 4.8B).

4.5. Discussion

Two variants of Cell ELISA using live and fixed cells are described in this study. Initially, Cell ELISA assay using live cells was performed due to the previously-reported concerns about alteration and/or loss of integrity of cell bound antigens when using fixation [14, 21]. Normal goat serum was used in the blocking agent to block any non-specific binding of goat anti-mouse IgG secondary antibody. As one of the most effective blocking methods, using normal serum from the same host species as the labeled secondary antibody prevents non-specific binding of the labeled IgG antibody. In an effort to optimize the assay, various concentrations of the antibodies were examined in the preliminary experiments for OV2008 cells, and the optimal concentrations of primary and secondary antibody were determined. A significant loss of cell monolayer was observed in Cell ELISA assay using live cells for all the cell lines (except OV2008), in spite of following a gentle washing protocol [20]. The detachment of cells (except OV2008) during the washing steps in this assay resulted in large variations in the number of recovered cells. The expression of MUC1 was detected only for the OV2008 and G26 cell lines in Cell ELISA assay using live cells (as seen in Figure 4.4 and summarized in Table 4.1). Cell ELISA for live cells could not be used for IMCC3 because of the high cell loss.

Therefore, a fixation step was added to both improve cell preservation and to reduce the background due to endogenous peroxidase activity [14, 20]. The use of a fixation step helped to retain a cell monolayer which was confirmed by using whole cell staining with Janus Green at end of the assay. Also, visual inspection of the cell monolayer under the light microscope supported that a cell monolayer was retained using fixation.

Using fixed cells, a significantly higher expression level of MUC1 was detected for the OV2008 cell line when compared to IMCC3 normal control. The results obtained for OV2008 (human ovarian carcinoma cell line) are consistent with the well-documented overexpression of MUC1 in almost all human adenocarcinomas (including 90% of breast, ovarian, pancreatic, colorectal, lung, prostate, and gastric carcinomas) [22-25].

In contrast to Cell ELISA assay with live cells, IMCC3 cells showed MUC1 expression in Cell ELISA assay with fixed cells, due to the sufficient cell numbers available for evaluation and possibly due to the reduced endogenous peroxidase activity.

Although being known as an epithelial-specific antigen, variable levels of MUC1 have been reported to be expressed by many other cancer cells, including astrocytoma, melanoma, and neuroblastoma as well as hematologic malignancies (multiple myeloma and some B-cell non-Hodgkin lymphomas) [12, 26, 27]. The data obtained in this study regarding the relatively low level of MUC1 expression by normal epithelial ovarian cells lines, e.g., IMCC3, when compared to the MUC1 levels expression by ovarian carcinoma of epithelial origin e.g., OV2008, support previously-reported findings by other investigators [23, 28, 29] who used other methodologies for MUC1 detection. This also confirms the reliability of the Cell ELISA assay described here as a method of choice for the detection of MUC1 expression by normal and tumorous epithelial cell lines.

To further compare findings regarding MUC1 expression using the Cell ELISA method developed in this study to findings of other investigators using different methodologies, we included additional cell lines such as U87 human glioma cell line reported previously to have no detectable levels of MUC1 [30, 31]. Again, we were able to confirm those previous findings, and the U87 human glioma cell line served in our studies as a negative control.

In addition, we included another human glioma cell line, U373, which has comparable characteristics to the U87 human glioma cell line by not exhibiting the typical and expected migratory capacity *in vivo* when implanted intracerebrally, resulting in extended survival times [32]. Again, our data regarding MUC1 expression were the same for the U373 human glioma cell line as for the U87 glioma, suggesting a possible connection between MUC1 expression and invasiveness of tumor cell lines. Our Cell ELISA assay consistently showed that MUC1 level was not detectable on these two cell lines providing an additional negative control.

However, to further test this possible connection between the expression of MUC1 and the migratory and invasive characteristics of tumor cell lines, we included the G26 glioma cell line, which was shown in our previous study to be highly invasive *in vitro* and *in vivo* in the orthotopic intracerebral mouse model and expressing markers found in immature progenitor cells, which were not found in U87 and U373 glioma [33]. The data from this study showed that this highly invasive and migratory G26 glioma cell line expressed MUC1. In light of this finding, MUC1 could be considered as another marker of tumor cell invasiveness, but this is a focus of a separate and currently ongoing study in our laboratory.

We concluded that fixation of cells (with paraformaldehyde) in the Cell ELISA technique is essential to obtain reliable data. We found that fixation did not interfere with MUC1-antibody binding. This finding is consistent with the previous MUC1 quantification studies using flow cytometry where a fixation step had been applied [10-12]. In addition, the implementation of whole-cell staining with Janus Green in Cell ELISA assay using fixed cells improved the accuracy of the assay by allowing for a normalization of the OD data based on cell numbers.

To validate the developed Cell ELISA assay as an effective method for quantification of MUC1, flow cytometry was performed on OV2008 cells. The percentage of MUC1-positive cells determined by flow cytometry correlated with the Cell ELISA results.

The results of the Cell ELISA assay were validated additionally by Western blotting of OV2008 and U87 cell lines. Multiple bands ranging in size from approximately 30 to 65 kDa were observed for MUC1 staining. Previous studies with Western blotting of MUC1 have clearly demonstrated cleavage of the α- and β-subunits of MUC1 using SDS [34]. The anti-MUC1 antibody (VU-11D1) was raised against the epitope TSAPDTR, which is found within the variable number tandem repeat (VNTR) region on the extracellular side of the protein [35]. Therefore, the antibody was raised to detect the extracellular side of the protein. Additionally, the extracellular domain of MUC1 can vary significantly in length among different cell lines due to the VNTR domain existing between 20 to 125 repeats among different individuals [36]. Densitometry demonstrated a greater than two-fold increase in MUC1 expression in OV2008 as compared to U87, and this correlates with the results obtained by Cell ELISA. Both flow cytometry and Western blotting analyses correlated well with the Cell ELISA data, thus providing validation for the results.

This Cell ELISA assay offers the convenience of testing various samples in multiple replicates on a single 96-well plate at once while using a small number of cells and reagents and inexpensive equipment.

The overexpression of MUC1 in certain cancer cells makes it an attractive therapeutic target for the design of a drug delivery system based on chitosan, which has been shown to have a strong mucoadhesive property [1, 37]. Having a sensitive and reproducible assay to detect the

expression of MUC1 in various cancer cells is essential for the further development of a previously-published drug delivery system with chitosan hydrogel [38, 39].

In summary, the newly-established Cell ELISA technique using fixed cells described in this paper can be used as a simple method to quantify the expression of MUC1 antigen on the surface of cells of epithelial and neuroectodermal origin in comparison to the normal controls.

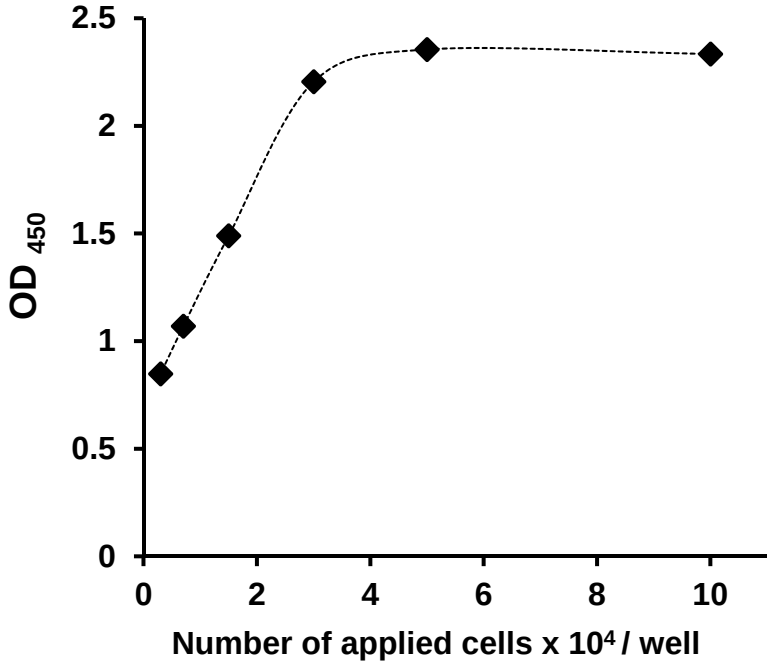

Figure 4.1 Effect of cell seeding density on the efficiency of antibody binding for OV2008 cells in Cell ELISA using fixed cells. The OD level obtained for the secondary antibody (Control Ab2) was subtracted from the OD level obtained for Ab1 +Ab2. The data represent the mean of duplicate samples.

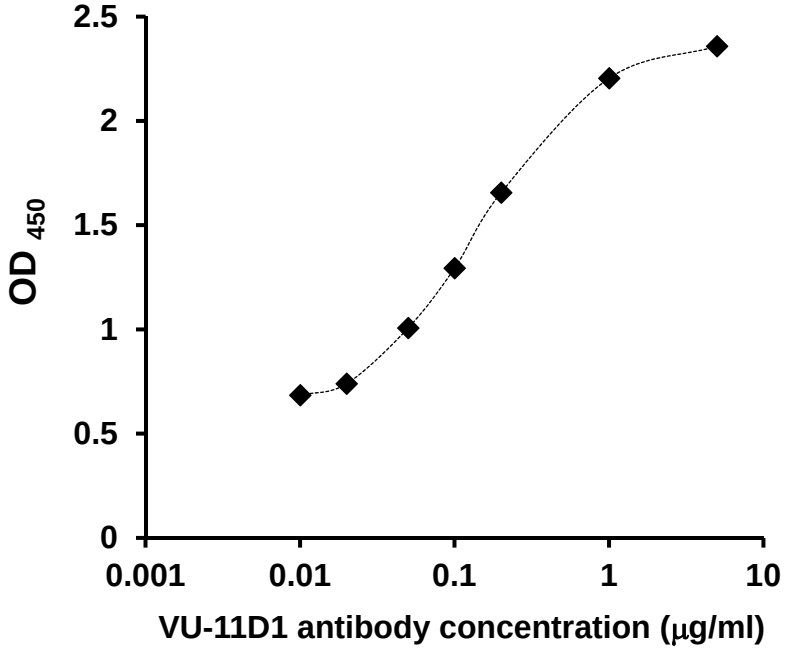

Figure 4.2 Titration of VU-11D1 antibody, OV2008 cells were used at the density of 3×10^4 cells/well in Cell ELISA using fixed cells. The OD level obtained for the secondary antibody (Control Ab2) was subtracted from the OD level obtained for Ab1 +Ab2. The data represent the mean of duplicate samples.

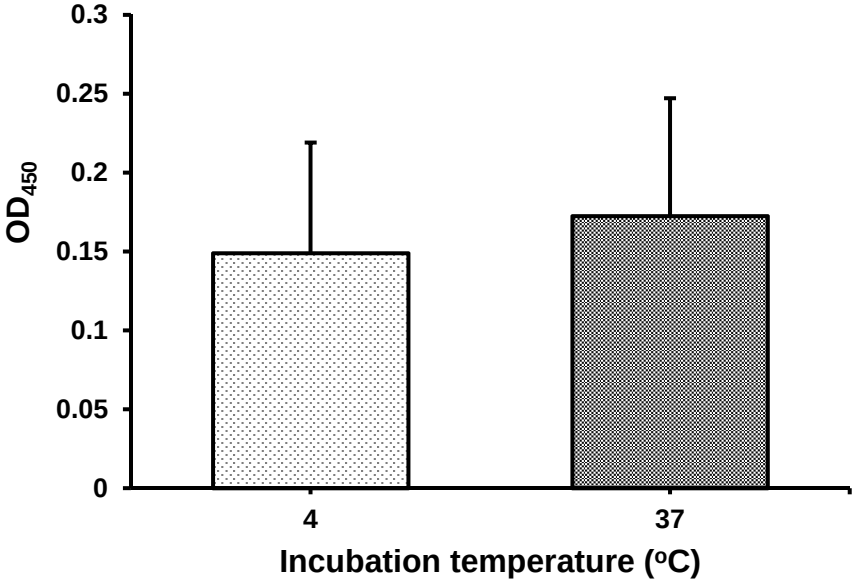

Figure 4.3 Effect of incubation temperature on the efficiency of antibody binding for OV2008 cells in Cell ELISA using live cells. The OD level obtained for the secondary antibody (Control Ab2) was subtracted from the OD level obtained for Ab1 +Ab2. The temperature had no statistically significant effect on the antibody binding efficiency measured as OD. The data represent n=2 experiments with triplicate samples.

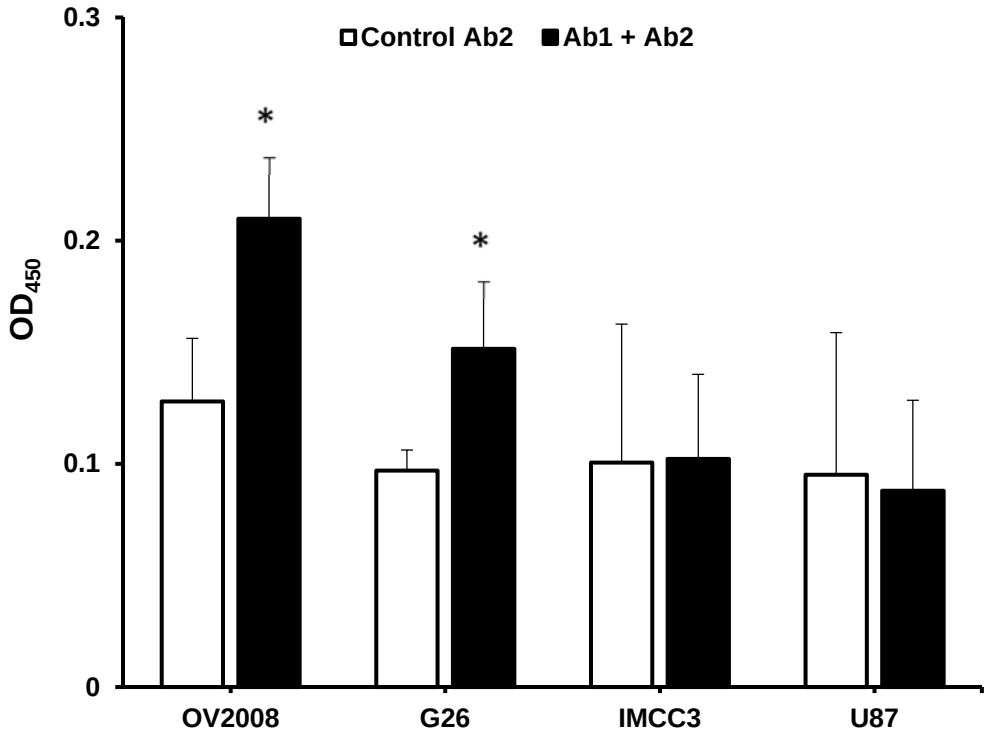

Figure 4.4 Cell ELISA assay using live OV2008, IMCC3, G26 and U87 cell lines. The data represent the mean of OD values for n=3 experiments with triplicate samples for OV2008 and IMCC3 cells and n=1 experiment for G26 and U87 cells with triplicate samples. The statistical significance between Ab1+Ab2 and Control Ab2 was analyzed using Student's t-test: *, $p<0.05$.

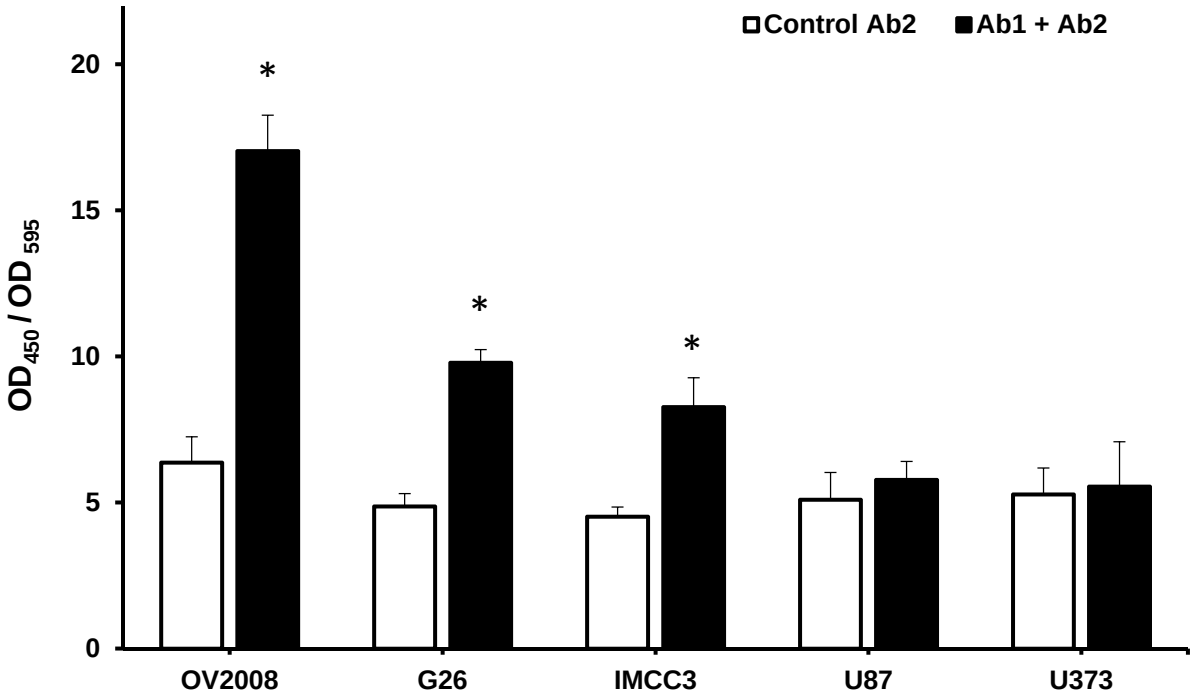

Figure 4.5 Cell ELISA using fixed cells (normalized by cell number) for OV2008, IMCC3, G26, U87, and U373 cell lines. The data represent the mean of OD values for n=4 experiments for OV2008, n=3 experiments for IMCC3, and n=1 experiment for G26, U87, and U373 cell lines all with triplicate samples. The statistical significance between Ab1+Ab2 and Control Ab2 was analyzed using Student's t-test: *, $p<0.05$.

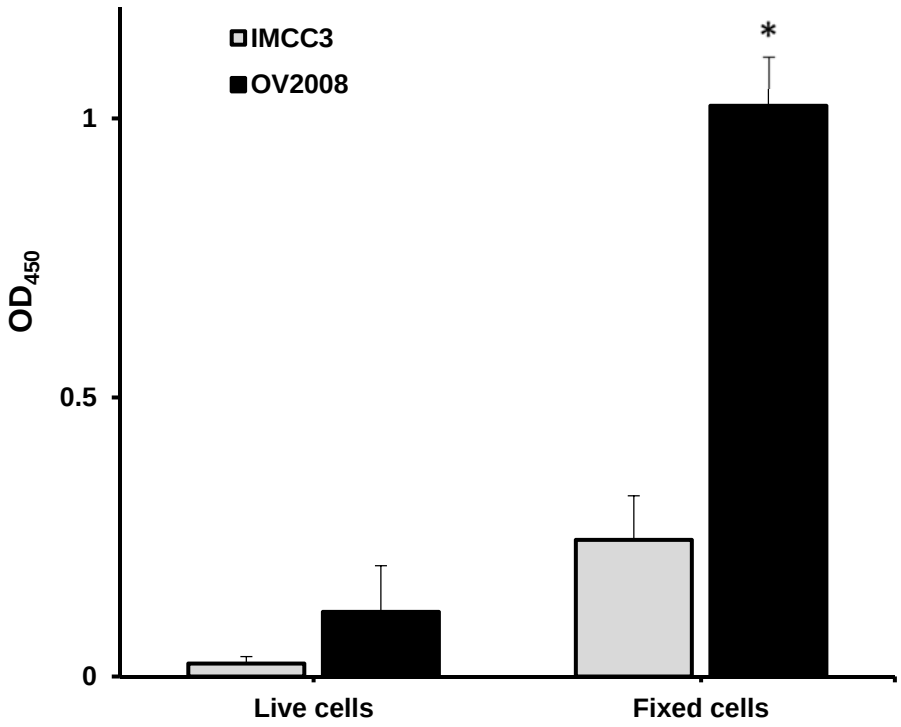

Figure 4.6 Cell ELISA using fixed and live OV2008 and IMCC3 cells. The OD value at 450 nm obtained for Control Ab2 was subtracted from the OD value at 450 nm obtained for Ab1 +Ab2. The data represent n=3 experiments for live IMCC3 and OV2008 cells, n=3 experiments for fixed IMCC3 cells, and n=4 experiments for fixed OV2008 cells all with triplicate samples. The statistical significance between IMCC3 and OV2008 cell lines was analyzed using Student's t-test: *, $p<0.05$.

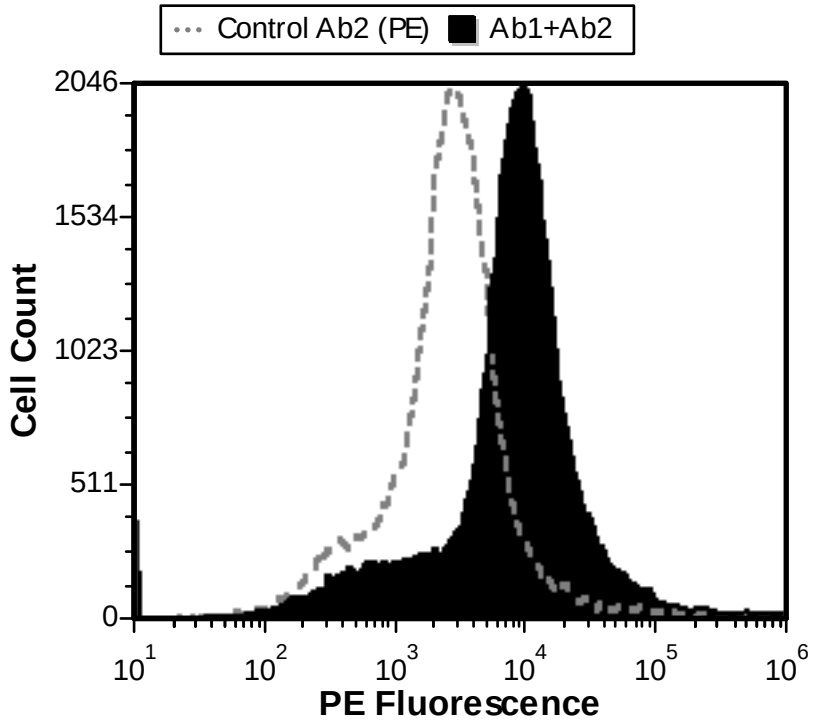

Figure 4.7 Flow cytometric evaluation of MUC1 expression in OV2008 cells. The superimposed peaks in the histogram represent Ab1+Ab2 (cells treated with anti-MUC1 antibody and PE conjugated secondary antibody) (filled black) and Control Ab2 PE (cells treated with PE conjugated secondary antibody) (dashed gray line). The histogram is a representative of four independent experiments.

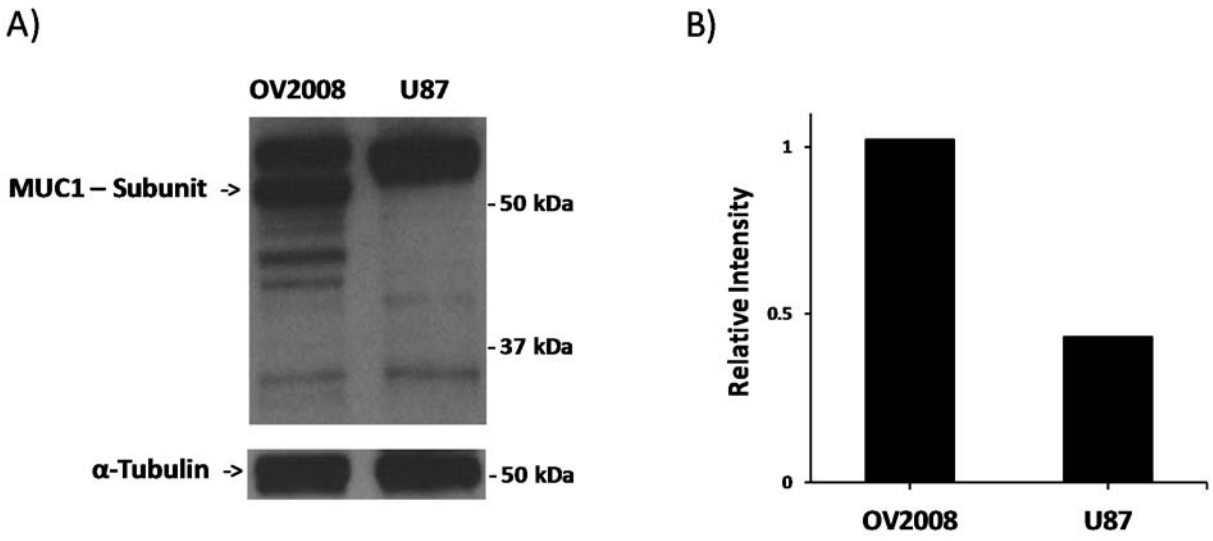

Figure 4.8 Evaluation of MUC1 expression in OV2008 and U87 cell lines using Western blot. A) Cell lysates were harvested and used at 50 μg. α-Tubulin was used as a sample loading control. B) Quantification of the MUC1 expression was performed with densitometric analysis by ImageJ software and normalized to α-Tubulin.

Table 4.1 Summary data for Cell ELISA in live cells and Cell ELISA in fixed cells

Cell line	Cell ELISA in live cells[a]	Cell ELISA in fixed cells[b]
OV2008	64%	167%
IMCC3	NS	83%
G26	56%	101%
U87	NS	NS
U373	ND	NS

NS = No significant difference between Ab1+Ab2 and Control Ab2 was found.
ND = Not determined.

a $\frac{[\mathbf{OD_{450}}]_{\mathbf{Ab1+Ab2}} - [\mathbf{OD_{450}}]_{\mathbf{Control\ Ab2}}}{[\mathbf{OD_{450}}]_{\mathbf{Control\ Ab2}}} \times \mathbf{100}$

b $\frac{[\mathbf{OD_{450}/OD_{595}}]_{\mathbf{Ab1+Ab2}} - [\mathbf{OD_{450}/OD_{595}}]_{\mathbf{Control\ Ab2}}}{[\mathbf{OD_{450}/OD_{595}}]_{\mathbf{Control\ Ab2}}} \times \mathbf{100}$

4.6. References

1. Hollingsworth, M.A. and B.J. Swanson, *Mucins in cancer: protection and control of the cell surface.* Nature Reviews Cancer, 2004. **4**(1): p. 45-60.
2. van de Wiel-van Kemenade, E., et al., *Episialin (MUC1) inhibits cytotoxic lymphocyte-target cell interaction.* The Journal of Immunology, 1993. **151**(2): p. 767-776.
3. Taylor-Papadimitriou, J., et al., *MUC1 and cancer.* Biochimica et Biophysica Acta (BBA)-Molecular Basis of Disease, 1999. **1455**(2): p. 301-313.
4. Kufe, D.W., *MUC1-C oncoprotein as a target in breast cancer: activation of signaling pathways and therapeutic approaches.* Oncogene, 2012. **32**(9): p. 1073-1081.
5. Beatson, R.E., J. Taylor-Papadimitriou, and J.M. Burchell, *MUC1 immunotherapy.* Immunotherapy, 2010. **2**(3): p. 305-327.
6. Nath, S. and P. Mukherjee, *MUC1: a multifaceted oncoprotein with a key role in cancer progression.* Trends in molecular medicine, 2014.
7. Tan, L., et al., *PEGylated Anti-MUC1 Aptamer-Doxorubicin Complex for Targeted Drug Delivery to MCF7 Breast Cancer Cells.* Macromolecular bioscience, 2011. **11**(10): p. 1331-1335.
8. Falahat, R., et al., *Enhanced targeting delivery to tumor cells using mucoadhesive chitosan and chlorotoxin.* Cancer Research, 2014. **74**(19 Supplement): p. 5410-5410.
9. Ta, H.T., C.R. Dass, and D.E. Dunstan, *Injectable chitosan hydrogels for localised cancer therapy.* Journal of Controlled Release, 2008. **126**(3): p. 205-216.
10. Kurihara, T., et al., *Selectivity of a replication-competent adenovirus for human breast carcinoma cells expressing the MUC1 antigen.* Journal of Clinical Investigation, 2000. **106**(6): p. 763-771.
11. Wykes, M., et al., *MUC1 epithelial mucin (CD227) is expressed by activated dendritic cells.* Journal of leukocyte biology, 2002. **72**(4): p. 692-701.
12. Fattorossi, A., et al., *Constitutive and inducible expression of the epithelial antigen MUC1 (CD227) in human T cells.* Experimental cell research, 2002. **280**(1): p. 107-118.
13. Walker, K.W., et al., *A rapid and sensitive cellular enzyme-linked immunoabsorbent assay (CELISA) for the detection and quantitation of antibodies against cell surface determinants: I. A comparison of cell fixation and storage techniques.* Journal of immunological methods, 1992. **154**(1): p. 121-130.
14. Liu, Z., T. Gurlo, and H. von Grafenstein, *Cell-ELISA using β-galactosidase conjugated antibodies.* Journal of immunological methods, 2000. **234**(1): p. P153-P167.
15. Ogino, T., X. Wang, and S. Ferrone, *Modified flow cytometry and cell-ELISA methodology to detect HLA* class *I antigen processing machinery components in cytoplasm and endoplasmic reticulum.* Journal of immunological methods, 2003. **278**(1): p. 33-44.

16. Jeon, H., et al., *Quantification of complement system activation by measuring C5b-9 cell surface deposition using a cell-ELISA technique.* Journal of immunological methods, 2014. **415**: p. 57-62.

17. Smith, D.D., C.B. Cohick, and H.B. Lindsley, *Optimization of cellular ELISA for assay of surface antigens on human synoviocytes.* BioTechniques, 1997. **22**(5): p. 952-957.

18. Wiranowska, M., et al., *Evaluation of blood-brain barrier permeability and the effect of interferon in mouse glioma model.* Journal of neuro-oncology, 1992. **14**(3): p. 225-236.

19. Wiranowska, M. and A.K. Naidu, *Interferon effect on glycosaminoglycans in mouse gliomain vitro.* Journal of neuro-oncology, 1994. **18**(1): p. 9-17.

20. Lourenço, E.V. and M.-C. Roque-Barreira, *Immunoenzymatic quantitative analysis of antigens expressed on* the *cell surface (cell-ELISA)*, in *Immunocytochemical Methods and Protocols*. 2010, Springer. p. 301-309.

21. Feit, C., et al., *An enzyme-linked immunosorbert assay (ELISA) for the detection of monoclonal antibodies recognizing surface antigens expressed on viable cells.* Journal of immunological methods, 1983. **58**(3): p. 301-308.

22. Feng, H., et al., *Expression of MUC1 and MUC2 mucin gene products in human ovarian carcinomas.* Japanese journal of clinical oncology, 2002. **32**(12): p. 525-529.

23. Dong, Y., et al., *Expression of MUC1 and MUC2 mucins in epithelial ovarian tumours.* The Journal of pathology, 1997. **183**(3): p. 311-317.

24. Gendler, S., et al., *Molecular cloning and expression of human tumor-associated polymorphic epithelial mucin.* Journal of Biological Chemistry, 1990. **265**(25): p. 15286-15293.

25. Dahiya, R., et al., *Mucin synthesis and secretion in various human epithelial cancer cell lines that express the MUC-1 mucin gene.* Cancer research, 1993. **53**(6): p. 1437-1443.

26. Oosterkamp, H.M., et al., *Comparison of MUC-1 mucin expression in epithelial and non-epithelial cancer cell lines and demonstration of a new short variant form (MUC-1/Z).* International journal of cancer, 1997. **72**(1): p. 87-94.

27. Treon, S.P., et al., *Muc-1 core protein is expressed on multiple myeloma cells and is induced by dexamethasone.* Blood, 1999. **93**(4): p. 1287-1298.

28. Ho, S.B., et al., *Heterogeneity of mucin gene expression in normal and neoplastic tissues.* Cancer research, 1993. **53**(3): p. 641-651.

29. Lu, K.H., et al., *Selection of potential markers for epithelial ovarian cancer with gene expression arrays and* recursive *descent partition analysis.* Clinical Cancer Research, 2004. **10**(10): p. 3291-3300.

30. Moore, A., et al., *In vivo targeting of underglycosylated MUC-1 tumor antigen using a multimodal imaging* probe. Cancer Research, 2004. **64**(5): p. 1821-1827.

31. Wei, N., et al., *A double-regulated oncolytic adenovirus with improved safety for adenocarcinoma therapy.* Biochemical and biophysical research communications, 2009. **388**(2): p. 234-239.

32. Galli, R., et al., *Isolation and characterization of tumorigenic, stem-like neural precursors from human* glioblastoma. Cancer research, 2004. **64**(19): p. 7011-7021.

33. Wiranowska, M., et al., *CD44 adhesion molecule and neuro-glial proteoglycan NG2 as invasive markers of glioma.* Brain cell biology, 2006. **35**(2-3): p. 159-172.

34. Levitin, F., et al., *The MUC1 SEA module is a self-cleaving domain.* Journal of Biological Chemistry, 2005. **280**(39): p. 33374-33386.

35. von Mensdorff-Pouilly, S., M. Moreno, and R.H. Verheijen, *Natural and induced humoral responses to MUC1*. Cancers, 2011. **3**(3): p. 3073-3103.

36. Brayman, M., A. Thathiah, and D.D. Carson, *MUC1: a multifunctional cell surface component of reproductive tissue epithelia.* Reproductive Biology and Endocrinology, 2004. **2**(1): p. 4.

37. He, P., S.S. Davis, and L. Illum, *In vitro evaluation of the mucoadhesive properties of chitosan microspheres.* International Journal of Pharmaceutics, 1998. **166**(1): p. 75-88.

38. Williams, E.C., R. Toomey, and N. Alcantar, *Controlled release niosome embedded chitosan system: Effect of crosslink mesh dimensions on drug release.* Journal of Biomedical Materials Research Part A, 2012. **100**(12): p. 3296-3303.

39. Falahat, R., et al., *Targeted delivery to tumor cells by using tunable nano-delivery system with chlorotoxin.* Cancer Research, 2013. **73**(8 Supplement): p. 4523-4523.

CHAPTER 5: ATR-FTIR ANALYSIS OF SPECTRAL AND BIOCHEMICAL CHANGES IN GLIOMA CELLS INDUCED BY CHLOROTOXIN

5.1. Abstract

Chlorotoxin (CTX) is a small peptide with unique targeting properties towards gliomas and other tumors of the neuroectodermal origin. Despite being investigated in many *in vivo* and *in vitro* targeted drug delivery and imaging studies, the mechanism of interaction between CTX and tumor cells has not been well understood. This study presents a new approach in monitoring the biochemical and biophysical changes in glioma cells after being exposed to CTX using Attenuated Total Reflection Fourier Transform Infra-Red (ATR-FTIR) spectroscopy. In the first part, we characterized the signature spectra of CTX and U87 cells. Next, we evaluated the differences in biochemical compositions of the spectra of the glioma cells treated with and without CTX over different incubation time periods. Our results indicated biochemical changes in U87 cells at different stages of incubation with CTX, with the most notable changes occurring after 30 min of incubation. Detailed comparisons of the spectra of the U87 cells treated with and without CTX for 30 min revealed distinct changes and shifts in the band frequencies associated with proteins and lipids. In particular, a downshift of the band assigned to CH_2 scissoring of lipid membranes from 1454 cm^{-1} to 1448 cm^{-1} followed by an appearance of a new shoulder at wavenumber of 1465 cm^{-1} revealed conformational changes in hydrocarbon chain packing in lipid bilayers of U87 cells due to CTX. Other frequency shifts indicated additional changes in conformation and orientation of lipids and proteins in U87 cells exposed to CTX.

5.2. Introduction

Chlorotoxin (CTX) is a 36-amino acid peptide derived from the venom of the scorpion *Leirius quinquestriatus* that preferentially binds to tumor cells of neuroectodermal origin, such as glioma, but not to normal non-transformed cells [1-3].

Several studies have demonstrated its use as an imaging and targeting agent for drug and radioisotope delivery [4-7]. However, the mechanism of interaction of CTX with cancer cells has not been well understood, and it needs to be further evaluated to optimize its use as a targeting compound for cancer cells.

Attenuated Total Reflection Fourier Transform Infra-Red (ATR-FTIR) spectroscopy is a well-established analytical method for the detection of molecular and structural changes in a wide range of chemical and biological samples [8]. As a label-free technique, it has been widely used for various exploratory and diagnostic investigations [9, 10]. A well-studied example is investigating the differences between the spectra of cancerous and non-cancerous cells and tissues [11-15].

In this study, we used ATR-FTIR spectroscopy to analyze the spectral and biochemical changes induced in U87, a glioma cell line, exposed to CTX at different incubation times. First, we characterized the signature spectra of CTX and U87 cells by assigning and evaluating the infrared absorption bands and their second derivatives.

Next, we analyzed the differences in biochemical compositions of the spectra of the glioma cells incubated with and without CTX by calculating the ratios of the areas of the bands corresponding to proteins, lipids, nucleic acids, and carbohydrates. Detailed comparisons of the spectral changes and band shifts also were performed, and possible mechanisms for the observed changes were further discussed.

5.3. Materials and Methods

5.3.1. Cell Line

U87, a human glioblastoma astrocytoma cell line (American Type Culture Collection) was used in this study. Cells were cultured in Minimum Essential Medium with Earle's Balanced Salts (MEM/EBSS; Hyclone, UT) supplemented with 10% Fetal Bovine Serum (FBS) and 2 mM L-glutamine, penicillin, and streptomycin. Cells were grown in 25 cm^2 culture flasks (Corning, NY) and incubated at 37ºC with 5% CO_2.

5.3.2. Cell Treatment with CTX

Cells were detached from adherent cultures using trypsinization (0.05% Trypsin/0.53mM EDTA; Corning, NY) and resuspended in the growth medium. After adjusting the cell density to 5×10^5 cells/ml, 250 µl of the cell suspension (1.25×10^5 cells) was placed in micro-centrifuge tubes. Cells received 25 µl of CTX (Iris Biotech, Germany) at a concentration of 10 µM (U87+CTX) or 25 µl of the culture medium (U87) and incubated for incremental time periods ranging from 15 min to 24 h at 37ºC in 5% CO_2. Following the incubation, cells were washed 3 times with 0.9% NaCl solution (Sigma-Aldrich, MO) and centrifuged at 400 g for 5 min to remove the culture medium and the unbound CTX. Cells were then resuspended in 0.9% NaCl solution and adjusted to a density of 5×10^5 cells/ml.

5.3.3. ATR-FTIR Spectroscopy

The ATR-FTIR spectra were obtained using a Nicolet 6700 spectrometer (Thermo Scientific, WI). A total of 100 µl of the prepared cell suspensions was introduced onto a 45º ZnSe flat crystal (Thermo Scientific, WI) and allowed to air dry for 1 hr. To remove any excess water, the formed films were exposed to an ultrapure nitrogen flux before collecting the spectra. The spectra in the 4000-400 cm^{-1} region were collected using 300 scans at a spectral resolution of

4 cm^{-1}. It should be noted that both U87+CTX and U87 cells were washed after incubation and before taking the spectra; therefore, the interference of unbound CTX was eliminated from the spectra.

5.3.4. Data Analysis

The data analysis was performed using OMNIC software (Thermo Scientific, WI). To ensure appropriate comparison between different samples, all the spectra were baseline corrected and normalized to amide I band at 1655 cm^{-1}. The complexity of the cell structure due to the presence of proteins, lipids, carbohydrates, and nucleic acids results in broad and superimposed bands in several spectral regions. As a resolution enhancement technique, the second derivative of each processed spectrum was calculated using Savitsky–Golay derivative function to resolve broad and overlapping bands into individual bands and eliminate possible artifacts. The areas under specific peaks in the absorbance spectrum were measured using OMNIC software. The subregion for each peak was selected based on the range of the peak resolved using the secondary derivative spectrum. This analysis was performed in triplicate. Statistical analysis was carried out using the Microsoft Excel Analysis Tool Pack. The data presented as descriptive statistical parameters (mean and SD). The Student's t-test was used to assess the statistical significance of the differences between U87 cells incubated in the absence and presence of chlorotoxin. $^{**}p < 0.01$ and $^{*}p < 0.05$ were considered to be statistically significant.

5.4. Results and Discussion

5.4.1. Vibrational Assignments

5.4.1.1. Chlorotoxin (CTX)

The absorption and the second derivative spectra of CTX are shown in Figure 5.1a, b. The characteristic frequency values and detailed assignments of the major bands are listed in

Table 5.1. The most prominent bands were observed at 1645 cm^{-1} and 1545 cm^{-1} assigned to amide I and amide II α-helical structures, respectively. The band at 1516 cm^{-1} was associated with ν(C-C) and δ(C-H) of Tyrosine ring. Similarly, the 1446 cm^{-1} peak was assigned to $\delta(CH_2)$ of Tyrosine and Phenylalanine amino acid side chains present in CTX. The peaks at 1408 cm^{-1} and 1388 cm^{-1} were assigned to ν(C-N) of Glutamine and Methionine and $\delta_w(CH_2)$ of Tyrosine, respectively. The strong amide I and amide II bands observed in the spectrum of CTX were both associated with the α-helical structure. This was in accordance with the Nuclear Magnetic Resonance (NMR) studies where the solution structure of CTX has been shown to be mainly an α-helix packed against a small β-sheet and cross-linked by three disulfide bonds [16].

5.4.1.2. U87 Cells

The absorption and the second derivative spectrum of U87 cells are shown in Figure 5.2a–d. The 3000–2820 cm^{-1} spectral region (Figure 5.2a, c) includes the bands that are associated with symmetric and antisymmetric stretching vibrations of CH_3 and CH_2 groups, mainly from lipids. Whereas the strong amide I band at 1655 cm^{-1} (Figure 5.2b, d) represents α-helical structure of proteins, the band at 1635 cm^{-1} is associated with β-sheet secondary structure of proteins in U87 cells. The shoulder at 1684 cm^{-1} also corresponds to antiparallel β-sheet structure of proteins [17]. The band at 1543 cm^{-1} was assigned to amide II. The band at 1739 cm^{-1} is primarily associated with stretching vibrations of lipid ester carbonyls [18, 19]. A list of detailed characteristics of all the major bands in the spectra of U87 cells is given in Table 5.2.

5.4.2. Analysis of the Integrated Area Ratios

Calculating the ratios of the areas of the bands corresponding to proteins, lipids, nucleic acids, and carbohydrates is one of the Feature Extraction (FE) techniques that has been used for the analysis of the spectra of the biological materials [20]. To monitor the biochemical changes

in U87 cells induced by CTX at different incubation time points, the ratios of the integrated areas of the bands at 1740 cm^{-1}, amide II (1543 cm^{-1}), 1080 cm^{-1}, and 1050 cm^{-1} corresponding to lipids, proteins, nucleic acids, and carbohydrates were calculated and compared to those of U87 cells without CTX treatment.

Figure 5.3 shows the ratio of the areas under amide II and 1742 cm^{-1} bands corresponding to protein and lipid, respectively [21]. The most significant change occurred for U87 cells after 30 min of incubation with CTX, where the protein-to-lipid ratio had a 65% increase ($^{**}p < 0.01$) compared to U87 cells without CTX treatment. Similarly, 21% and 33% increases in protein-to-lipid ratio ($^{**}p < 0.01$) were found for U87 cells incubated with CTX (U87+CTX) for 15 min and 1 h compared to U87 cells. This increase implies the cellular uptake of CTX in U87 cells incubated with CTX. Whereas 2 h of incubation resulted in an 18% increase in the ratio ($^{*}p < 0.05$) for U87+CTX cells compared to U87, no significant difference of this ratio was found between U87 and U87+CTX after 3 h and 24 h of incubation.

The changes in amide II: 1080 cm^{-1} area ratio (representing protein-to-nucleic acid ratio) in U87 and U87+CTX cells at different incubation times are shown in Figure 5.4. A 33% increase ($^{*}p < 0.05$) for this ratio occurred for U87 cells incubated with CTX for 30 min compared to U87 cells. No significant difference of this ratio was found between U87 and U87+CTX for other incubation time points.

The ratios of the areas under amide II and 1050 cm^{-1} bands corresponding to protein and carbohydrate, respectively, are shown in Figure 5.5. A 70% and 41% increase ($^{**}p < 0.01$) for this ratio occurred for U87 cells incubated with CTX for 1 h and 30 min compared to U87 cells. Similarly, 22% and 27% increase in protein-to-carbohydrate ratio ($^{*}p < 0.05$) were found for U87

cells incubated with CTX (U87+CTX) for 2 h and 24 h compared to U87 cells. No significant difference of this ratio was found between U87 and U87+CTX for 3 h.

As can be seen in Figures. 5.3, 5.4, and 5.5, significant differences between U87+CTX and U87 cells were found for all the measured ratios after 30 min of incubation. Therefore, the spectra of this time point were selected for detailed evaluation of the spectral changes in the following section.

5.4.3. Spectral Changes for U87 Cells after 30 min Treatment with CTX

Detailed comparisons between the spectra of U87 and U87+CTX cells were performed in the following three spectral regions.

5.4.3.1. 1760–1480 cm^{-1}

Figure 5.6 shows the absorption and second derivative spectra of U87 cells incubated with and without CTX for 30 min in the frequency region of 1760–1480 cm^{-1}. Several spectral shifts occurred for U87+CTX peaks compared to those of U87 cells in this region, which can be easily traced in the second derivative spectra shown in Figure 5.6. It can be seen that the peak at 1739 cm^{-1} associated with ν(C=O) of ester groups, primarily from lipids and fatty acids in U87 cells, shifted to 1744 cm^{-1} for U87+CTX. Also, the shoulder at 1718 cm^{-1} diminished and almost disappeared for U87+CTX cells.

The bands around 1740 and 1730 cm^{-1} have been reported to reflect the stretching vibrations of non-hydrogen bonded and hydrogen bonded lipid ester carbonyls, respectively [17, 18]. They have been used to probe the changes in physical packing of lipid bilayers where tightly packed lipids show a lower portion of hydrogen-bonded carbonyls due to the lower water penetration into the interfacial region of the bilayer. Therefore, the observed upshift of the band at 1739 to 1744 cm^{-1} is indicative of an increase in the amount of non-hydrogen bonded lipid

ester carbonyls in the membrane bilayers of U87+CTX cells compared to U87 cells, suggesting that CTX induces changes in physical packing of U87 cell membranes. This is in agreement with previous studies in which the incorporation of a protein into lipid bilayer membranes resulted in an increase in the percentage of non-hydrogen bonded lipid ester carbonyls [18, 22].

Along with these changes, other shifts in this region were observed for amide I peaks, including upshifts of the bands at 1684 cm^{-1} and 1653 cm^{-1} for U87 cells to 1688 cm^{-1} and 1656 cm^{-1} for U87+CTX cells, respectively. These upshifts are indicative of conformational changes [18, 22]. Also, the shoulder at 1635 cm^{-1} assigned to amide I, β-sheet secondary structure diminished and almost disappeared for U87+CTX cells. This further confirms that secondary structure of proteins was affected by CTX. As can be seen in Figure 5.6, the amide II band had a 6 cm^{-1} upshift in the spectra of U87+CTX cells compared to U87 cells. As shown in several studies, the frequency changes in amide bands correlate with the strength alterations of the hydrogen bonds [22-24]. While an upshift represents weakening of hydrogen bonds in stretching vibrations, it indicates stronger hydrogen bonds for bending vibrations [23]. It has been shown that the shifts of amide II band induced by hydrogen bonding derive predominantly from N-H bending [25]. Therefore, the observed upshift of amide II band in the spectra of U87+CTX compared to U87 cells indicates an increase in N-H hydrogen bonding within transmembrane proteins. Other changes included two shifts of the peaks at frequencies of 1513 cm^{-1} and 1492 cm^{-1} for U87 cells to 1516 cm^{-1} and 1496 cm^{-1} for U87+CTX cells, respectively. All the changes are summarized in Table 5.3.

5.4.3.2. 1480–1280 cm^{-1}

Comparative representations of the absorption and second derivative spectra of U87 cells incubated with and without CTX for 30 min in the frequency region of 1480–1280 cm^{-1} are

shown in Figure 5.7. A new shoulder appeared at 1465 cm^{-1} for U87+CTX cells, which was assigned to CH_2 scissoring of lipids.

The peak at 1454 cm^{-1} assigned to asymmetric CH_2 and CH_3 in plane bending vibrations in lipids for U87 cells downshifted to 1448 cm^{-1} for U87+CTX cells. The shifts in CH_2 scissoring bands have been reported to associate with the changes in conformational orders and chain packing of lipid molecules [22, 26]. In particular, a downshift of the CH_2 scissoring bands has been associated with transitions from typical highly-ordered orthorhombic phases to a metastable hexagonal phase [22, 26]. Therefore, the observed downshift along with the appearance of the shoulder at 1465 cm^{-1} indicates the changes in the conformational ordering and lateral packing of the hydrocarbon chains of the lipid molecules in U87 cell membranes induced by CTX. Similar changes also were observed for U87+CTX cells after 15 min and 1 h of incubation (data not shown).

A large upshift of 9 cm^{-1} was observed for the 1341 cm^{-1} peak of U87 cells assigned to CH_2 wagging of phospholipid, fatty acid, triglyceride, and amino acid side chains, where it shifted to 1350 cm^{-1} for U87+CTX cells. The CH_2 wagging modes have been used to monitor the conformational sequences and *trans-gauche* isomerization of acyl chain in lipid bilayers [26, 27]. While the wagging mode at 1341 cm^{-1} reflects an end-*gauche* conformation, the band at 1354 cm^{-1} corresponds to double-*gauche* conformations [26]. Thus, the observed upshift of CH_2 wagging band from 1341 to 1350 cm^{-1} clearly indicates a change in the conformational orders of acyl chains in lipid bilayers.

In addition, an increase in the number of *gauche* conformers has been associated with an increase in disordering of the lipid bilayers [26, 28], suggesting that the upshift of CH_2 wagging

band is indicative of an increase in conformational disorders of acyl chains in lipid bilayers of U87 cells due to CTX.

5.4.3.3. 1280–880 cm^{-1}

The absorption and second derivative spectra of U87 cells incubated with and without CTX for 30 min in the frequency region of 1280–880 cm^{-1} are shown in Figure 5.8. This region includes the absorbance of infrared mainly due to the presence of phosphates, carbohydrates, and nucleic acids. Two major shifts were observed for U87+CTX cells compared to U87 cells after 30 min of incubation in this region. The 1051 cm^{-1} peak for U87 cells assigned to stretching vibrations of COH group in carbohydrates (polysaccharides or glycogen) had a 4 cm^{-1} downshift to 1047 cm^{-1} for U87+CTX cells. Also, the 916 cm^{-1} peak assigned to ribose ring vibration of RNA for U87 cells upshifted to 922 cm^{-1} for U87+CTX cells. All the spectral changes for U87 cells after 30 min of treatment with CTX are summarized in Table 5.3.

5.5. Conclusions

We used ATR-FTIR spectroscopy to evaluate the biochemical changes in U87 glioma cells in response to incubation with CTX at different time intervals. The analysis of the integrated area ratios of the bands corresponding to major biochemical components (protein-to-lipid, protein-to-carbohydrate and protein-to-nucleic acid) indicated that the most significant changes between U87 and U87+CTX cells occurred at the incubation period of 30 min.

Comparisons of the different regions of the spectra for U87 and U87+CTX cells incubated for 30 min revealed distinct changes and shifts in the band frequencies. The band at 1739 cm^{-1} associated with ν(C=O) of lipids shifted to 1744 cm^{-1}, indicating an increase in the percentage of non-hydrogen bonded lipid ester carbonyls in U87+CTX cells compared to U87 cells. The shifts of the amide I bands associated with the conformational changes in

transmembrane proteins of U87+CTX cells compared to U87 cells. The upshift of the amide II band further confirmed the conformational changes and indicated an increase in N-H hydrogen bonding within transmembrane proteins.

The most significant changes occurred for the bands associated with CH_2 deformations, indicating lipid fatty acyl chain disorders. First, the 6 cm^{-1} downshift of the CH_2 scissoring band at 1454 cm^{-1} along with the appearance of the shoulder at 1465 cm^{-1} indicated conformational alteration in ordering and lateral packing of the hydrocarbon chains of the lipid molecules, suggesting transitions of the lipid chains from highly-ordered orthorhombic phases to a metastable hexagonal phase. This was further supported by 9 cm^{-1} upshift of the band at 1341 cm^{-1} associated with CH_2 wagging, which indicated an increase in the number of *gauche* conformers, implying an increase in conformational disorders of acyl chains in lipid bilayers of U87+CTX cells compared to U87 cells due to CTX. These findings are particularly interesting, as they suggest CTX introduces disorders in lipid acyl chains of the lipids in U87+CTX cell membranes.

Our results indicate that ATR-FTIR can be used to monitor the biochemical changes induced in glioma cells by CTX. Also, we were able to detect important conformational and structural changes in glioma cells due to CTX.

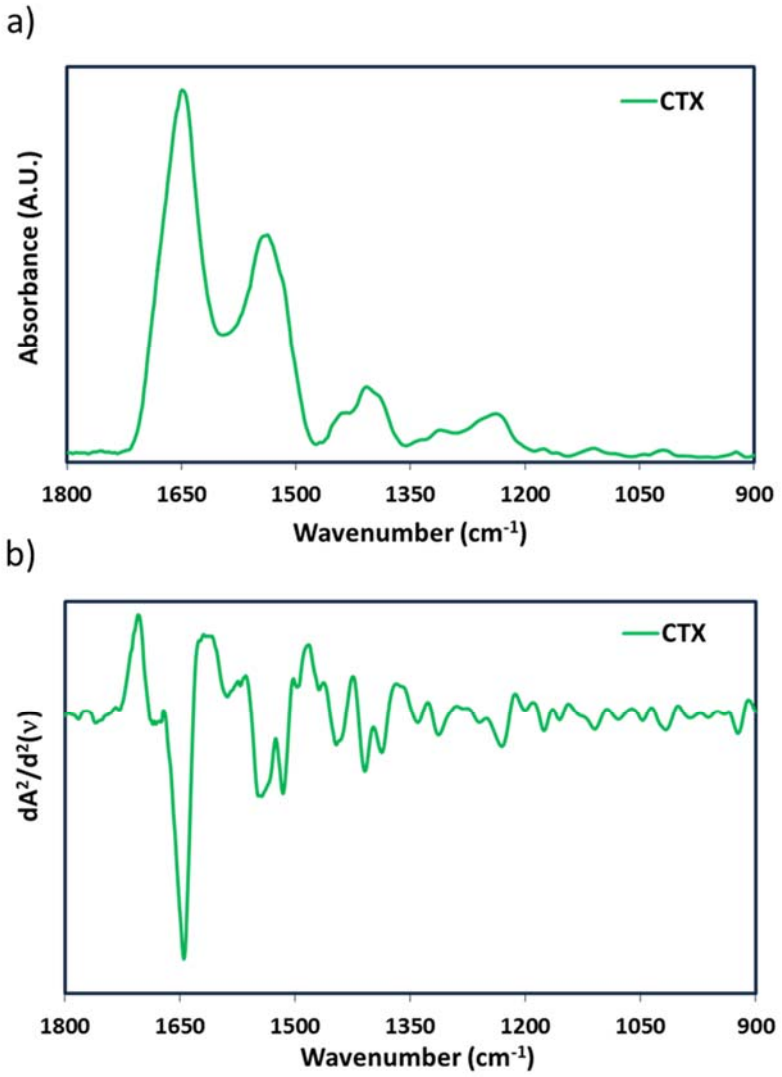

Figure 5.1 Absorption (a) and corresponding second derivative (b) spectra of CTX in frequency region of 1800–900 cm^{-1}

Table 5.1 Frequencies and assignments of major absorption peaks in ATR-FTIR spectra of CTX

Wavenumber (cm^{-1})	Assignment	Major Contribution
1760	ν(C=O)	Aspartic acid [29]
1680	ν(C=O)	Glutamine [29]
1645	ν(C=O)	Amide I, α-helix [30, 31]
1589	$\delta(NH_2)$	Glutamine [29]
	ν(C-C) ring	Phenylalanine, Tyrosine
1545	δ(N-H) + ν(C-N)	Amide II
1516	ν(C-C) ring + δ(C-H)	Tyrosine [17, 29]
1446	$\delta(CH_2)$	Phenylalanine, Tyrosine [29, 31, 32] Glutamine Proline
1409	ν(C-N)	Glutamine [17, 29, 32] Methionine
1387	$\delta_w(CH_2)$	Tyrosine [29]
1340	δ(CH)	Cysteine [29, 32]
	$\delta_t(CH_2)$	Proline
1313	$\delta(CH_2)$	Glutamine [29, 32]
1231	ν(CO)	Tyrosine [29, 33]
1175	$\delta(CH_2)$ + δ(COH)	Tyrosine [29, 32]
1155	ν(C-O)	Threonine [29]
1109	$\gamma(CH_2)$	Histidine [29]
1017	ν(C=C) ring	Histidine [29]
923	γ ring ν(C-C)	Histidine [29]

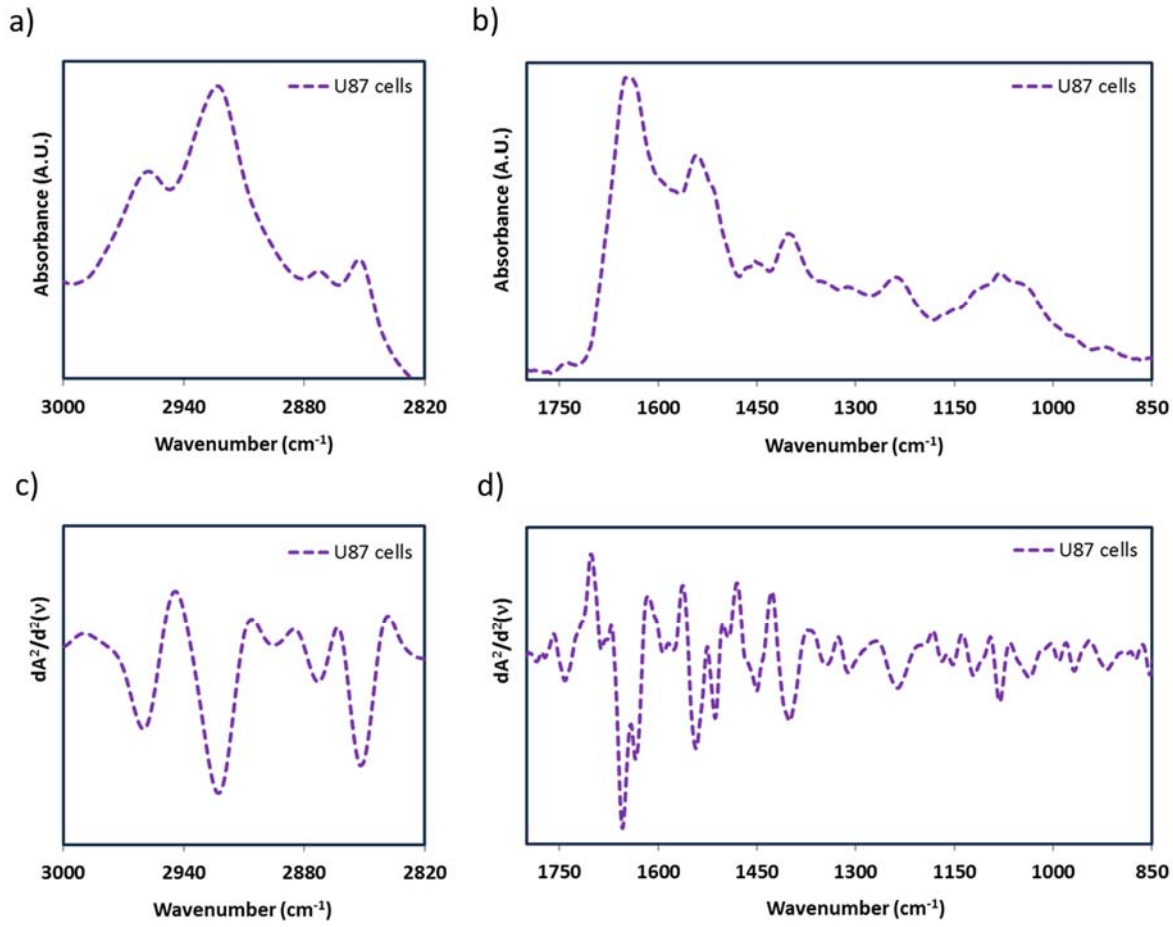

Figure 5.2 Absorption and second derivative spectra of U87 cells in frequency region of 3000–2820 cm^{-1} (a, c) and 1800–850 cm^{-1} (b, d)

Table 5.2 Band assignments of major peaks in IR spectra of U87 cells in 2980–900 cm^{-1} region

Wavenumber (cm^{-1})	Assignment	Major Contribution
2960	$\nu_{as}(CH_3)$	Saturated fatty acids
2922	$\nu_{as}(CH_2)$	Saturated fatty acids
2873	$\nu_s(CH_3)$	Saturated fatty acids
2851	$\nu_s(CH_2)$	Saturated fatty acids
1739	ν(C=O)	Phospholipids – cholesterol ester
1684	Amide I, antiparallel β-sheet	Protein
1655	Amide I, α-helix	Protein
1635	Amide I, β-sheet	Protein
1584	$\nu_{as}(COO^-)$ ν(C-C) tyrosine	Protein [29, 33]
1543	Amide II	Protein
1455	$\delta_{as}(CH_2)$, $\delta_{as}(CH_3)$	Mainly lipids, with small contribution from proteins [11, 12, 19, 34, 35]
1400	ν_s(C=O) of COO^- $\delta_s(CH_2)$, $\delta_s(CH_3)$	Lipids and proteins [11, 35]
1342	CH_2 wagging	Phospholipid, fatty acid, amino acid side chains [13, 19]
1312	ν(C-N)	Proteins [36]
1237	$\nu_{as}(PO_2^-)$	Mainly nucleic acids, with small contribution from phospholipids
1170	ν_{as}(C-O) CO-O-C ester bonds	Phospholipids – cholesterol ester
1150	ν(C-O), γ(COH)	Carbohydrates
1120	ν(C-O)	Ribose ring – RNA [19, 37]
1083	$\nu_s(PO_2^-)$	Nucleic acids, weak glycogen
1041	ν(COH)	Polysaccharides, glycogen [11, 19]
992	ν(C-O), ν(C-C) $\nu_s(PO_4^{=})$	Ribose – RNA [38] RNA [11]
966	ν (C-O), ν(C-C) $\nu_s(PO_4^{=})$	Deoxyribose – DNA [38] Phosphorylated proteins and nucleic acids [11]
917	ν(COP)	Phosphorylated protein [39] Ribose ring: RNA [19, 40]

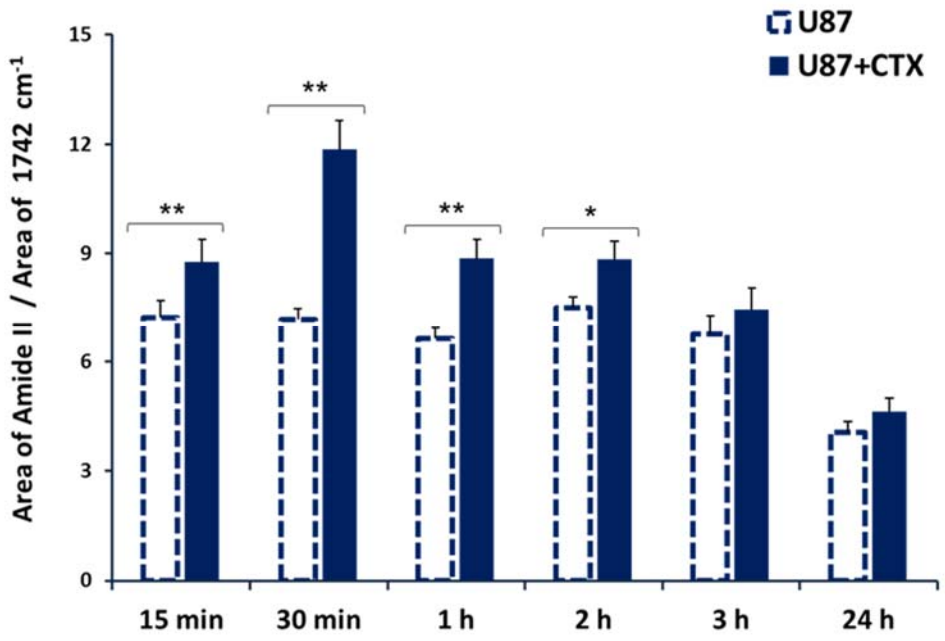

Figure 5.3 Comparisons of amide II/ 1742 cm^{-1} area ratios for U87 cells with and without CTX treatment at different incubation time points. Data represent mean ± SD for n=3 measurements. Statistical significance between U87 and U87+CTX analyzed using Student's t-test: **$p<0.01$ and *$p<0.05$

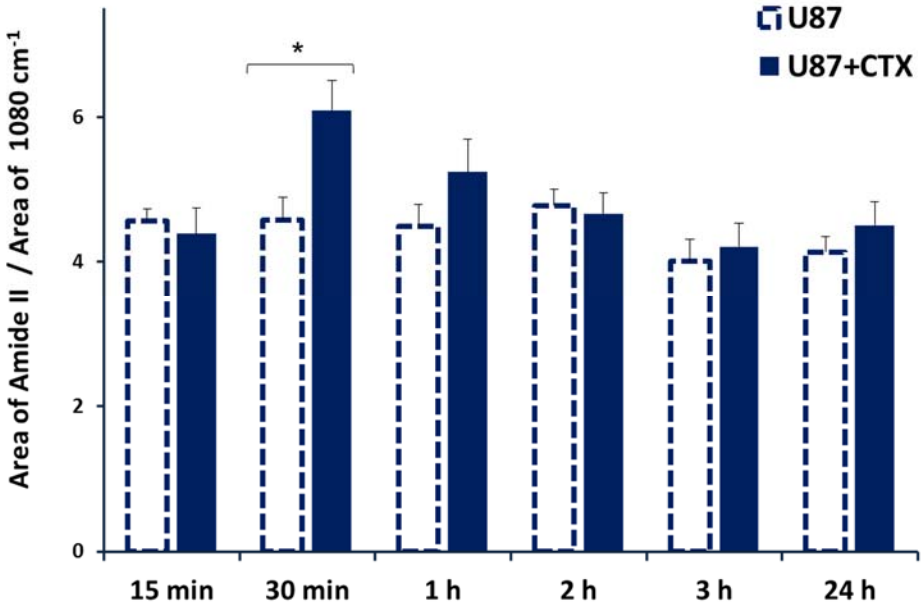

Figure 5.4 Comparisons of amide II/ 1080 cm^{-1} area ratios for U87 cells with and without CTX treatment at different incubation time points. Data represent mean ± SD for n=3 measurements. Statistical significance between U87 and U87+CTX analyzed using Student's t-test: *$p<0.05$

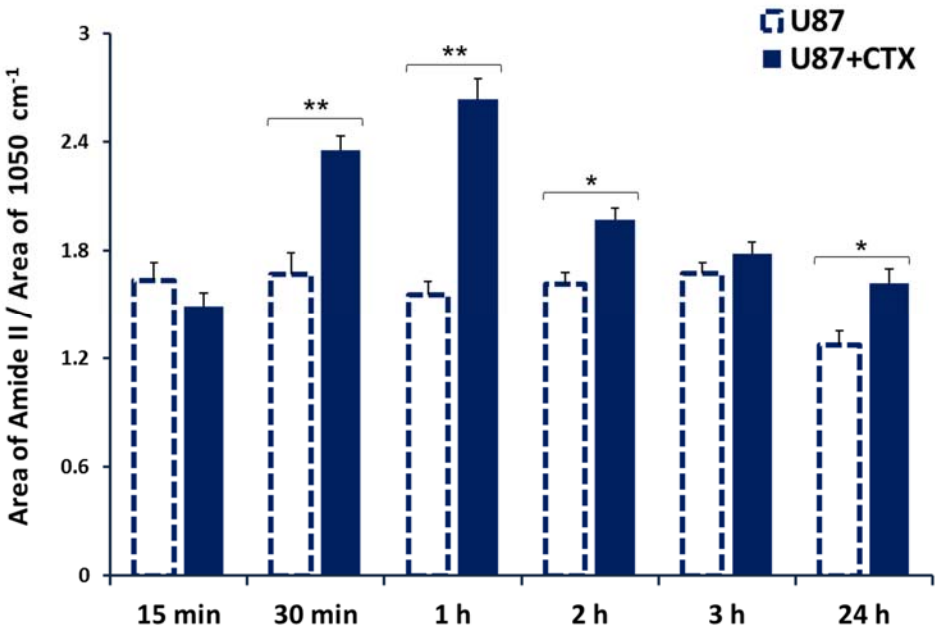

Figure 5.5 Comparisons of amide II/ 1050 cm^{-1} area ratios for U87 cells with and without CTX treatment at different incubation time points. Data represent mean ± SD for n=3 measurements. Statistical significance between U87 and U87+CTX analyzed using Student's t-test: **$p<0.01$ and *$p<0.05$

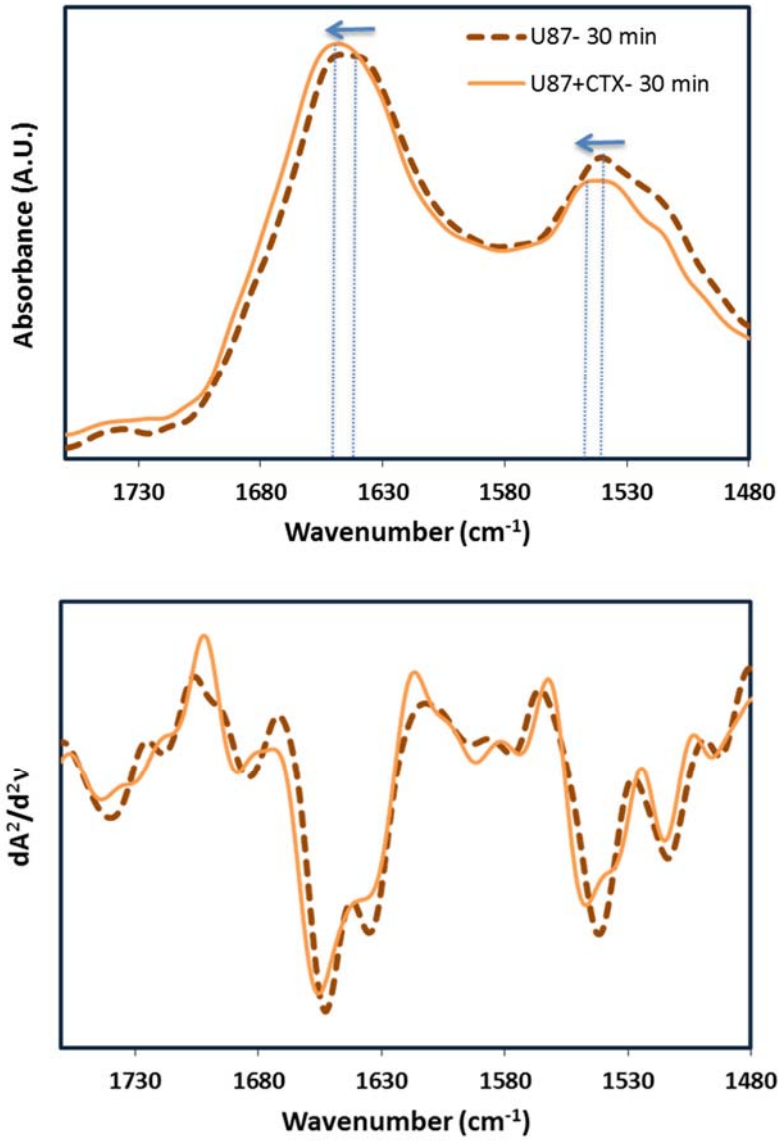

Figure 5.6 Absorption and second derivative spectra of U87 cells incubated with and without CTX for 30 min in frequency region of 1760–1480 cm^{-1}

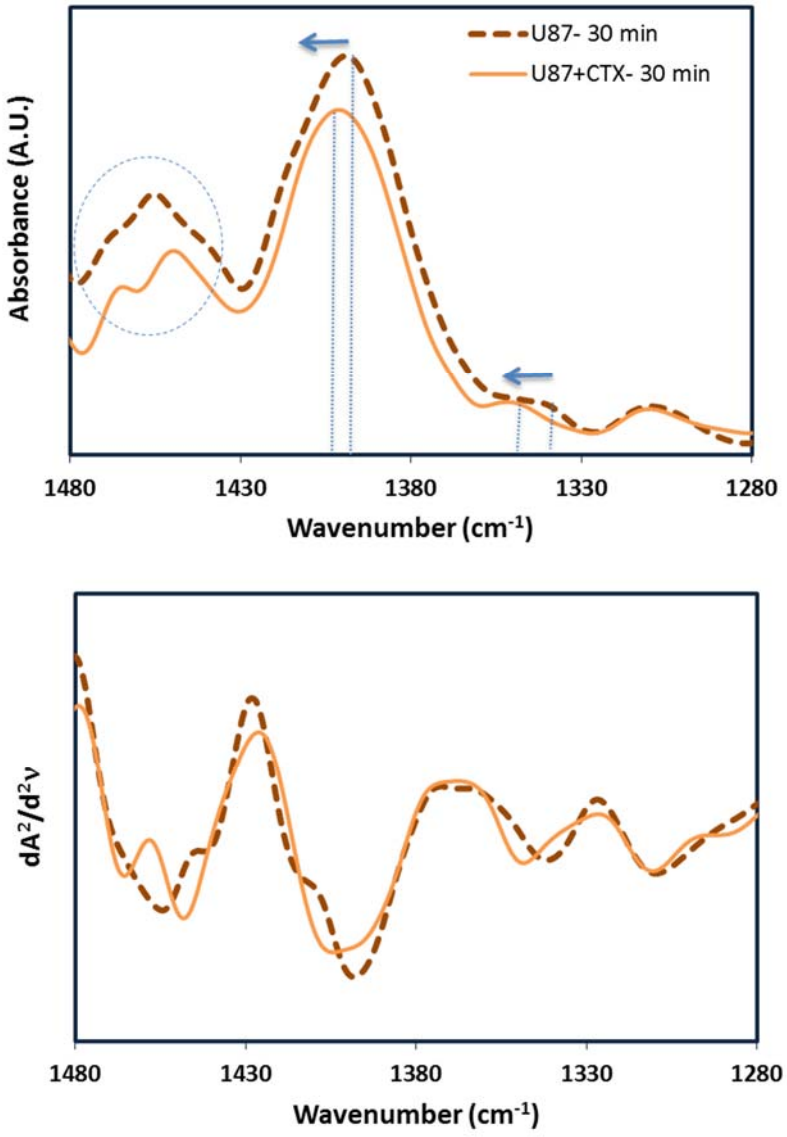

Figure 5.7 Absorption and second derivative spectra of U87 cells incubated with and without CTX for 30 min in frequency region of 1480–1280 cm^{-1}. The spectral differences between U87 and U87+CTX were found mainly for the bands associated with CH_2 deformations indicating lipid fatty acyl chain disorders

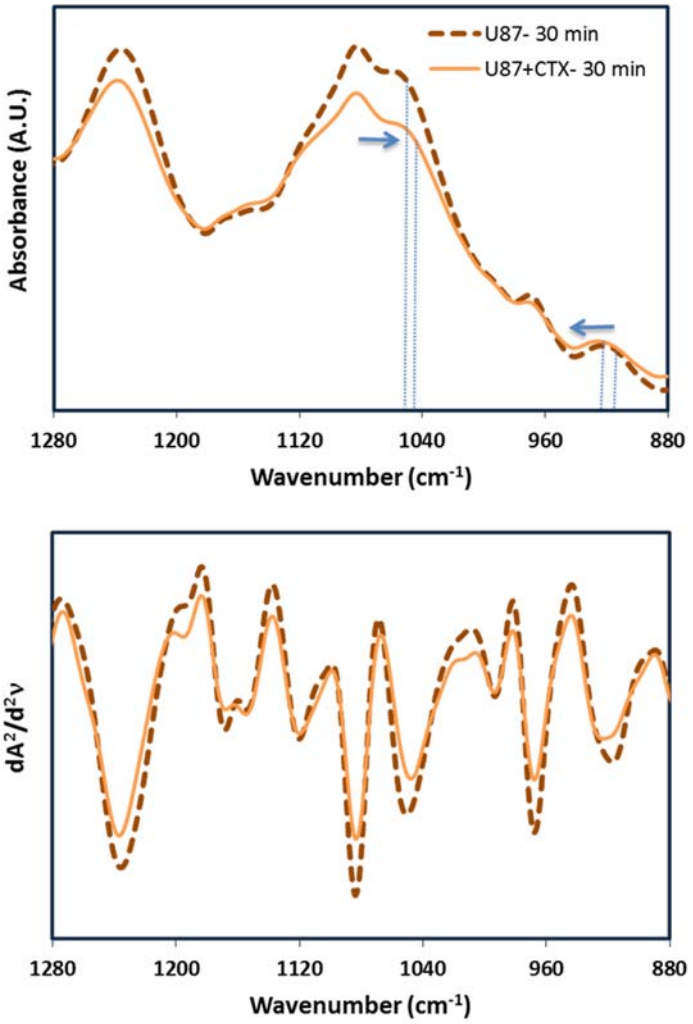

Figure 5.8 Absorption and second derivative spectra of U87 cells incubated with and without CTX for 30 min in frequency region of 1280–880 cm^{-1}

Table 5.3 Summary of changes observed in ATR-FTIR spectra of U87 cells incubated with and without CTX for 30 min

Wavenumber (cm^{-1})		Change	Assignment	Major Contribution
U87	U87+CTX			
1739	1744	+5 shift	ν(C=O)	Phospholipids – cholesterol ester
1684	1688	+4 shift		
1653	1656	+3 shift	Amide I, α-helix	Protein
1635		disappeared	Amide I, β-sheet	Protein
1542	1548	+6 shift	Amide II, α-helix	Protein
1513	1516	+3 shift		
1492	1496	+4 shift		
	1465	appeared		
1454	1448	-6 shift	$\delta_{as}(CH_2)$, $\delta_{as}(CH_3)$	Mainly lipids, with small contribution from proteins [11, 12, 19, 34, 35]
1440		disappeared		
1398	1404	+6 shift	ν_s(C=O) of COO^- $\delta_s(CH_2)$, $\delta_s(CH_3)$	Lipids
1341	1350	+9 shift	CH_2 wagging	Phospholipid, fatty acid, triglyceride, amino acid side chains [19]
1191	1195	+4 shift		
1051	1047	-4 shift	ν(C-O), δ(C-O)	Polysaccharides , glycogen
916	922	+6 shift	ν(COP)	Phosphorylated protein [39] Ribose ring – RNA [19, 40]

5.6. References

1. Debin, J.A., J.E. Maggio, and G.R. Strichartz, *Purification and characterization of chlorotoxin, a chloride channel ligand from the venom of the scorpion.* American Journal of Physiology-Cell Physiology, 1993. **264**(2): p. C361-C369.
2. Lyons, S.A., J. O'Neal, and H. Sontheimer, *Chlorotoxin, a scorpion-derived peptide, specifically binds to gliomas and tumors of neuroectodermal origin.* Glia, 2002. **39**(2): p. 162-173.
3. Wiranowska, M., L.O. Colina, and J.O. Johnson, *Clathrin-mediated entry and cellular localization of* chlorotoxin *in human glioma.* Cancer Cell Int, 2011. **11**: p. 27.
4. Veiseh, M., et al., *Tumor paint: a chlorotoxin: Cy5. 5 bioconjugate for intraoperative visualization of cancer foci.* Cancer research, 2007. **67**(14): p. 6882-6888.
5. Akcan, M., et al., *Chemical re-engineering of chlorotoxin improves bioconjugation properties for tumor imaging and targeted therapy.* Journal of medicinal chemistry, 2011. **54**(3): p. 782-787.
6. Falahat, R., et al., *Enhanced targeted delivery of paclitaxel to tumor cells of epithelial and neuroectodermal origin using chlorotoxin-chitosan nanodelivery system.* Cancer Research, 2015. **75**(15 Supplement): p. 3677-3677.
7. Dardevet, L., et al., *Chlorotoxin: A Helpful Natural Scorpion Peptide to Diagnose Glioma and Fight Tumor Invasion. Toxins*, 2015. **7**(4): p. 1079-1101.
8. Goormaghtigh, E., V. Raussens, and J.-M. Ruysschaert, *Attenuated total reflection infrared spectroscopy of proteins and lipids in biological membranes.* Biochimica et Biophysica Acta (BBA)-Reviews on Biomembranes, 1999. **1422**(2): p. 105-185.
9. Mourant, J., et al., *FTIR spectroscopy demonstrates biochemical differences in mammalian cell cultures at different growth stages.* Biophysical journal, 2003. **85**(3): p. 1938-1947.
10. Mordechai, S., et al., *Possible common biomarkers from FTIR microspectroscopy of cervical cancer and melanoma.* Journal of microscopy, 2004. **215**(1): p. 86-91.
11. Maziak, D.E., et al., *Fourier-transform infrared spectroscopic study of characteristic molecular structure in cancer cells of esophagus: an exploratory study.* Cancer detection and prevention, 2007. **31**(3): p. 244-253.
12. Yano, K., et al., *Direct measurement of human lung cancerous and noncancerous tissues by Fourier transform infrared microscopy: can an infrared microscope be used as a clinical tool?* Analytical Biochemistry, 2000. **287**(2): p. 218-225.
13. Fujioka, N., et al., *Discrimination between normal and malignant human gastric tissues by Fourier transform infrared spectroscopy.* Cancer Detection and Prevention, 2004. **28**(1): p. 32-36.
14. Gazi, E., et al., *A correlation of FTIR spectra derived from prostate cancer biopsies with Gleason grade and tumour stage.* European urology, 2006. **50**(4): p. 750-761.

15. Krafft, C., et al., *Analysis of human brain tissue, brain tumors and tumor cells by infrared spectroscopic mapping.* Analyst, 2004. **129**(10): p. 921-925.

16. Lippens, G., et al., *NMR sequential assignments and solution structure of chlorotoxin, a small scorpion toxin that blocks chloride channels.* Biochemistry, 1995. **34**(1): p. 13-21.

17. Baenziger, J.E. and C.J. daCosta, *Membrane protein structure and conformational change probed using Fourier transform infrared spectroscopy.* Biophysical Analysis of Membrane Proteins: Investigating Structure and Function, 2008: p. 259-288.

18. Corrie, J., et al., *Lipid-protein interactions at the nicotinic acetylcholine receptor A functional coupling between nicotinic receptors and phosphatidic acid-containing lipid bilayers.* Journal of Biological Chemistry, 2002. **277**(1): p. 201-208.

19. Ozek, N.S., et al., *Characterization of microRNA-125b expression in MCF7 breast cancer cells by ATR-FTIR spectroscopy. Analyst*, 2010. **135**(12): p. 3094-3102.

20. Baker, M.J., et al., *Using Fourier transform IR spectroscopy to analyze biological materials.* Nature protocols, 2014. **9**(8): p. 1771-1791.

21. *Szalontai*, B., et al., *Membrane dynamics as seen by Fourier transform infrared spectroscopy in a cyanobacterium, Synechocystis PCC 6803: the effects of lipid unsaturation and the protein-to-lipid ratio.* Biochimica et Biophysica Acta (BBA)-Biomembranes, 2000. **1509**(1): p. 409-419.

22. Tamm, L.K. and S.A. Tatulian, *Infrared spectroscopy of proteins and peptides in lipid bilayers.* Quarterly reviews of biophysics, 1997. **30**(04): p. 365-429.

23. Barth, A., *Infrared spectroscopy of proteins.* Biochimica et Biophysica Acta (BBA)-Bioenergetics, 2007. **1767**(9): p. 1073-1101.

24. Takekiyo, T., et al., *Pressure stability of the α-helix structure in a de novo designed protein (α-l-α) 2 studied by FTIR spectroscopy.* Biopolymers, 2007. **85**(2): p. 185-188.

25. Myshakina, N.S., Z. Ahmed, and S.A. Asher, *Dependence of amide vibrations on hydrogen bonding.* The Journal of Physical *Chemistry* B, 2008. **112**(38): p. 11873-11877.

26. Moore, D.J., M.E. Rerek, and R. Mendelsohn, *FTIR spectroscopy studies of the conformational order and phase behavior of ceramides.* The Journal of Physical Chemistry B, 1997. **101**(44): p. 8933-8940.

27. Chia, N.-C. and R. Mendelsohn, Conformational *disorder in unsaturated phospholipids by FTIR spectroscopy.* Biochimica et Biophysica Acta (BBA)-Biomembranes, 1996. **1283**(2): p. 141-150.

28. *Venkataraman*, N. and S. Vasudevan, *Conformation of methylene chains in an intercalated surfactant bilayer.* The Journal of Physical Chemistry B, 2001. **105**(9): p. 1805-1812.

29. Barth, A., *The infrared absorption of amino acid side chains.* Progress in biophysics and molecular *biology*, 2000. **74**(3): p. 141-173.

30. Barry, B., H. Edwards, and A. Williams, *Fourier transform Raman and infrared vibrational study of human skin: assignment of spectral bands.* Journal of Raman Spectroscopy, 1992. **23**(11): p. 641-645.

31. Venyaminov, S.Y. and N. Kalnin, *Quantitative IR spectrophotometry of peptide compounds in water (H2O) solutions. I. Spectral parameters of amino acid residue absorption bands.* Biopolymers, 1990. **30**(13-14): p. 1243-1257.

32. Stewart, S. and P. Fredericks, *Surface-enhanced Raman spectroscopy of amino acids adsorbed on an electrochemically prepared silver surface.* Spectrochimica Acta Part A: Molecular and Biomolecular Spectroscopy, *1999*. **55**(7): p. 1641-1660.

33. Mudunkotuwa, I.A., A. Al Minshid, and V.H. Grassian, *ATR-FTIR spectroscopy as a tool to probe surface adsorption on nanoparticles at the liquid–solid interface in environmentally and biologically relevant media.* Analyst, 2014. **139**(5): p. 870-881.

34. Dreissig, I., et al., *Quantification of brain lipids by FTIR spectroscopy and partial least squares regression.* Spectrochimica Acta Part A: Molecular and Biomolecular Spectroscopy, 2009. **71**(5): p. 2069-2075.

35. Wong, P., et al., *Infrared spectroscopy of exfoliated human cervical cells: evidence of extensive structural changes during carcinogenesis.* Proceedings of the National Academy of Sciences, 1991. **88**(24): p. 10988-10992.

36. Sajan, D., et al., *NIR-FT Raman, FT-IR and surface-enhanced Raman scattering spectra, with theoretical* simulations *on chloramphenicol.* Journal of Raman Spectroscopy, 2008. **39**(12): p. 1772-1783.

37. Meade, A.D., et al., *Growth substrate induced functional changes elucidated by FTIR and Raman* spectroscopy *in in–vitro cultured human keratinocytes.* Analytical and bioanalytical chemistry, 2007. **387**(5): p. 1717-1728.

38. Dovbeshko, G.I., et al., *FTIR spectroscopy studies of nucleic acid damage.* Talanta, 2000. **53**(1): p. 233-246.

39. Bellisola, G. and C. Sorio, *Infrared spectroscopy and microscopy in cancer research and diagnosis.* American journal of cancer research, 2012. **2**(1): p. 1.

40. Banyay, M., M. Sarkar, and A. Gräslund, *A library of IR bands of nucleic acids in solution.* Biophysical chemistry, 2003. **104**(2): p. 477-488.

CHAPTER 6: SUMMARY

This study reports a development of a localized and targeted drug delivery system using chlorotoxin (CTX) assisted thermosensitive niosome-chitosan hydrogel complexes for cancer treatment. With the controlled, sustained and targeted delivery features, this system represents a novel approach in cancer therapy.

Release rate studies indicated that embedding niosomes in chitosan hydrogel significantly extends the release rates. Embedding CTX along with niosomes in chitosan hydrogel resulted in slightly more extended release rates as compared to the release rates from niosomes alone in chitosan hydrogel. Attachment of CTX to the surface of niosomes shown by TEM imaging improved the stability of niosomes resulting in extended release rates. ATR-FTIR studies also confirmed the interaction of CTX with niosomes.

Thermosensitive chitosan hydrogels containing Paclitaxel (PTX)-loaded niosomes with various amount of crosslinker in their formulations (L-Ch, M-Ch and H-Ch) were also prepared. The incorporation of PTX-niosomes in chitosan hydrogels resulted in prolonged release profiles which lasted for more than 40 days in a pH-dependent manner. While L-Ch and M-Ch hydrogels indicated similar PTX release profiles, relatively slower release rates (around 10%) were found for H-Ch hydrogels. The release mechanism was identified as anomalous transport (a combination of diffusion-controlled and swelling-controlled release) for L-Ch hydrogels when incubated in PBS with pH 6.3. Major changes in swelling behavior were observed for L-Ch and M-Ch chitosan hydrogels with small physiologically relevant pH changes.

Having a sensitive and reproducible assay to detect the expression of MUC1 in various cancer cells is essential for further development of the drug delivery systems using chitosan hydrogel which have been shown to have a strong mucoadhesive property. Therefore, two variants of Cell ELISA assays using live and fixed cells were developed in this study. It was found that the Cell ELISA in live cells was not sensitive enough to detect a difference in MUC1 levels between the normal cells and tumor cells. However, we found that Cell ELISA in fixed cells followed by whole cell staining was a dependable method of MUC1 level detection in the normal and tumor cells showing significantly higher levels of MUC1 receptor in the tumor cells when compared to the normal controls. Both flow cytometry and Western blotting analyses correlated well with the Cell ELISA data and provided validation of the results.

ATR-FTIR spectroscopy was used to evaluate the biochemical changes in U87 glioma cells in response to incubation with CTX at different time intervals. The analysis of the integrated area ratios of the bands corresponding to major biochemical components indicated that the most significant changes between U87 and U87+CTX cells occurred at the incubation period of 30 min. Comparisons of the different regions of the spectra for U87 and U87+CTX cells incubated for 30 min revealed distinct changes and shifts in the band frequencies. The most significant changes occurred for the bands associated with CH_2 deformations, indicating lipid fatty acyl chain disorders. First, the 6 cm^{-1} downshift of the CH_2 scissoring band at 1454 cm^{-1} indicated conformational alteration in ordering and lateral packing of the hydrocarbon chains of the lipid molecules, suggesting transitions of the lipid chains from highly-ordered orthorhombic phases to a metastable hexagonal phase. This was further supported by 9 cm^{-1} upshift of the band at 1341 cm^{-1} associated with CH_2 wagging, which indicated an increase in the number of gauche conformers, implying an increase in conformational disorders of acyl chains in lipid bilayers of

U87+CTX cells compared to U87 cells due to CTX. These findings are particularly interesting, as they suggest CTX introduces disorders in lipid acyl chains of the lipids in U87+CTX cell membranes. They also indicate that by understanding the interactions between CTX and glioma cells, we can achieve the optimized design of CTX assisted drug delivery systems for targeting gliomas.

Together these findings are encouraging as they indicate the developed drug delivery system in this study with the distinct tumor targeting features and extended release profiles would improve the specific and efficient delivery of anticancer drugs to tumor cells without affecting normal cells.

APPENDIX A COPYRIGHT PERMISSIONS

Below is permission for the use of materials in Chapter 4.

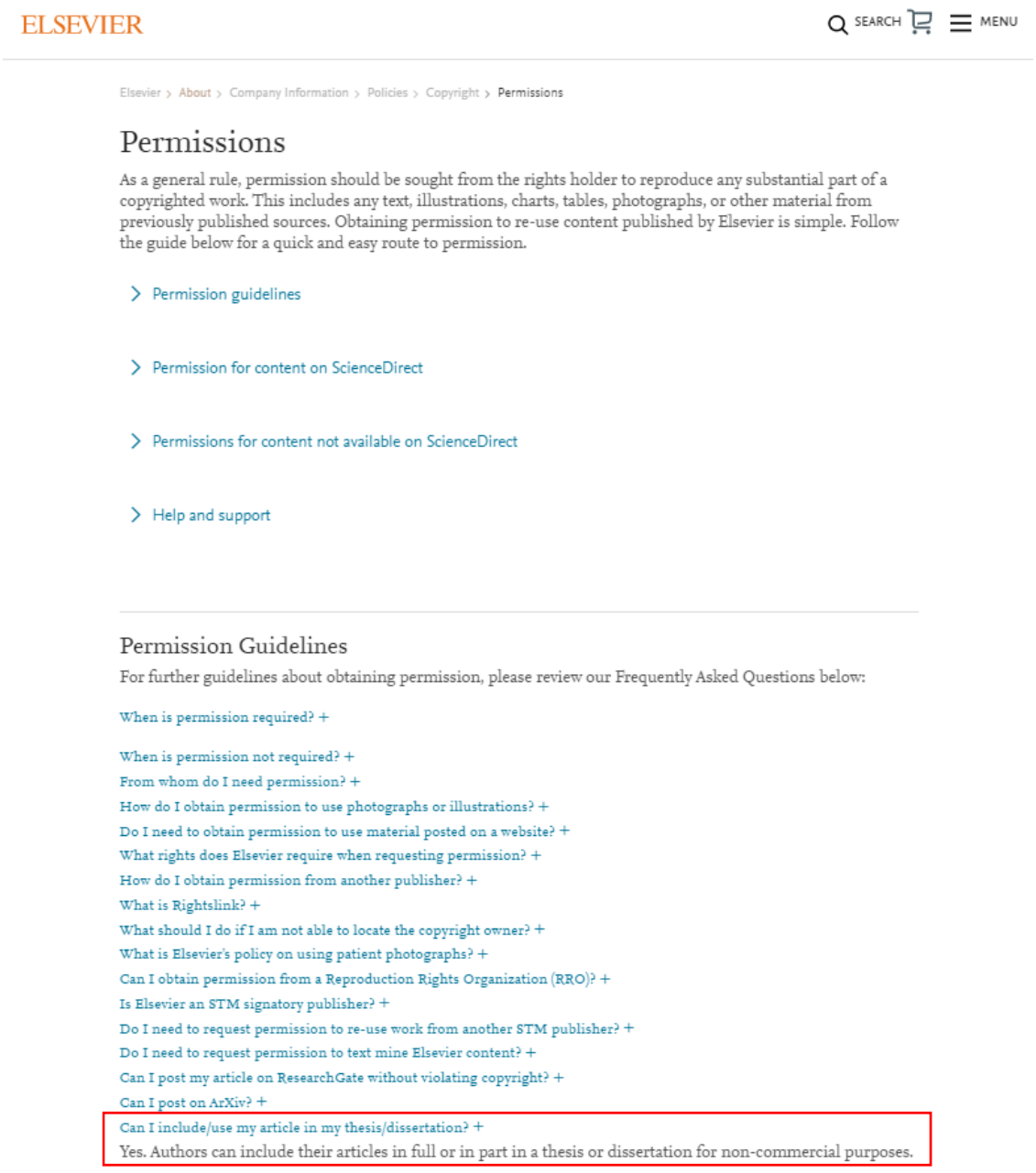

ELSEVIER

SEARCH MENU

Elsevier > About > Company Information > Policies > Copyright > Permissions

Permissions

As a general rule, permission should be sought from the rights holder to reproduce any substantial part of a copyrighted work. This includes any text, illustrations, charts, tables, photographs, or other material from previously published sources. Obtaining permission to re-use content published by Elsevier is simple. Follow the guide below for a quick and easy route to permission.

> Permission guidelines

> Permission for content on ScienceDirect

> Permissions for content not available on ScienceDirect

> Help and support

Permission Guidelines

For further guidelines about obtaining permission, please review our Frequently Asked Questions below:

When is permission required? +

When is permission not required? +
From whom do I need permission? +
How do I obtain permission to use photographs or illustrations? +
Do I need to obtain permission to use material posted on a website? +
What rights does Elsevier require when requesting permission? +
How do I obtain permission from another publisher? +
What is Rightslink? +
What should I do if I am not able to locate the copyright owner? +
What is Elsevier's policy on using patient photographs? +
Can I obtain permission from a Reproduction Rights Organization (RRO)? +
Is Elsevier an STM signatory publisher? +
Do I need to request permission to re-use work from another STM publisher? +
Do I need to request permission to text mine Elsevier content? +
Can I post my article on ResearchGate without violating copyright? +
Can I post on ArXiv? +
Can I include/use my article in my thesis/dissertation? +

Yes. Authors can include their articles in full or in part in a thesis or dissertation for non-commercial purposes.